Università degli Studi di Palermo

AREA QUALITÀ, PROGRAMMAZIONE
E SUPPORTO STRATEGICO
SETTORE STRATEGIA PER LA RICERCA
U. O. DOTTORATI

Doctoral Course in Civil, Environmental and Materials Engineering
Department of Engineering
ICAR/07

CHARACTERIZATION OF THE 3D PRINTING PROCESS FOR FINE-GRAINED SOILS

PhD Candidate
Silvia La Rosa

Coordinator
Prof. Antonina Pirrotta

Supervisor
Prof. Alessio Ferrari

CICLO XXXIV
A.A. 2021/2022

To Martina,
always missed but always present.

ACKNOWLEDGEMENTS

The research work discussed in this thesis would have never been possible without the inestimable support given to me by some fundamental people who surrounded me during the PhD study duration.

First and foremost, my extreme gratitude goes to my supervisor Prof. Alessio Ferrari, whose presence and guidance never lacked during these years of research. Without his patience and motivation it wouldn't be possible to complete my studies. His immense knowledge and passion are of great inspiration for me and I'm lucky to have had the opportunity to work with him.

I'm also thankful to the research group of the Geotechnical Laboratory of the Engineering Department of the University of Palermo: Dr. Marco Rosone for his contribution for my research work; Dr. Vincenzo Butticé, not only for advice and encouragement always offered to me as a colleague, but also for their friendship and support throughout the journey of completing my PhD; Mr. Giovanni Sapienza for all the testing laboratory knowledge shared with me, and for all the time spent helping me with the execution of the tests. My deepest thanks go to Prof. Calogero Valore and Prof. Maurizio Ziccarelli for their valuable guidance throughout my bachelor and master studies: thanks to their teaching abilities I couldn't help falling in love with Geomechanics. Additionally, I'd like to acknowledge Mr. Marco Starvaggi for his contribution on the development of the double porosity model within his Master thesis and my former Master colleague and true friend Mr. Alessio Vaccaro for its help in the development of the Python script.

I want to express my sincere gratefulness to Prof. Bernardo Caicedo Hormaza for hosting me at the University of Los Andes and guiding me during this amazing experience abroad. It was an extraordinary cooperation and an unrepeatable occasion to meet new motivating people. Amongst them, I want to acknowledge Dr. Julieth Monrroy for the inestimable help, and Mr. Camilo Jose Sanchez Avellaneda, with whom I collaborated during laboratory activities.

The cooperation with the industrial partners gave me the opportunity to face with an extremely interesting world populated by inspired people. My sincere gratitude goes to Dr. Francesco Belvisi and to Mr. Filippo Paredes, who supervised my first steps with 3D printing at OCORE s.r.l. and to Mr. Rosario Amato Sottosanti, who welcomed me at Terrecotte del Sole s.r.l. and helped me during my time with them.

Thanks to the technical staff of the Engineering Department of the University of Palermo, the Doctoral School Board and in particular the coordinator Prof. Antonina Pirrotta, for always being supporting and understanding during the PhD years.

I would like to express my heartfelt gratitude to my colleagues who have also become dear friends during my time working on my PhD. Chiara, Chiara and Santo, have been invaluable sources of support, encouragement, and camaraderie throughout this journey. Not only have they offered valuable insights and feedback on my work, but they have also been there for me as friends, offering a listening ear and a shoulder to lean on when things got tough. I am very lucky to have shared my path with you.

I am deeply grateful to the friends who have always been there for me. Martina D. and Stefano with their presence in my everyday life, but also Chiara D., Martina A., Gioia, Alessia, Marco, Giulia, Laura, Vanessa and Agnese. Whether through a listening ear, a word of encouragement, or a much-needed distraction, each and every one of you has played a crucial role

in these years. I am truly blessed to have each and every one of you as my friend and I am grateful to have such a strong and loving support system.

Lastly, I want to express my deepest gratitude to my family: to my mother Giusi and my father Vincenzo for their unwavering belief in my abilities even when I didn't believe in myself, and for always encouraging me to pursue my dreams; to my brother Carlo for his unfailing presence in my life – he sees me, he knows me, he understands me and he loves me no matter what.

ABSTRACT

The purpose of this study was to explore the 3D printing process of fine-grained soils with a geomechanichal approach. In particular, identifying the factors (including geomechanical characteristics of the soil, geometry of the problem, and 3D printer settings) that influence the behavior of 3D printed samples. To answer this question, three groups of materials differing in mineralogy, consistency limits and consistency, and three types of equipment have been used – an extruder and two 3D printers – to widely investigate the behaviour of the fine-grained soils when subjected to the process. First, the extrusion process has been studied finding that the parameter to take into account to predict the outcome are: the coefficient of consolidation of the soil, the extrusion length and the time of extrusion. Then, a double-porosity model was developed to predict the index properties of 3D printed specimens based on the geotechnical characteristics of the fine-grained soil and the specimens' geometry. This model was validated through its application to specimens with different values of the adimensional spacing between parallel filaments. The research then focuses on the structure of 3D printed clayey soil, examining the relationship between particle arrangements, pore size, orientation, and shape, and the 3D printing process. An experimental campaign was conducted to investigate the evolution of soil tensile state before, during, and after the 3D printing process using oedometric tests. Finally, the experimental campaign, conducted at the Geotechnical Laboratory of the University of Los Andes, sought to accurately reproduce 3D models generated using random field theory using a custom multimaterial 3D printer, finding the relationship between printing velocity, extrusion velocity and area of the nozzle that would guarantee an optimum 3D printing.

TABLE OF CONTENTS

ACKNOWLEDGEMENTS I

ABSTRACT III

TABLE OF CONTENTS IV

INTRODUCTION 1

1. STATE OF THE ART 3

1.1 Additive Manufacturing Overview 3

1.2 Additive Manufacturing in Geomechanics 5

1.3 Additive Manufacturing Techniques in Ceramics 6

1.4 Fine-Grained Soils as Printing Material 7

Trial and error approach 7
Mechanical characterization of extruded clayey soil 12
Extrusion of clayey soil as a new experimental method 13

1.5 PhD Project Development 13

2. MATERIALS USED IN THE EXPERIMENTAL PROGRAM 16

2.1 CC – Commercial Clay 16

2.2 Group A – Unipa Custom Geomaterials 17

2.3 Group B – UniAndes Custom Geomaterials 19

3. EXTRUSION PROCESS OF FINE-GRAINED SOILS 22

3.1 Materials 22

3.2 Extrusion Tests 22

Testing set-up 22
Results and analysis 23

3.3 Oedometric Tests 29

Testing set-up 29
Data elaboration 30
Data analysis 31
Specimens preparation 31
Results and analysis 33

3.4 Summary 35

4. 3D PRINTING OF SOILS, HOW-TO 36

4.1 3D Printers For Soils 36

Delta WASP 2040 Clay and Delta WASP 4070 Clay 36
Delta WASP 2040 Clay operating instructions 38
UNIANDES custom multimaterial 3D printer 40

4.2 GCODE Programming Language 41

GCODE programming language elements 41

4.3 G-Code Generation 43

Point 44
Line 44
Square 45
Serpentine 46

4.4 G-Code Generation with Python 49

5. A DOUBLE-POROSITY MODEL FOR 3D PRINTED FINE-GRAINED SOILS 53

5.1 Double-Porosity Framework 53

Adjacent filaments 56
Distanced filaments 61

5.2 Index Properties Prediction 63

5.3 Validation Of The Model 64

Index properties of the specimens 66

5.4 Summary 69

6. MICROSTRUCTURAL CHARACTERIZATION OF A 3D PRINTED SOIL 70

6.1 Introduction 71

6.2 Material And Methods 71

6.3 Fabric of the Printed Samples 73

6.4 Conclusion 77

6.5 Additional Images and Data Analysis 78

7. CHANGE IN THE TENSIONAL STATE OF A FINE-GRAINED SOIL DURING 3D PRINTING PROCESS 81

7.1 Material and Methods 81

Tested material 81
Specimens preparation 81
Testing Set-Up 88

7.2 Results and Analysis 89

Data collection 89
Data elaboration 90
Data analysis 91

7.3 Summary 94

8. MULTIMATERIAL 3D PRINTING OF FINE-GRAINED SOILS 96

8.1 Materials and Methods 96

Tested materials 96
Testing Set-Up 97
G-Code generation 97

8.2 Characterization Of The Custom Multimaterial 3d Printer 98

Identification of the problem 98
Proposed method 99
Experimental results 99

8.3 Faithful Multimaterial 3D Printing 100

Experimental campaign 101

8.4 Summary and Future Developments 103

CONCLUSIONS 104

REFERENCES 106

ANNEXES 108

INTRODUCTION

Additive manufacturing (AM), or 3D printing, is nowadays driving the third Industrial Revolution, and the technique born for printing polymeric material expands its application over a wide range of fields and materials. Exploring the potential of 3D printing technology in the field of fine-grained soils would allow to develop new methods for fabricating clay structures, to investigate the properties and performance of 3D printed clay materials, or to find new applications for 3D printed clay in areas such as architecture, industrial design, or sculpture.

The PhD research project here exposed deals thus with the 3D printing of fine-grained soils, with the novelty of studying them as a printing material and considering the 3D printing process as a series of geomechanical process to which the geomaterials are subjected.

The research pursued the following main objectives:

- reading the process of 3D printing of fine-grained soils from a geomechanical point of view;
- determining which geomechanical characteristics of the soil, the geometry of the problem and which 3D printer settings influence the behaviour of the 3D printed samples.

The thesis is organized as follows:

- Chapter 1 offers an overview of the current knowledge about the 3D printing technologies with a focus on their applications in the geomechanical field;
- Chapter 2 describes the three groups of fine-grained soils adopted in the investigation;
- Chapter 3 presents the testing campaign carried out to investigate the extrusion process of fine-grained soils mixtures;
- Chapter 4 describes the innovative technology used during the PhD research project, in particular the 3D printers, the GCODE language and the ways in which the G-codes have been written;
- Chapter 5 proposes a model to describe the index properties of 3D printed soils and its validation;
- Chapter 6 describes the results of the microstructural characterization of a 3D printed soil – it has been chosen to present this Chapter in the same form in which it has been published by the journal *Soils and Rocks* after peer-review;
- Chapter 7 details the outcomes of the investigation about the change in the tensional state of 3D printed fine-grained soils before, during and after printing;
- Chapter 8 presents the experimental campaign about the characterization of a multimaterial 3D printer;
- Chapter 9 reports the main findings of this thesis and some recommendations for future researches.

The research project has been proposed by the University of Palermo and funded by the Italian Ministry of University and Research within the PON-RI 2014-2020, achieving maximum score in the evaluation.

Two industrial partners and a foreign University have been involved:

- “OCORE s.r.l”, an innovative company within the ARCA consortium located in Palermo, active in the 3D printing industry. It was winner of the National Award for Innovation in 2017, with a well-established know-how in the 3D printing techniques in general and specialized in glass/carbon fiber-reinforced polymers;
- “Terrecotte del Sole S.r.l”, a company active on the production and selling of Sicilian typical artistic ceramics. The innovative mindset of the owners led to the acquisition of a 3D printer for ceramics, in order to explore new ways of production;
- University of Los Andes (Bogotá, Colombia), in which the Geomaterial and Infrastructure System (GeoSI) Group, led by Professor Bernardo Caicedo Hormaza, has already realized a custom multimaterial 3D printer for fine-grained soils. The work carried out in collaboration with the University of Los Andes is presented in Chapter 8.

1. STATE OF THE ART

The aim of this Chapter is to give the reader an overview of the current State of the Art.

While the 3D printing is a technique currently commonly used, the innovation of this research lies on the study of soils as printing materials. The literature review here presented, therefore, comprehends a variety of fields,

In this Chapter, though, will be first given an overview of the Additive Manufacturing techniques – of whom 3D printing techniques are part. Then the focus will go on how the Additive Manufacturing techniques would have served geomechanical purposes, to end with examples of uses of ceramic materials as printing materials – even without geomechanical interest.

1.1 ADDITIVE MANUFACTURING OVERVIEW

History of Additive Manufacturing begins in 1951 with the patent of photo-glyph recording by Otto John Munz, in which an object would have been reproduced by exposing selectively layers of a photo emulsion during the scanning the object. In less than a century, additive manufacturing technique increased in attractiveness and diffusion thanks to the technological improvements of the past years followed by and following the interest of researcher in this field, exponentially increasing in the past decade (figure 1.1).

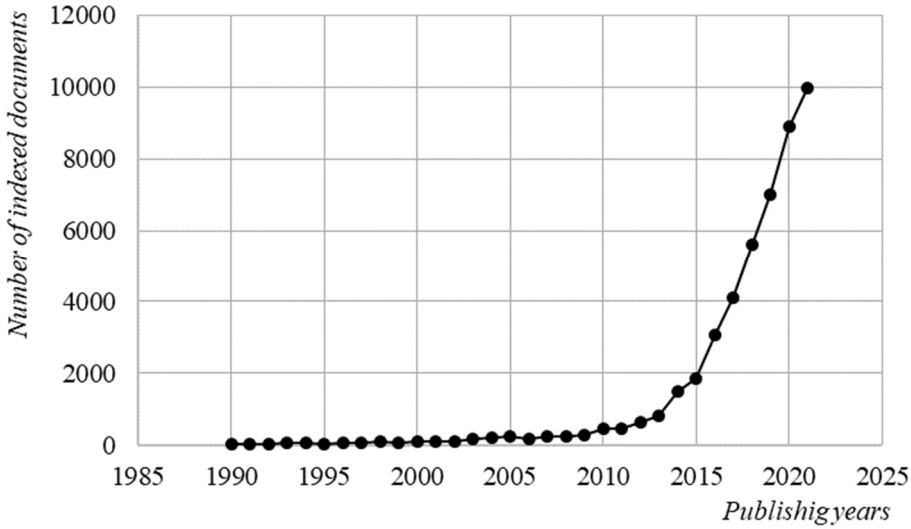

Figure 1.1 *- Number of indexed documents with keyword "additive manufacturing" from 1990 to 2021.*[1]

Additive Manufactory is defined by ASTM as "the process of joining material to make objects from 3D model data, usually layer upon layer, as opposed to subtractive methodologies"[2]. The 3D model of the object – usually created by computer-aided design (CAD) software or obtained by a scan of an existing one – is sliced in layers of same thickness by a slicing software that returns a file in which are written all of the instructions that the machine has to respect to

[1] *data collected from http://www.scopus.com*

[2] *Standard Terminology of Additive Manufacturing Technology, ASTM F2792-10, June 2010*

exactly reproduce the 3D model (e.g. initial position, path to be followed, speed of printing, temperature…).

Thanks to the fact that every object is produced adding the material layer by layer, Additive Manufacturing technologies enable to create complex geometric shapes impossible to create with subtractive technologies, and whenever it would have been possible to produce, the geometric complexity translated into additional costs, more time required or necessity of assemblage. The cost convenience of the industrial production with Additive Manufacturing technologies relies either in the possibility to manufacture on-demand – and so with no inventory needed –, and in the reduction of material waste during production. However, while for mass-production the start-up costs of subtractive manufacturing techniques can be absorbed within the high number of pieces created, additive manufacturing techniques become more convenient when a customized product is needed, as it happens for instance in automotive industry or in bio-medical applications.

The development of Additive Manufacturing perfectly fits into the digital revolution we're living in these years, adding to the democracy of information, the democracy of production. Even with the relevant concerns about copyright and public security, thanks to the low-cost of some of the Additive Manufacturing technologies available and of the printing material, everybody can create whatever he can draw. Hence, a virtuous cycle has been created, in which the improvement of Additive Manufacturing technologies inspires end-users and at the same time is enhanced by them.

Because of this fast diffusion, there are a lot of Additive Manufacturing techniques, differing from each other by the printing material and by the way in which layers are created, and because of it, many efforts have been made to classify in a comprehensive and clear way all of them. The ASTM International has classified AM technologies into seven categories: material extrusion, powder bed fusion, vat photopolymerization, material jetting, binder jetting, sheet lamination and directed energy deposition (table 1.1).

Table 1.1 *– ASTM International classification of AM technologies.*

	Technologies	Material	Power Source
Material extrusion	Fused Deposition Modelling (FDM) Contour Crafting	Thermoplastics, ceramic slurries, metal pastes	Thermal Energy
Powder Bed Fusion	Selective Laser Sintering (SLS) Direct Metal Laser Sintering (DMLS) Selective Laser Melting (SLM)	Atomized metal powder, ceramic powder	High-powered Laser Beam
	Electron Beam Melting (EBM)		Electron Beam
Vat Photopolymerization	Stereolithography (SLA)	Photopolymer, ceramics	Ultraviolet Laser
Material Jetting	Polyjet/Inkjet printing	Photopolymer, wax	Thermal Energy / Photocuring
Binder Jetting	Indirect Inkjet Printing	Polymer powder, Ceramic powder, metal powder	Thermal energy
Sheet Lamination	Laminated Object Manufacturing	Plastic film, metallic sheet, ceramic tape	Laser Beam
Directed Energy Deposition	Laser Engineered Net Shaping (LENS) Electronic Beam Welding (EBW)	Molten metal powder	Laser Beam

1.2 ADDITIVE MANUFACTURING IN GEOMECHANICS

In Geomechanics, use of Additive Manufacturing technologies is spreading in the past few years thanks to the possibility to easily reproduce the effective disposition of the geomaterial, substituting it with a polymer with adequate characteristics for the purpose.

The main possibility in research is to conduct multiple, and eventually destructive, tests on different near identical samples reproducing the prototype, changing boundary and/or loading conditions.

Research studies focalized into three main topics:

Study of behaviour of natural rocks. Natural rock samples are first scanned and digitalized, then the internal structure of the prototype is reproduced using materials with similar properties according to the purpose of the study (e.g. Ju et. al, 2014; Matsumura & Mizutani, 2015; Bourke, 2008). The main problem to be exceeded in this application field involves the resolution

of the rock images used as input, that directly affect the resolution of the printed samples, with the consequence of poorly represent fine-scale properties of the natural rock. On the other hand, an increase in the image resolution would add computational effort, not always allowed.

Fluid analysis in geotechnical systems. In these types of applications, real or artificial micro/macropore networks are reproduced in order to study the behaviour of the interstitial liquid i.e. varying pressure, temperature, chemical composition. The printing material in these experiences has been either only polymeric, and silica sand with a synthetic binder cured until complete polymerization (Dal Ferro & Morari, 2015; Gomez et al., 2019).

Grain morphology. Above this field of application, individual grains are first mathematically generated, and, after a CAD visualization, they are printed using a polymeric material. The pursued purpose is in this case to investigate the role of the grain morphology on the mechanical response of the geomaterial (Hanaor et al., 2016).

In all the cases reported, the accuracy of the printed specimens depends not only by the resolution of the model used as reference, but also by the printing method and by the printing material chosen for the study. In these cases, indeed, the material used to reproduce the geotechnical system is an artificial one (mostly polymeric or a natural one with polymeric binder), uncapable to replicate all the features at the same time.

1.3 ADDITIVE MANUFACTURING TECHNIQUES IN CERAMICS

For the purpose of this thesis, however, only the most relevant techniques involving the use of clay will be discussed, distinguishing the Additive Manufacturing techniques with respect to the form of the material before printing, as reported in the following table 1.2.

Table 1.2 *– Classification of ceramic-based AM technologies.*

	Technology	**Forming method**
Powder-based	Selective Laser Sintering (SLS)	Powder fusion
	Three-Dimensional Printing	Binder bonding
Slurry-based	Inkjet Printing	Binder bonding
	Direct Ink Writing	Extrusion

In the powder-based techniques clayey material is deposited in form of a powder on the substrate. In SLS technique the material is selectively irradiated with a high-power laser so that interparticle fusion occurs. In Three-Dimensional Printing technique a binder liquid material is sprayed between successive layers, the bonding of which occurs because of the solidification of the binder material.

In both cases a post-processing involving firing of the objects is planned.

Slurry-based techniques consider the clayey material dispersed in a liquid solvent. Thus, the material can be studied in a geotechnical way, considering the printing material as a granular biphasic medium.

In Inkjet Printing, the material consists in a dispersion of clay minerals within a liquid solvent with a liquid content ranging from 250% to 150%. The material is deposited through a printhead and after allowed to dry, it is sintered.

In Direct Ink Writing, or **Extrusion**, the material, in form of high viscous clayey paste, is extruded through a nozzle moving in the 3D space and deposited layer by layer. Due to the consistency of the printing material, the created object is self-standing and there's no need for support structure. In common applications, the manufactured object is then fired in a furnace.

Object of the research is the study of hydro-mechanical behaviour of 3D printed soils, hence only the last AM technique will be explored and discussed as reference of the successive study.

1.4 FINE-GRAINED SOILS AS PRINTING MATERIAL

When fine-grained soils have been used as printing material, the ways to find the adequate mix-design for the purposes involved different approaches. In this paragraph some interesting examples of that will be showed.

Trial and error approach

In September 2018, the Italian company CSP srl, within the WASP project, showed the first 3D-printed house, "Gaia" (figure 1.2). The 20 m^2 house has been printed using a big trellis-work 3D printer, called "Crane WASP" developed by them, using the soil available on site mixed with hydraulic lime, straw and rice hulls as printing material.

The modulus is conceived as an advanced eco-sustainable prototype in which structural and energetic design are integrated. The circular perimetrical wall is an alveolar structure in the cavities of which rice hulls are poured, taking advantage of their insulation properties (figure 1.3).

Figure 1.2 *– "Gaia", the house modulus printed by CSP[3].*

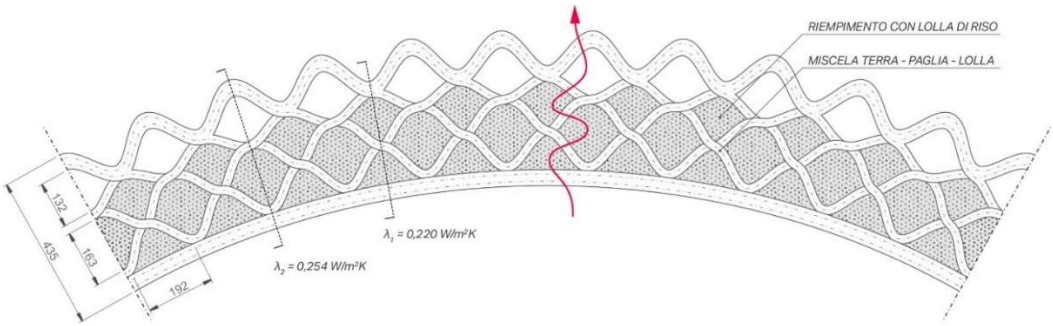

Fig. 1.3 *– Cross section of a sector of the 3D printed house "Gaia"[3].*

In the successive years, the research and development of the company continued, leading to the 3D printing of another type of house-moduli within the project Tecla (figure 1.4 and figure 1.5).

[3] *http://www.3d-wasp.com*

Figure 1.4 *– "Tecla", the house moduli printed by CSP[3].*

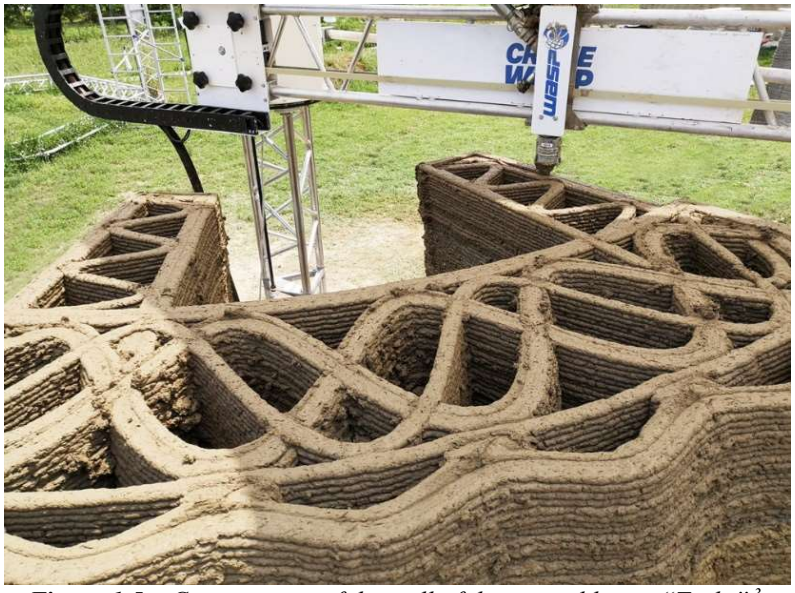

Figure 1.5 *– Cross section of the wall of the printed house "Tecla"[3].*

At the Institute of Advanced Architecture (IAAC, Barcelona) is active a Postgraduate Diploma in Open Thesis Fabrication (OTF) of 6-months duration ending with the realization of a

1:1 prototype. In the previous three years, 3D printing of buildings with unfired clay has been studied respectively with the projects “Terraperforma” (figure 1.6), “Digital Adobe” (figure 1.7) and “Building Architectural Continuity” (figure 1.8).

Figure 1.6 *– Terraperforma, IAAC*[4].

[4] *http://www.iaac.com*

Figure 1.7 *– Digital Adobe, IAAC [4].*

Figure 1.8 *– Building Architectural Continuity, IAAC [4].*

During the years of studies, conducted with a trial and error approach, clay has been mixed with additives to improve extrudability and strength, and to reduce shrinkage during drying (figure 1.9).
The material they proposed as printing material is a mixture of clay, brick dust and marble dust mixed with ash, wheat and hemp (respectively approximately 40%, 20%, 20% + 15%, 4.7%, <0.1%).

Figure 1.9 *– Sample printed by IAAC with the proposed mix design [4].*

Mechanical characterization of extruded clayey soil

In France, a study about the additive manufacturing of earth-based material at laboratory scale has been conducted (Perrot et al., 2018a). The material chosen for sperimentation was a fine-grained soil with characteristics showed in the following Table 1.3.

Table 1.3 *– Characteristics of the material used by Perrot et al, 2018a.*

d_{max} [mm]	d_{50} [μm]	P(10 μm) [%]	LL [-]	PL [-]	PI [-]	w [-]	τ_y [kPa]
1	8	>60	0.48	0.27	0.21	0.47	1.5

The printing phase was carried out with a flow rate of 2 cm/s with approximately 60 s of delay between successive layers, printing from two to four layers both using a circular nozzle and a rectangular nozzle.

Using alginate as additive to the soil, they evaluate the evolution of the yield stress and of the elastic modulus of the material, concluding that the additive only reduces the time required to the interstitial water to evaporate, thus increasing the suction and consequently the strength, but that the ultimate values don't change and that the samples printed with the rectangular nozzle exhibit compressive strength higher than that of the circular cross section samples.

Extrusion of clayey soil as a new experimental method

In all the previous cases, however, the raw earth used as printing material hasn't been studied from a geotechnical point of view, not considering how its multiphasic structure influences the behaviour.

It has been proved that, when reverse extrusion is performed, the water content of a fine-grained soil is linearly dependent from the logarithm of the extrusion pressure(Whyte, 1982; Kayabali & Tufenkci, 2010; Veràstegui-Flores & Di Emidio, 2014; Kayabali et al., 2015). The aim of their works was to propose and calibrate a new method for the determination of the consistency limits choosing the values of the liquid limit and of the plastic limit as those corresponding to certain values of extrusion pressure P_E (2300 kPa for the plastic limit and 15 kPa for the liquid limit), but their results can be read in an inverted manner.

Knowing the pressure range of the machine, the best mix design of the material would be that one that would guarantee a certain consistence in that range. After the determination of the consistency limits of the material, they would be plotted in a $\log P_E$-w graph associating to each of them the respective extrusion pressure; if the straight line passing through the two points overlaps the "optimum zone", the material is suitable for 3D printing.

1.5 PHD PROJECT DEVELOPMENT

In this Chapter has been discussed how 3D printing involving geotechnical field has only served as a tool to conduct geomechanical characterization, using non-geomaterials materials as printing materials to reproduce a real one, or how when geomaterials have been used, they would have been characterized following the classical mechanics, considering them as fluids or – in industrial and fine arts fields – finding the correct mix-design using a trial and error approach. In the next figure 1.10, a schematization of the current state of the art is presented.

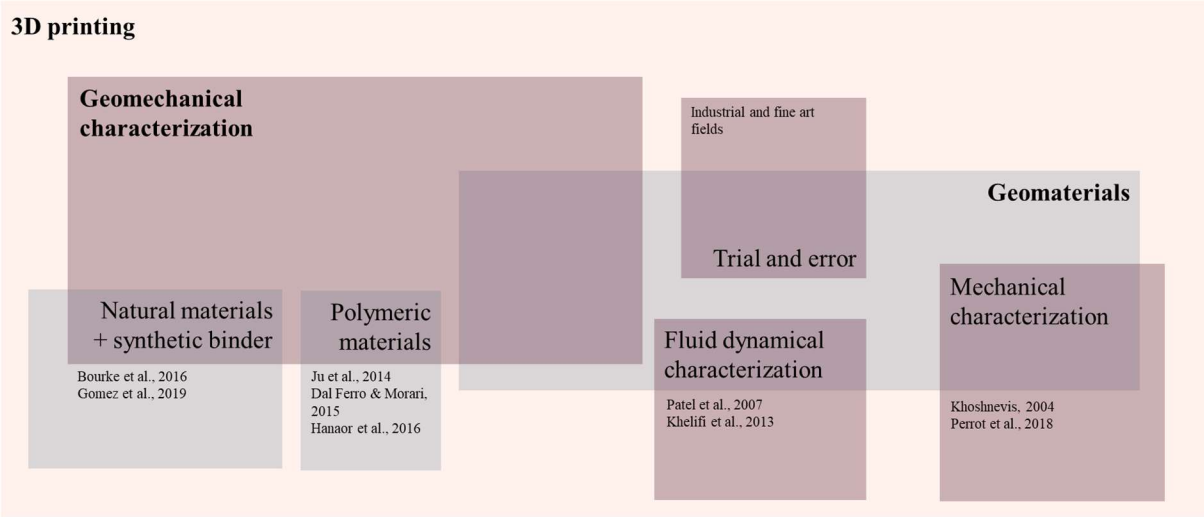

Figure 1.10 *– State of the art overview.*

With this research, a new way will be explored, considering the process of extrusion as a geomechanical one, and thus geomechanically characterizing 3D printed geomaterials (figure 1.11).

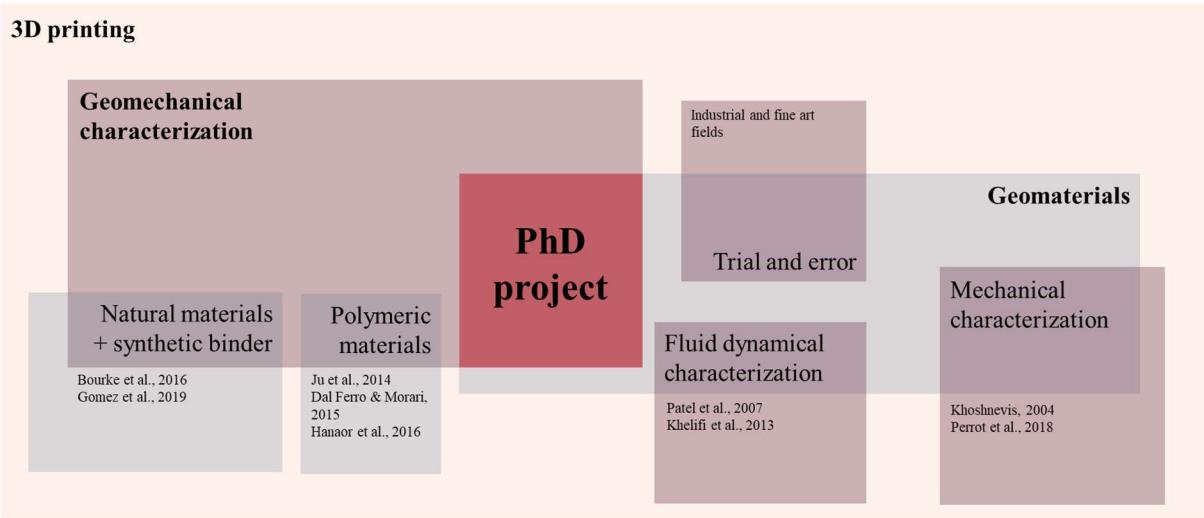

Figure 1.11 *– PhD project in the state of the art.*

2. MATERIALS USED IN THE EXPERIMENTAL PROGRAM

With the aim to explore a wide range of behaviors of the fine-grained soils related to their mineralogic composition (kaolinite, quartz, and bentonite) and to their consistency (plastic state and liquid state), three groups of fine-grained soils have been used duringthe pursuit of the objectives of this thesis:

- Commercial clay – CC: clayey soil sold to be used for artistic purposes;
- Group A: custom mixtures prepared in the Geotechnical Laboratory of the University of Palermo;
- Group B: custom mixtures prepared in the GeoSI Laboratoy of the University of Los Andes.

In this chapter, the characteristics of them are described, as to be of reference for the following chapters.

2.1 CC – COMMERCIAL CLAY

A commercial clay sold for artistic purposes was used during the testing campaign of the research project.

It has been chosen to use this kind of geomaterial because in this phase of the exploration of the use of clay as printing materials worldwide, the use of that has spread amongst the buyers of 3D printers for soils; it is indeed, the type of material that the company from which the Engineering Department of the University of Palermo sent when the DELTA WASP 2040 Clay has been bought.

Moreover, the industrial character of the PhD thesis needed that the results of the investigation conducted could've had tangible effects on the national – and regional – productive fabric. As mentioned, the second industrial partner of the Project is "Terrecotte del Sole", a company involved in the production and selling of artistic ceramics typical of the Southern Italy. The company owns a Delta WASP 4070 Clay 3D printer (the same type of 3D printer used at the University of Palermo, but with a larger printable volume), using as printing material the Commercial Clay here presented. The material was therefore furnished by them.

The Commercial Clay here described is sold in parallelepipedal humid blocks covered in a plastic film of 35 kg. The silty clay presents a water content equal to 21% when sold. While the geomaterial always needs to be humified and process prior to be used for 3D printing, the storage of it only necessitated to avoid contamination: the plastic film covering the blocks was therefore sufficient.

The material has been geotechnically identified by means of the specific gravity, the consistency limits and the grain-size distribution. In the following table 2.1 the determined properties are summarized.

Table 2.1 *– Main geotechnical properties of the soil called "CC" (specific gravity G_s, liquid limit LL, plastic limit PL, clay fraction f_{clay}, silt fraction f_{silt}, sand fraction f_{sand}).*

Soil ID	G_s	*LL*	*PL*	f_{clay}	f_{silt}	f_{sand}
(-)	(-)	(-)	(-)	(%)	(%)	(%)
CC	2.77	0.45	0.21	52	46	2

2.2 GROUP A – UNIPA CUSTOM GEOMATERIALS

Group A is composed of four mixtures of Speswhite kaolin and pulverized quartz with different proportions of dry weight of them.

It has been chosen to test mixtures of those materials because, on one hand, a good workability of the mixture is guaranteed from the presence of the kaolin, on the other hand, the quartz would increase the resistance of the mixture. Finally for both material, the maximum size of the grains has been chosen equal to 0.075 mm, so that the extrusion of the material from the smaller 3D printer nozzle owned by the Geotechnics Laboratory of the University of Palermo occurred with a reduced clogging risk.

The studied soils are thus the following mixtures:

- 100K 100% kaolin
- 90K10Q 90% kaolin – 10% quartz
- 70K30Q 70% kaolin – 30% quartz
- 50K50Q 50% kaolin – 50% quartz

The hygroscopic water content of the kaolin was determined equal to 1%. Taking that into account, the mixtures were prepared in order to obtain 2 kg for each dried mixture. To achieve a homogeneous mixture, the two materials were firstly placed on a tray, there gently and carefully mixed, to minimize dispersion in the air. The soils' mixtures were finally inserted and stored in transparent plastic bag properly sealed so that they would not be contaminated by the external environment.

Each mixture was geotechnically identified, determining the grain size distributions, reported in figure 2.1. In table 2.2 the specific gravity of them, the consistency limits, and the clay, silt and sand fractions are summarized.

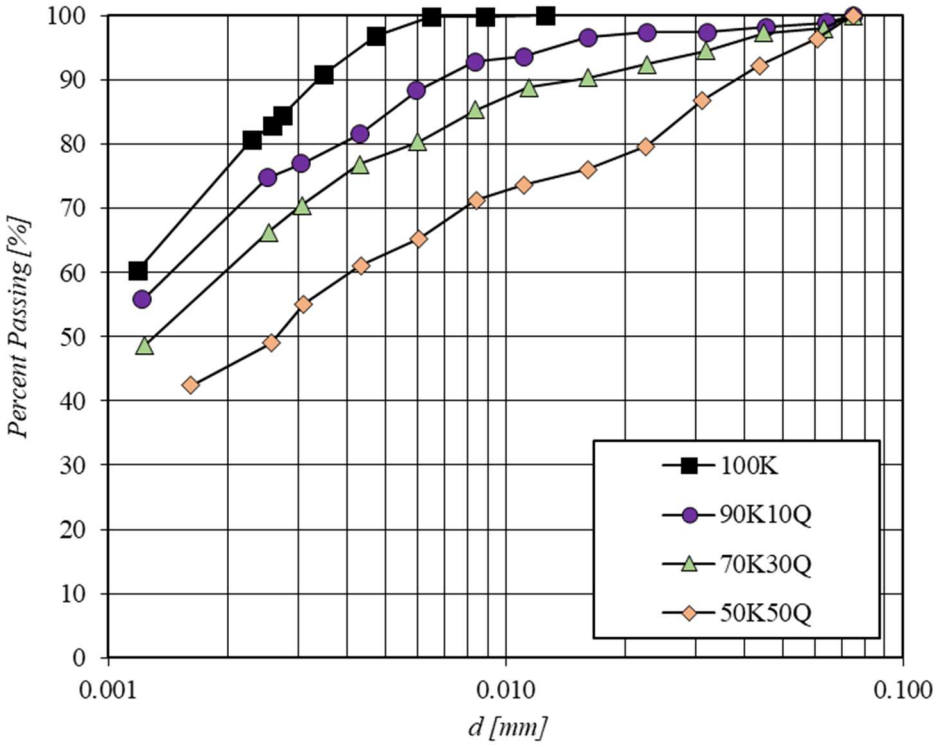

Figure 2.1 *– Grain size distribution of the soils of "Group A".*

Table 2.2 *– Main geotechnical properties of the soils of "Group A" (percentage of kaolin W_K/W_{tot}, percentage of quartz W_Q/W_{tot}, specific gravity G_s, liquid limit LL, plastic limit PL, clay fraction f_{clay}, silt fraction f_{silt}, sand fraction f_{sand}).*

Soil ID	W_K/W_{tot}	W_Q/W_{tot}	G_s	*LL*	*PL*	f_{clay}	f_{silt}	f_{sand}
[-]	*[%]*	*[%]*	*[-]*	*[-]*	*[-]*	*[%]*	*[%]*	*[%]*
100K	100	0	2.60	0.61	0.35	77	23	0
90K10Q	90	10	2.62	0.51	0.25	69	19	12
70K30Q	70	30	2.64	0.42	0.22	61	21	18
50K50Q	50	50	2.68	0.33	0.18	46	20	34

As visualized in the following figure 2.2, it appears that not only both the consistency limits of the mixtures decrease with the increase of the quartz percentage, but also the plasticity index – representing the amplitude of the plastic state - has a slight reduction with it.

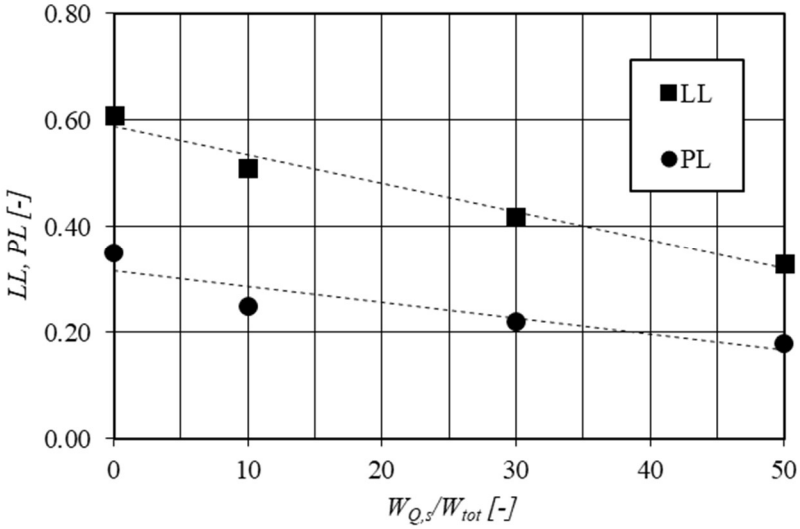

Figure 2.2 *– Decrease of the consistency limits with the increase of quartz percentage.*

2.3 GROUP B – UNIANDES CUSTOM GEOMATERIALS

Group B is composed of eight mixtures of kaolin, sodium bentonite and mineral colorants – used to differentiate the soils – with different proportions of dry weight of them (Garzón et al., 2015).

The fine-grained soils described in this paragraph have been used during the investigation phase conducted at the Geotechical Laboratory of the University of Los Andes (Bogotá, Colombia).

It has been chosen to test mixtures of those materials because they are the ones currently used by the GeoSI Group of the University of Los Andes within their investigations on the characterization of the behaviour of soils having different values of the limit liquid (e.g. Pua et al., 2018; Pua and Caicedo, 2021). The inherent geotechnical characteristics of the bentonite related to its capacity to adsorb water (e.g. Grim, 2011) make that possible.

The main geotechnical properties of the eight fine-grained soils are summarized in the following table 2.3.

Table 2.3 *– Main geotechnical properties of the soils of "Group B" (percentage of kaolin W_K/W_{tot}, percentage of bentonite W_Q/W_{tot}, percentage of colorant W_C/W_{tot}, specific gravity G_s, liquid limit LL, plastic limit PL).*

Soil ID	$W_{K,s}/W_{tot}$	$W_{B,s}/W_{tot}$	$W_{C,s}/W_{tot}$	*Gs*	*LL*	*PL*

[-]	[%]	[%]	[%]	[-]	[-]	[-]
S1	100	0	0	2.7	0.87	0.44
S2	68	23	9	2.73	1.20	0.32
S3	55	33	12	2.74	1.48	0.26
S4	44	44	12	2.75	1.96	0.24
S5	31	52	17	2.83	2.04	0.20
S6	21	63	16	2.82	2.34	0.23
S7	10	73	17	2.76	3.00	0.29
S8	0	100	0	2.84	3.48	0.30

In the following figure 2.3 can be noticed that not only both the consistency limits of the soils increase with the increase of the bentonite percentage, but also a widening of the plastic state of the soils occurs.

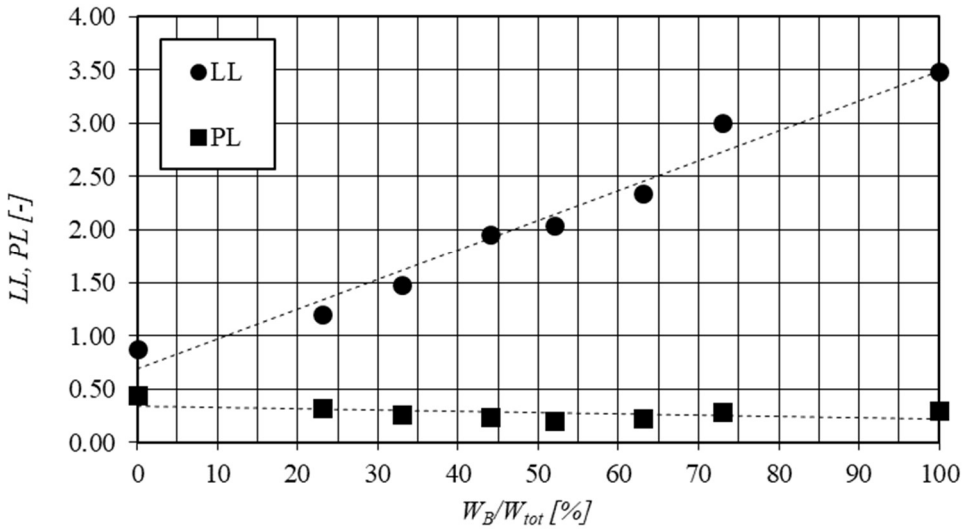

Figure 2.3 *– Increase of the consistency limits with the increase of bentonite percentage.*

In summary, the fine-grained soils used in this work are characterised by s a variety of mineralogic composition and of Atterberg limits. With the aim to ease the consultation of the next chapters, table 2.4 reports a schematization of the chapters in which the previously described soils have been tested.

Table 2.4 *– Schematization.*

Soil Group	***Where***
CC	Chapter 5, Chapter 6, Chapter 7
Group A	Chapter 3
Group B	Chapter 8

3. EXTRUSION PROCESS OF FINE-GRAINED SOILS

Extrusion of fine-grained soils represents the main process to which a soil is subjected when 3D printed. It has been therefore chosen to investigate the role played in the process by the geomechanical characteristics of the soil and by the geometry of the extrusion system.

3.1 MATERIALS

In this phase of the work, the soils belonging to the Group A composed by mixtures of kaolin and quartz, with different proportions of dry weight of them, as described on the chapter 2.2 have been tested.

It has been chosen to test the mixtures adding a weight of distilled and demineralized water as to reach a water content equal to 1.2 times the liquid limit of each of them. This value guaranteed the extrudability of the mixtures, allowing on one hand the workability of them, and, on the other hand, allowing to obtain filaments that maintained their shape once extruded.

In the following table 3.1, the characteristics of the tested soils are reported:

Table 3.1 *– Main characteristics of the studied fine-grained soils.*

Soil ID	G_s	*LL*	*PL*	*w*
[-]	*[-]*	*[-]*	*[-]*	*[-]*
100K	2.60	0.61	0.35	0.73
90K10Q	2.62	0.51	0.25	0.61
70K30Q	2.64	0.42	0.22	0.50
50K50Q	2.68	0.33	0.18	0.39

3.2 EXTRUSION TESTS

Testing set-up

The testing set-up, represented in the figure 3.1, consisted in two polyethylene extruder having internal diameter equal to 24 mm and internal area equal to 4.52 cm^2. The first of them was equipped with a polyethylene cylindrical nozzle with a diameter equal to 3.9 mm; the second one was equipped with a polyurethan nozzle with a truncated cone section, having outlet diameter of 1.2 mm and inclination of the walls equal to 7°.

Inside the extruders a ram with 80 mm stroke was housed in. The contact with the material occurred by means of a waterproof gasket; on the ram a vertical force was applied, to exert a vertical total pressure on the material inside the extruder equal to 123 kPa or equal to 217 kPa. The extruded filament was then collected in a container put on a scale with 0.01 g resolution.

The mixtures were humidified slowly adding the weight of water corresponding to the target one, working then the material on a glass support with a spatula. The extruder would then

be filled by mean of a little spatula, adding on each step circa 5 g of material; at the end of the procedure, the extruder would be weighted to determine the unit weight of the material inside of it.

During the extrusion tests, performed at a constant load, the vertical displacements of the ram and the weight of the extruded filament were measured; the extruded filament would be collected at regular volume intervals, and then placed in the oven at 105 °C for 24 hours, to quantify the evolution of the water content of the mixture during the extrusion process.

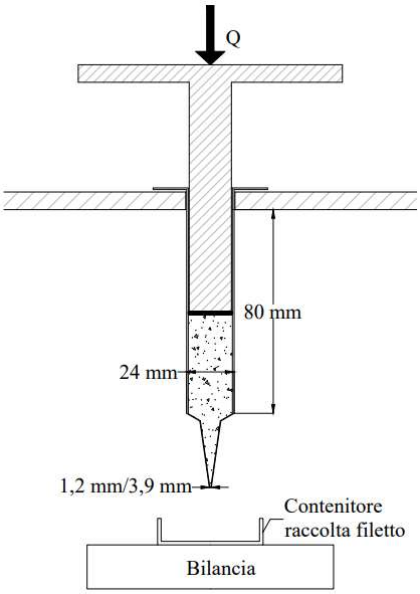

Figure 3.1 *– Testing set-up.*

To summarize:

- two extruders: d_n = 1.2 mm and d_n = 3.9 mm
- two loading pressures: P_E = 123 kPa and P_E = 217 kPa
- four mixtures of soils: 100K – 90K10Q – 70K30Q – 50K50Q

With this testing set-up, a total of 16 tests are therefore necessary to fully investigate the extrusion behaviour.

Results and analysis

In this experimental campaign, 18 extrusion tests have been performed, as two of the 16 necessary needed to be repeated.

In the following figures 3.2 and 3.3, a significant example of the variation of the unit weight of the soil inside the extruder with the advance of the ram is represented: results show that in the first steps of the test, corresponding to circa 50 mm advance, values of the unit weight stayed almost constant, while variations could be observed in the latter parts of the extrusion process.

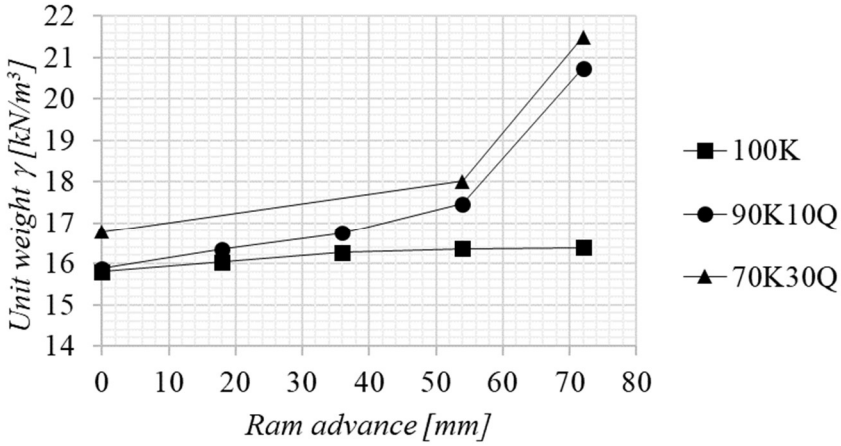

Figure 3.2 - *Evolution of the unit weight of the soil inside the extruder with the advance of the ram. Nozzle diameter d_n = 1.2 mm.*

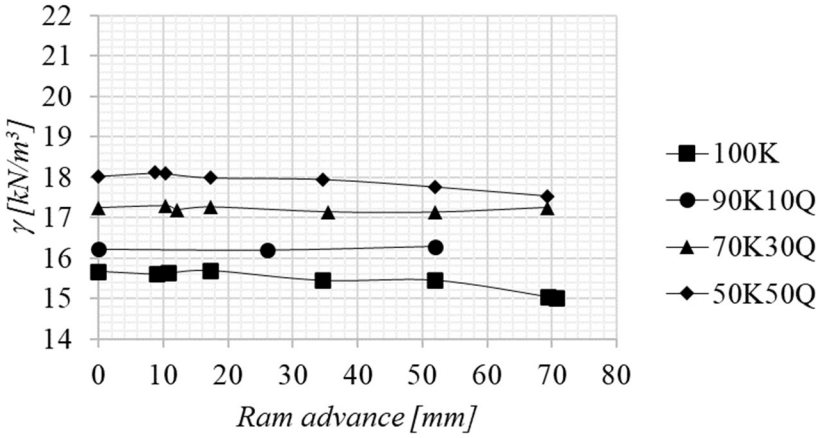

Figure 3.3 - *Evolution of the unit weight of the soil inside the extruder with the advance of the ram. Nozzle diameter d_n = 3.9 mm*

As it is noticeable in the following figures 3.4 and 3.5, overlapping the information about the unit weight of the extruded filament and the unit weight of the material inside the extruder, to a reduction of the value on the first one corresponded an increase of that on the other. This behaviour is justified considering the extrusion process as a combination of a consolidation process and an efflux process in which the densification of the soil inside the extruder is possible in relation to the dissipation of the excess pore water pressure.

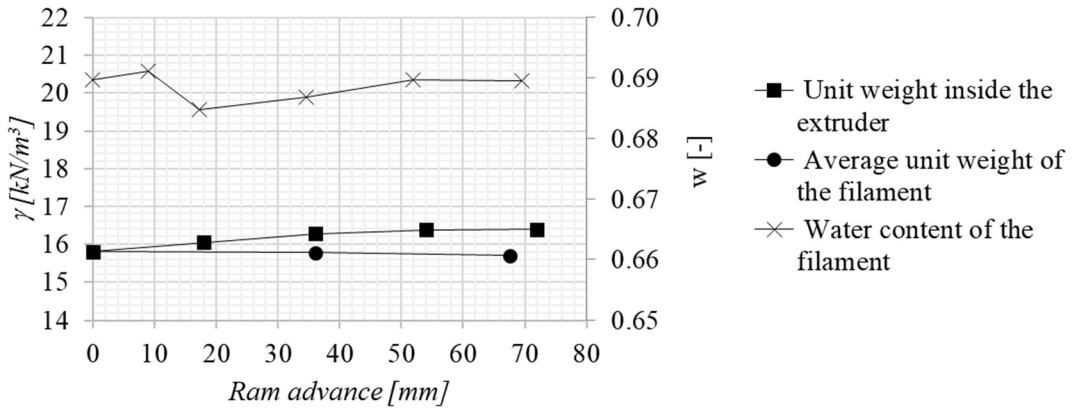

Figure 3.4 - *Evolution of the unit weight of the soil inside the extruder with the advance of the ram in relation with the water content of the filament – soil 100K.*

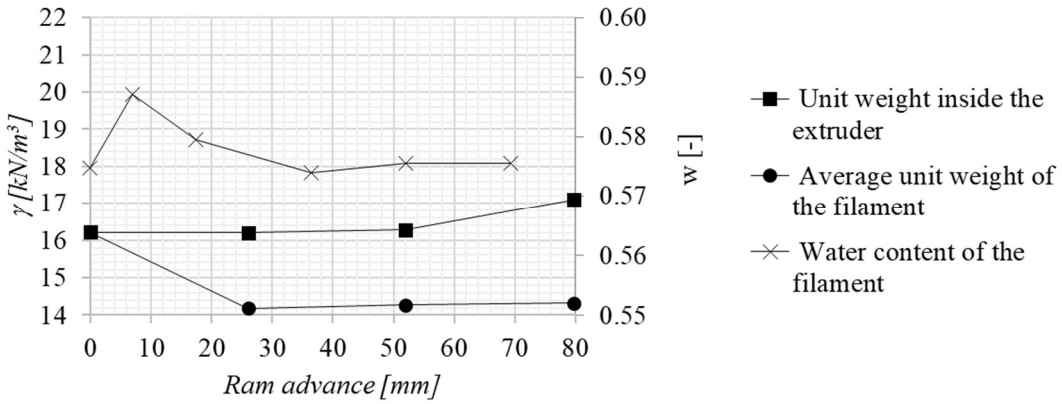

Figure 3.5 - *Evolution of the unit weight of the soil inside the extruder with the advance of the ram in relation with the water content of the filament – soil 90K10Q.*

Further evidence in this regard is obtained by comparing the results obtained from two extrusion tests carried out at the same load and with the same size of the diameter of the nozzle on the soils mixture having a quartz percentage of 10% and on the soils mixture having a quartz percentage of 50% (Figure 3.6). As the time elapsed since the start of the test increases, the change in the weight of the unit of volume of the extruded filament is more pronounced in the mixture containing more quartz.

The greater presence of the latter, in fact, increasing both the permeability of the mixture and its oedometric modulus, increases the value of the consolidation coefficient, allowing a faster dissipation of interstitial pressures and thus allowing the densification of the mixture.

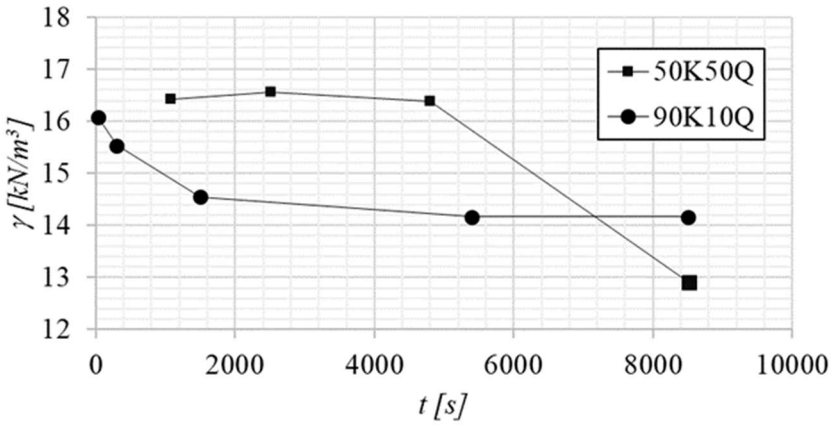

Figure 3.6 *– Evolution of the unit weight of the extruded filament with the time elapsed from the start of the test for soils 50K50Q and 90K10Q.*

An explanation on the different behaviors expressed by the mixtures can be found in the difference on mineralogy of them.

Kaolinite, the main mineral of which kaolin is composed, is a clay mineral having crystals consisting of stacked layers of tetrahedral and octahedral sheets bonded together – a 1:1 or TO structure (e.g. Klein et al., 1993). The tetrahedral sheet is composed of a silicon ion surrounded by four oxygen ions, while the octahedral sheet is composed of an aluminum ion surrounded by six oxygen or hydroxyl ions. The oxygen ions are shared between the sheets, guaranteeing a strong bond between them, while the bonding between layers is guaranteed by hydrogen bonding, The hydrogen bonding is strong enough to have up to 100 crystals stacked before a layer of water molecules would infiltrate, giving the kaolin clay its plasticity properties: under stress the crystals slip past to each other and the shape is retained after the stress is removed.

Quartz is a mineral consisting on tetrahedra consisting on a silicon ion surrounded by four oxygen ions, with each one of them shared between two tetrahedra. This form of the crystal doesn't allow any infiltration of water molecules (e.g. Klein et al., 1993).

Therefore, when the quartz is pulverized, even if the grain dimensions of it falls in the geotechnical definition of clay, the hygroscopic properties don't change. The mixture behaves then as a double-structured material in which the quartz particles are immersed in a clayey matrix. Water surrounds quartz particles and cannot penetrate the structure. It has no bond to the quartz particles. So as it is easy to surround them, it is equally easy for water to migrate from it. On the contrary, it is very difficult for water to stick to the kaolin structure, and it is on the contrary equally difficult to get away from it.

These two different characteristics lead to two different behaviors: when the soil is only composed of kaolin, or the quartz percentage is low, the soil behave as a clay in which some quartz particles are embedded, and the consolidation process is very slow because a lot of time is needed to reduce the excess pore water pressure by ejecting the water; the time in which the extrusion process occurs is therefore too limited and the process could be considered as undrained. With the increase of the quartz percentage, the soil could be described as quartz particles surrounded by clay; the consolidation process is in this case quicker and if the extrusion process is slow, the excess pore water pressure could be reduced by ejecting the water and the process could be considered as drained.

This behaviour appeared evidently when testing the soil having the highest percentage of quartz. As shown in the next figure 3.7, when the fine-grained soil mixture has only 10% of quartz, the flow is stationary almost until the complete emptying of the extruder: the emptying velocity is constant with respect to the time and the process can be considered ended within an hour. When the quartz percentage is equal to 50%, on the other side, the process is slower, up to clogging of the extruder – which permits the completion of the consolidation process, as can be seen in the next figure 3.8, where the drainage of a drop of water from the nozzle occurs.

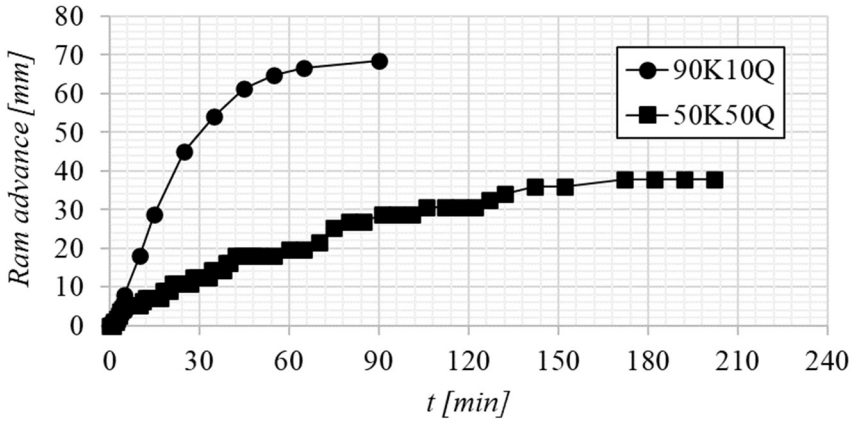

Figure 3.7 *– Advance of the ram with the time elapsed from the start of the test for soils 50K50Q and 90K10Q.*

Figure 3.8 *– Drainage of a drop of water. Soil 50k50Q..*

To confirm the occurrence of the consolidation process during the test, the water content of the soils mixture inside the extruder has been determined: 10 cm^3 of soil have been extracted from the upper part of the extruder – in the proximity of the ram – and 10 cm^3 have been extracted from the bottom part – in the proximity of the nozzle. As reported in the next table 3.2 and represented in the next figure 3.9, the water content of the soil significantly reduced in the proximity of the ram, while only a slight variation occurred in the proximity of the nozzle.

Table 3.2 *– Water content values inside the extruder before the printing process and after the interruption of the test.*

	w *[-]*	
	before test execution	after test interruption
proximity of the ram	0.39	0.33
proximity of the nozzle		0.40

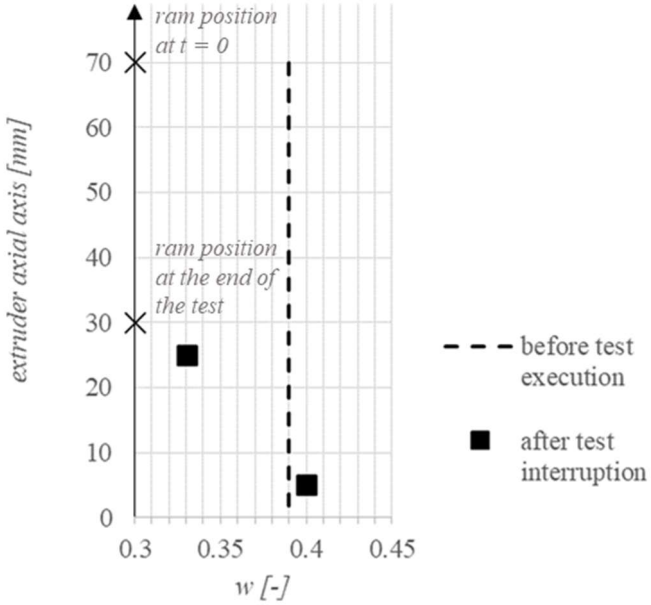

Figure 3.9 *– Water content representation before the printing process and after the failure of the test with respect to the position of the fine-grained soil 50K50Q inside the extruder.*

In the proximity of the ram, the soil undergoes a process of compaction: for the soils particles to get closer – and thus the void index to reduce –, the water needs to migrate. In the proximity of the nozzle, the presence of the ram does not influence the compaction of the soil, therefore, the water content remains constant.

3.3 OEDOMETRIC TESTS

Wroth & Houlsby (1984) proposed a criterion then confirmed by Martin et al. (2006), according to which for the extrusion process to occur without being affected by the consolidation process, the extrusion time must be at least an order of magnitude less than the characteristic filtration time – as defined by Terzaghi (1943):

$$t_{ext} < 0.1 \, \frac{H^2}{c_v}$$

To investigate more thoroughly the behavior of the mixtures subjected to the extrusion process, oedometric tests were carried out in order to derive the consolidation coefficient for each mixture and, subsequently, make a comparison with the criterion exposed.

Testing set-up

The testing set-up consists of a mechanical oedometric apparatus. In this type of machine the application of the effective vertical stress happens by putting a weight on a mechanical arm. The load is then transferred to the superior part of the cylindrical specimen, that is put in a box

filled with water. The machine is equipped with LVDT transducer linked to a software; the electrical signal is transferred to the software and the displacements are registered.

The loading path followed during the tests is reported in the following table 3.3.

Table 3.3 *– Loading and unloading steps carried out in the oedometric tests.*

	Step	***Effective stress applied***
	n.	σ'_v
	[-]	*[kPa]*
Loading	1	*0.1*
	2	10
	3	20
	4	30
	5	90
	6	189
	7	397
	8	692
	9	1280
	10	2555
	11	3786
	12	5016
Unloading	1	2555
	2	692
	3	189
	4	30
	5	10
	6	0.1

The first loading step is referred to the only application of the loading head. Each loading step had a duration of 24 hours, that was the time necessary to consolidation of the specimens to complete. In the loading phase, a geometric series for the increments has been followed, with ratio equal to two: doubling so the load applied for each step. The unloading phase followed a geometric series too, but with a ratio of four. The water level has aways been maintained constant to ensure the saturation of the specimen during the test.

Data elaboration

The data elaboration has been executed with the following layout:

- data cleansing;
- construction of the displacement vs time curves in semi-logarithmic chart for each loading/unloading step;

- identification of the ρ_0 and ρ_{100} values by means of the logarithm of time graphic method corresponding to the value of the displacement at the beginning of the consolidation process – when the average degree of consolidation is equal to 0 – and at the end of the consolidation process – when the average degree of consolidation is equal to 1;
- determination of the coefficient of consolidation c_v by means of the Casagrande graphic method;
- determination of the void index relating to the end of the primary consolidation process of each step – when the vertical displacement equal to ρ_{100} has been therefore reached;
- construction of the oedometric curves.

Data analysis

The analysis of the **vertical displacement vs time curves** is conducted on a semi-logarithmic chart in which the displacement axis is represented with positive values when a subsidence occurs.

The ρ_0 and ρ_{100} values are determined by means of the logarithm of time graphic method for each loading/unloading step to evaluate the value of the void ratio corresponding to the end of primary consolidation and to evaluate the value of the coefficient of consolidation c_v.

Specimens preparation

To obtain the specimens for the tests, the following steps has been followed.

The soils mixtures described at the beginning of this Chapter are prepared at a water content of 1.2 times the value of the liquid limit of each of them, as reported in the table 3.1, with the aim to test the same mixtures of soils at the same conditions had during the extrusion process. To give a slight compaction, they are then put on a modified permeameter (figure 3.10) having a diameter size wider than the one of the oedometer ring and they loaded with the only loading head for three days. After this last operation, the oedometer ring was slipped inside the permeameter to derive the specimen to be tested in the oedometer.

Figure 3.10 *– Picture of the modified permeameter used to slightly compact the fine-grained soils.*

Results and analysis

The oedometric curves derived for the soils mixtures are represented in the following figures 3.11, 3.12, 3.13.

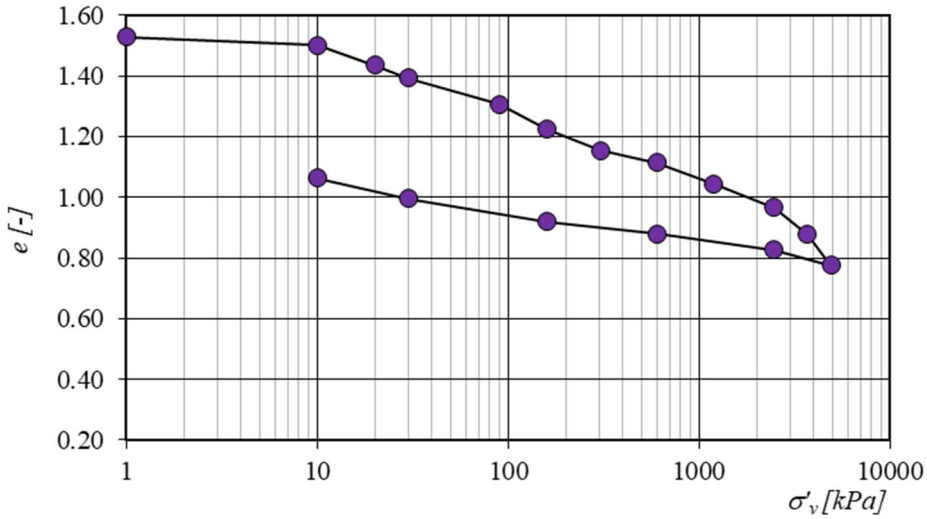

Figure 3.11 *– Oedometric curve – 90K10Q.*

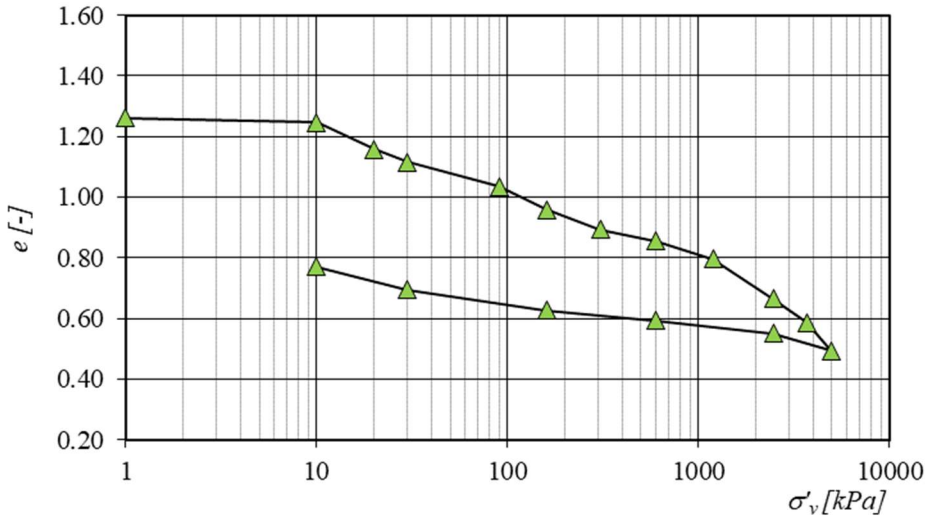

Figure 3.12 *– Oedometric curve – 70K30Q.*

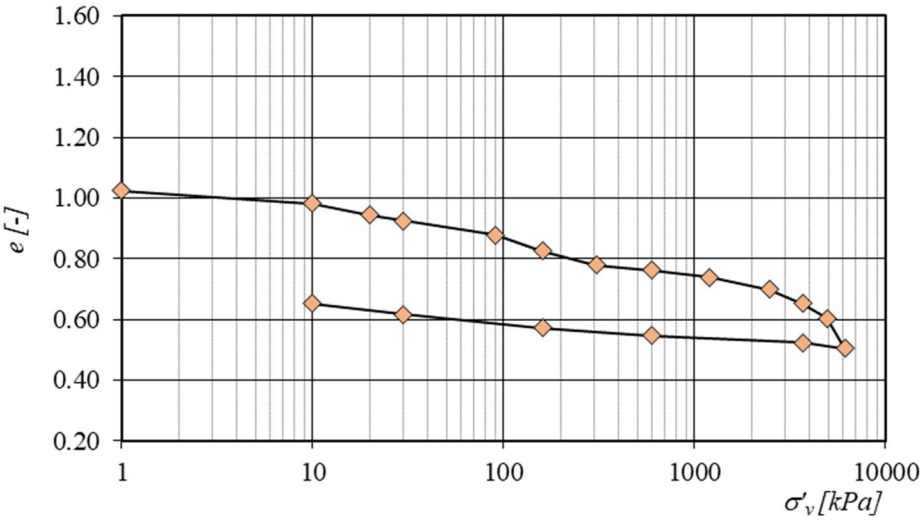

Figure 3.13 *– Oedometric curve – 50K50Q.*

Table 3.4 shows the values of the coefficients of consolidation c_v determined for the loading step n. 6, in which the effective pressure applied to the specimen (189 kPa) corresponds to a little more than the average pressure applied during the extrusion tests – equal to 123 kPa and 217 kPa.

It is now possible to make some considerations about the extrusion process of the mixtures seen in the previous paragraphs. All the completed extrusion tests presented a duration of the magnitude of a couple of minutes, while the two unfinished tests related to the mixtures 70K30Q and 50K50Q had durations of the magnitude of hours. Knowing the relevant coefficient of consolidation of the soils mixtures, the characteristic time can be computed and compared with the extrusion time accordingly to the criterion exposed by Wroth & Houlsby (1984). To do so, the filtration length has been considered equal to the extruder height, as 80 mm, and extrusion time has been estimated equal to 60 seconds for the soils mixtures in which the extrusion process completes, and equal to 21600 seconds (6 hours) for the soils mixtures in which the process stops. The data are collected in the table 3.4, and, as can be seen, there is accordance between the predictions of the Wroth & Houlsby criterion and the experimental experience.

When designing an extrusion process, it would therefore be recommended to verify that the expected duration of that would be ten times shorter than the characteristic time of the process, depending on the geometry of the extruder and on the soils characteristics.

Table 3.4 *– Coefficient of consolidation c_v and Wroth and Houlsby criterion for the soils mixtures.*

	$c_{v,189\,kPa}$ [mm²/s]	$t_{ext} / (H^2/c_v)$ [-]
90K10Q	0.8	0.01
70K30Q	1.3	4.39
50K50Q	1.15	3.88

3.4 SUMMARY

The extrusion tests carried out on the four selected soils provided an overview of how the extrusion process is affected by the considered variables. Considering soil extrusion as a combination of consolidation and efflux, for consolidation to take place, excess pore water pressures induced by the application of the constant load must be able to dissipate – in that case a failure of the extrusion process is experienced. When this condition is reached (more visible in the presence of the extruder having a smaller nozzle diameter) a thickening of the soils mixtures within the extruder is observed, which corresponds to an increase in the unit weight within them, compensated by a decrement of the same in the extruded filament. The determination of the water content of the filament confirmed this trend, observing a correlation between the initial increase in the water content and the decrease in the unit weight of the filament.

Combining these results with the information provided by the observation of the extrusion process over time, it was finally observed how the presence of quartz affects the behavior of the mixture towards thickening. Comparing, under the same conditions, the behaviour of the two mixtures with a lower and higher percentage by weight of quartz, it was observed that the reduction of the unit weight of the filament occurs more quickly in the second case, with the presence of quartz speeding up dissipation of the excess pore water pressure leading to the failure of the extrusion process. The reduction on the water content of the soil located inside the extruder in the proximity to the ram confirmed the occurrence of the water migration inducted by the consolidation process occurred.

A set of oedometric tests has been finally executed to deeply investigate the hydromechanical behaviour of the selected mixtures of soils, verifying that the Wroth & Houlsby criterion (1984) is capable to predict the outcome of the extrusion process, relating the geomechanical characteristics of the soil with the geometry of the extruding system.

4. 3D PRINTING OF SOILS, HOW-TO

A significant part of this work has been dedicated to develop the necessary skills for the purpose of 3D printing the soils - consisting on the learning of the functioning principles of the types of 3D printers used in this work, and on the learning and on the acquisition of a mastery on the programming languages used to code.

Scope of this Chapter is therefore to present to the reader the innovative technology used during the PhD research project: in the first part of the chapter, the 3D printers with which the work has been conducted are first presented and described; in the second part of it the GCODE language – used to write the codes describing the printed samples – is described and finally, the ways in which the G-codes have been written for this work are explained – from scratch and encoding them through a script written in Python language.

In the further course of this work, *"GCODE"* written in uppercase will indicate the programming language, while *"G-code"* written in sentence case and indented will indicate the resulting file.

Examples of the G-codes used in this work are available in the Annexes and at the following link:
https://drive.google.com/drive/folders/10qUUwVNcvvtEWXra8ip_UElZIYifOrSk?usp=sharing.

4.1 3D PRINTERS FOR SOILS

3D printers for soils are not so common in the commercial area at this time. Mostly, whenever in the academic field the scope of 3D printing of soils has been reached, other kind of printers have been modified in order to work with clayey material, as happened for instance at the Institute of Advanced Architecture of Catalunia, where an anthropomorphic robot is modified to permit extrusion of the soil.

In this research, two kind of 3D printers have been used: the first one is a commercial 3D printer produced by the DELTA CSP company, commercialized properly for the printing of clay and usually bought from ceramic industry or artists. The second one is a custom-one built in the GeoSI Lab of the University of Los Andes. This two 3D printers have substantial differences that will be here deepened.

Delta WASP 2040 Clay and Delta WASP 4070 Clay

The Delta WASP 2040 Clay (figure 4.1) is the 3D printer bought for the Geotechnical Laboratory of the Engineering Department of the University of Palermo for the development of the Research Project here presented.

The Delta WASP 4070 Clay is the 3D printer owned by the industrial partner of the Research Project, "Terrecotte del Sole S.r.l.".

Figure 4.1 *– Delta WASP 2040 Clay 3D printer.*

The two 3D printers only differ on the dimensions of the maximum printing volume, while the printing system is the same.

The printing system (schematized in figure 4.2) is composed by a 3-liter air-tight tank, in which an air-pressurized ram moves the soil toward the extruder; the extruder is fixed on a horizontal plate connected to three rollers that with independent translations permit the movement of the extruder on the three dimensions covering a printing volume of a cylinder with a diameter of 20 cm and a height of 40 cm, in the case of the Delta WASP 2040 Clay or of a cylinder with a diameter of 40 cm and a height of 70 cm, in the case of the Delta WASP 4070 Clay. The efflux of the material reaching the extruder occurs thanks to the rotation of an endless screw located inside the extruder connected to a stepper motor – schematized in figure 4.3.

In this kind of 3D printers, therefore, the pressure applied on the material in the tank is needed only to permit to the material to reach the extruder; the extrusion of the material depends on the rotational speed of the endless screw.

The Delta WASP Clay 3D printers incorporate a Marlin firmware by which it is possible to control both the movements on the three direction of the extruder and – indirectly – the rotational speed of the endless screw by mean of the G-code.

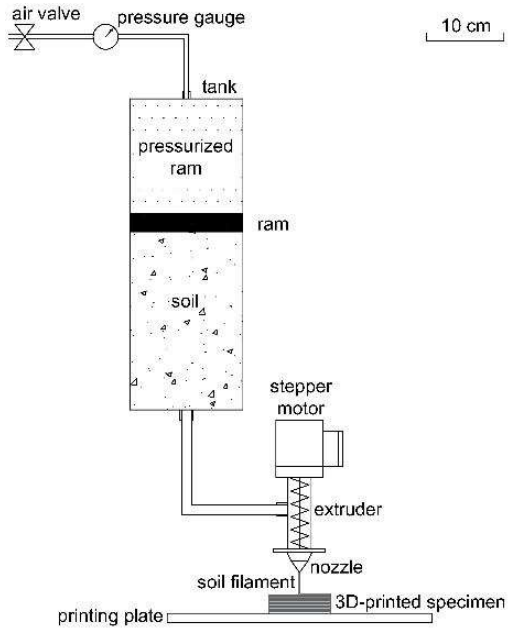

Figure 4.2 *– Schematization of the Delta WASP 2040 Clay 3D printer.*

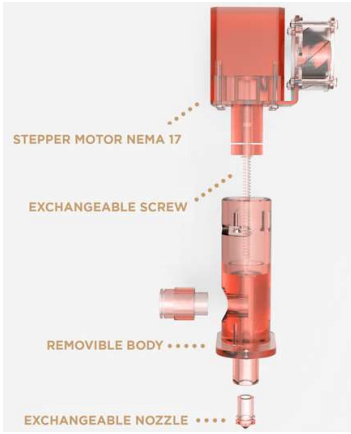

Figure 4.3 *– Schematization of the extruder of the Delta WASP 2040 Clay 3D printer.*

Delta WASP 2040 Clay operating instructions

The necessary procedures to be carried out to perform a 3D printing with the Delta WASP 2040 Clay located in the Geotechnical Laboratory of the University of Palermo are here described:

Tank filling

The air-tight tank of the 3D printer is composed by a steel tube inside of which a polyurethan disk equipped with two o-rings can move. The two ends of the tank present lids at the base of each of whom an o-ring is located. To ensure the correct blockage of the two lids, the steel plates composing them has a diameter larger than the tank as to include four external holes in

which one of them a threaded bar can be ubicated joining safely the two ends. The connection of the tank to the 3D printer structure is realized through the joint of the superior part of the tank to a mobile flange on the superior part of the 3D printer structure. The two lids differs for the presence of two holes: the upper one permits the connection to the air-pressure system by mean of a pipe. The second one permits the connection with the output pipe, in which the fine-graine soils are sent. The pressurized air is provided to the system by an in-house compressor: the pressure is regulated from an external valve equipped with a displayed pressure-gauge in which the actual pressure can be read. The valve is connected to the air-tight tank by mean of a pipe in which a valve has been installed to isolate the system, having thus an additional safety pressure barrier. It is possible to introduce air with a pressure of 13 bar; anyway following the safety instructions of the producer, 7 bar has been the maximum value of pressure with which the work has been carried out.
To fill the tank is firstly necessary to disconnect it from the system and take it apart. First, once the pressure is zeroed, the two pipes are disconnected from the two lids; then the threaded bars are removed and the two lids can be removed. The ram is then pushed till the end of the tank and is therefore removed. The technique used to fill the tank with the fine-grained soils at the plastic state consists on the previous preparation of the material with the required water content and on the forming of a quasi-cylindrical mass having a diameter superior to the one of the tank. The mass is drive by a cylindrical tube having the same diameter of the tank, and the material on the inside is finally pushed inside the tank by mean of a wooden piston. Once the material is inside the tank, the ram is inserted from the base filled with the material, in order to avoid any air occlusion that will interfere with the correct printing. The lids can be installed again and the connection to the pipes can be carried out.

3D printer height setting

The setting of the height is necessary to ensure that the Z-coordinates required by the G-code would fit together with the distance of the nozzle to the printing base. To do so, it is necessary to power on the 3D printer and act through the internal software of the machine. Once opened the command of the regulation of the height, it will be possible to move the extruder by mean of the wheel with whom the 3D printer is equipped. Clicking on it, it is possible to choose the resolution of the movement: for the first steps of movement, a low resolution is used, when the extruder is at a distance from the printing base of less than one centimeter, the highest resolution of the movement is needed. To choose the correct height, this technique has been used during this work: a sheet of paper is posed on the printing base, the correct height would be the one before the clogging of the sheet of paper between the extruder and the printing plate. The correct height is finally saved on the machine software. It is important to repeat this procedure every time the printing base changes or is moved.

Extruder chamber filling

Once the tank is filled and the correct height is set, it is necessary to fill the extruder chamber before the beginning of the 3D printing, otherwise during the first movements, the extrusion of the fine-grained soil wouldn't occur. To do so, first the required pressure is imposed through the compressor to the ram; then from the 3D printer menu, the extrusion command is selected. Moving the wheel, the value of the positions of the E-axis (further specified) will increase. In this phase it is important to rotate the wheel slowly, assuring that the screw inside the extruder would rotate properly. Once the fine-grained soil starts to flow, the extruded filament can be cut and the 3D printing can begin.

UNIANDES custom multimaterial 3D printer

The multimaterial 3D printer for soils of the Geotechnical Laboratory of The University of Los Andes has been developed and built by the Research Group there operating (Pua et al., 2018).

The printing system (figures 4.4 and 4.5) is composed of eight independent 2.3-liter air-tight tanks converging through pipe of 10 mm of diameter into a commercial hydraulic multiplexor valve having eight inputs and one output. The multiplexor valve is connected to a plate able to move on the three dimension with a precision of 0.1 mm, covering a printing volume of 30 cm x 30 cm x 30 cm. To the valve is connected an interchangeable nozzle.

In this 3D printer the efflux of the soil in the tank is guaranteed by stepper motors that control the ram displacement in each tank: the soil flows to the multiplexing valve and the filament is printed.

In this configuration of the 3D printer, the movements on the three dimension of the multiplexor and the switch amongst the tanks is controlled by the G-code, while the rotational speed of the stepper motors is controlled by an external software.

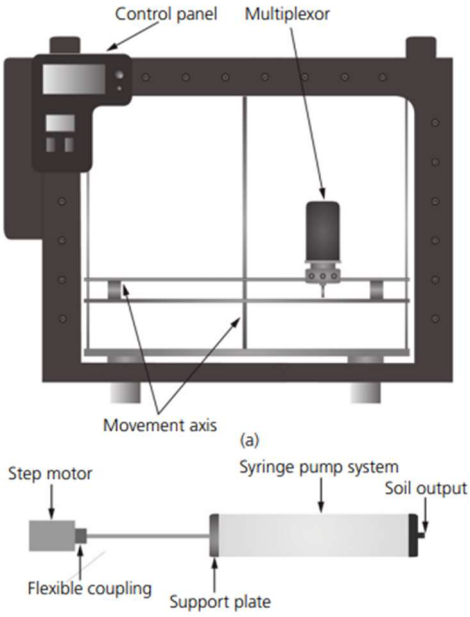

Figure 4.4 *– Schematization of the printing system of the custom multimaterial 3D printer for soils developed by the GeoSI Group at the University of Los Andes.*

Figure 4.5 *– Picture of the custom multimaterial 3D printer for soils developed by the GeoSI Group at the University of Los Andes.*

4.2 GCODE PROGRAMMING LANGUAGE

The GCODE is a computer numerical control (CNC) high-level programming language, used to control a variety of computer-aided machines like mills, lathes and 3D printers.

The language program has been developed in 1958 at the Massachusetts Institute of Technology, with the aim of control a 2-axis plotter. It rapidly spread all over the world, and it is nowadays one of the most ancient programming languages still used. The standard that this language follows is the ISO 6983, and when a new machine is manufactured, the controls of it are built according to that.

With the GCODE language is possible to write the G-code files – or simply G-codes – in the instructions telling the machine every information about e.g. the path to follow, the speed of the movements, the tool to be used, are stored.

In the next part of this section, a description of the elements composing the GCODE language is given, so that a common thesaurus could be considered in the developing of this work.

GCODE programming language elements

A G-code file consists of a list of lines in which, on every line a command is given; the 3D printer would complete the execution of the commands in the order in which they are reported.

The smallest unit of the G-code is the ***character***, being that digits from 0 to 9, capital letters (also called addresses) and symbols. A combination of one capital letter, digits and eventually symbols forms a ***word***, that is the instruction unit. Multiple words one after the other in a logical order form a ***block***, thus being a series of instructions executed simultaneously. In the G-codes for 3D printing, generally, and in this work in particular, the first word of a block tells how the action needs to be performed (here called *how-word*), while the successive words of the block

give information about the action itself (here called *what-words*). The program is finally constituted from a list of blocks – one for each line.

Being the G-code a programming language well-used in many industries having different purposes, it comprehends a long list of commands; in this section only the ones used in this project will be described.

Characters used

- Digits: `[0 - 9];`
- Letters – or addresses: `[G, M, T]` to form how-words, `[X, Y, Z, E, F, P, T]` to form what-words. In particular:
    - `G` is the address used to give preparatory instructions;
    - `M` is the address used to give miscellaneous instructions;
    - `T` is the address used to indicate the tool to be used;
    - `X, Y` and `Z`, are the addresses representing the position in the X- Y- and Z-axes;
    - `E` is the address representing – in standard 3D printing - the quantity of the used polymeric filament. This value has been re-interpreted to take into account the use of soil as printing material; in this work `E` is the address representing the soil flow;
    - `F` is the address used to assign the printing velocity, that is the velocity of the movements along the X- Y- and Z-axes;
    - `P` and `T` (the latter, when used in what-words) are the addresses used to give instructions about time;
- Symbols: `[+, -, .]` to form *how-words*, and in particular to describe real numbers (positive values, negative values, decimal point), `[;]` used at the end of a block to indicate that from that point the comments begin.

Every character can be used in the comment section of the code.

Words used

The following *how-words* with the related *what-words* have been used in the G-codes created to fulfil the aim of this Thesis, the meaning of which is here described:

- `G0` – rapid positioning; with this command it isn't guaranteed that the movement would follow a straight line, so it has been used only when movements without extrusion would have occurred. It has been used only when printing velocity was assigned or when the first position of a layer needed to be achieved.
- `G1` – linear interpolation; this command guarantees that the action would take place following a linear interpolation: straight lines are therefore assured when going from a generic point A to a generic point B. It has therefore been used in every movement in which extrusion occurred.
- `G21` – use of metric values; it is a preliminary command. It is used in the first blocks of the G-code and informs that the values of the what-words need to be expressed accordingly to the metric system.
- `G28` – home all axes. The command moves the extruder to the home position of its X, Y and Z axis. It is a tricky command because it is dependent on where the home of the axis has been set, not necessarily the home of the axis coincide with

the origin of them, e.g., the Delta WASP 2040 Clay had its home at (X, Y, Z) = (0, 0, 250 mm), while the Uniandes Custom Multimaterial 3D printer had its home at X, Y, Z = (0, 0, 20 mm).

- `G90` – use absolute coordinates for the X-, Y- and Z-axes;
- `G92` – zero the E-axis;
- `M82` – use absolute coordinates for the E-axis;
- `M84` – disable motors;
- `M201` – set the maximum acceleration for the X-, Y- and Z-axes

4.3 G-CODE GENERATION

For the common 3D printers working with polymeric filament, there is a wide range of slicing software (e.g. Cura, Slic3r, Simplify3D etc…) that would allow the final user to create the G-code starting with a 3D model of the object to craft: importing the 3D model in the software and acting on the settings of the program, the slicer software would break down the 3D model in horizontal layers of constant thickness and would return the G-code file in which the reproduction of the model is guaranteed with the 3D printer.

This kind of programs do a very good job when they are used with standard 3D printers and standard materials: the web is filled with forums in which almost every question finds its answer thanks to the experience of the community working with it and on it.

In the case of this research project, however, neither the 3D printers used, nor the printing materials are standard. It has been therefore chosen, considering the simple structure of the samples to be printed, to write the G-codes from scratch programming them with Microsoft Excel and copying it on a *.txt file then saved as *.GCODE, not using the available slicing software; in one case the G-codes have been programmed using the Python programming language.

Breaking down the G-codes programmed in this research project, they are constituted by three main parts:

- 3D printer priming – where the 3D printer initial setting instructions are written. These blocks of the G-code would be the same when using the same 3D printer;
- Body of the G-code – where the positioning instructions are written. In the bodies' blocks of the programmed G-codes, only information about the successive positions of the four axis are given. It has been chosen to use absolute positioning for the X-, Y- and Z-axis, while for the E-axis it has been chosen to use relative positioning. Every block would start with a G1 command, to ensure the linearity of the execution of the commands.
- 3D printer powering down – where the 3D printer initial setting instructions are written. These blocks of the G-code too would be the same when using the same 3D printer.

Four bodies structures have been programmed, and are here described.

Point

The body is constituted of two blocks. In the first block the absolute geometrical coordinates of the point to reach are given. The extrusion axis is set to 0.

In the second block the geometrical coordinates of the point remain the same and can be therefore omitted, while the E-axis moves to its final position related to the desired extruded volume.

The body of a punctual extrusion performed from the point (10, 20, 100) would appear like that:

- `G1 X10 Y20 Z100 E0`
- `G1 E100`
-

Line

The body is constituted of two blocks: in the first block the absolute geometrical coordinates of the first point of the line are given and the E-axis is set to 0. In the second block, the geometrical coordinates of the last point of the line are given; if one of two geometrical coordinates remain the same, they can be omitted; the relative position of the E-axis is calculated as the length of the extruded line.

The body of a linear extrusion performed from the point A = (10, 20, 7) to the point B = (30, 20, 7) would appear like that:

- `G1 X10 Y20 Z7 E0`
- `G1 X30 Y20 Z7 E20`

Alternatively, the second block can be written as:

- `G1 X30 E20`

Figure 4.6 gives a representation of the coded line on a horizontal plane.

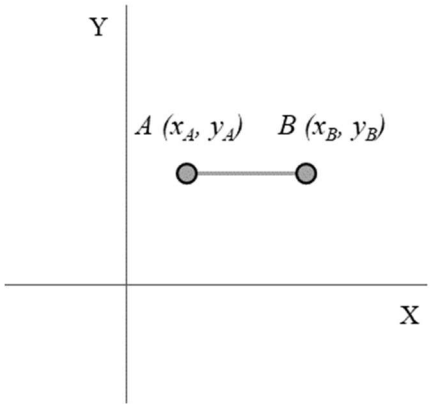

Figure 4.6 *– Representation of the coded line on a horizontal plane.*

Square

The body is constituted by five blocks: the first stores the geometrical information of the first point of the square and the E-axis is set on 0; the next ones store the geometrical information of the successive ordered vertices of the square, the last position corresponding to the first one, to close the square. The position of the E-axis would increment each time of the length of the path covered.

For a square with vertices equal to A = (0, 0, 5), B = (10, 0, 5), C = (10, 10, 5), D = (10, 0, 5), the following body would have been programmed:

- `G1 X0 Y0 Z5 E0` ; point A
- `G1 X10 Y0 Z5 E10` ; point B
- `G1 X10 Y10 Z5 E20` ; point C
- `G1 X0 Y10 Z5 E30` ; point D
- `G1 X0 Y0 Z5 E40` ; point A

Figure 4.7 gives a representation of the coded square on a horizontal plane.

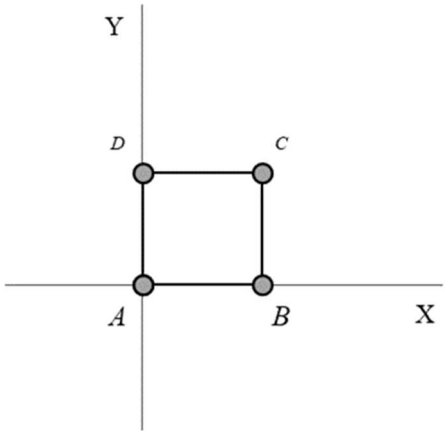

Figure 4.7 *– Representation of the coded square on a horizontal plane.*

Choosing a barycentric reference system, the problem can be simplified thanks to the axial-symmetry of the square: it is indeed possible to consider an unique maximum absolute value "*ABS*" to assign to the x and y coordinates. As shown in figure 4.8, the coordinates of the points would be:

- *(-ABS, -ABS) point A*
- *(+ABS, -ABS) point B*
- *(+ABS, +ABS) point C*
- *(-ABS, +ABS) point D*
- *(-ABS, -ABS) point A*
-

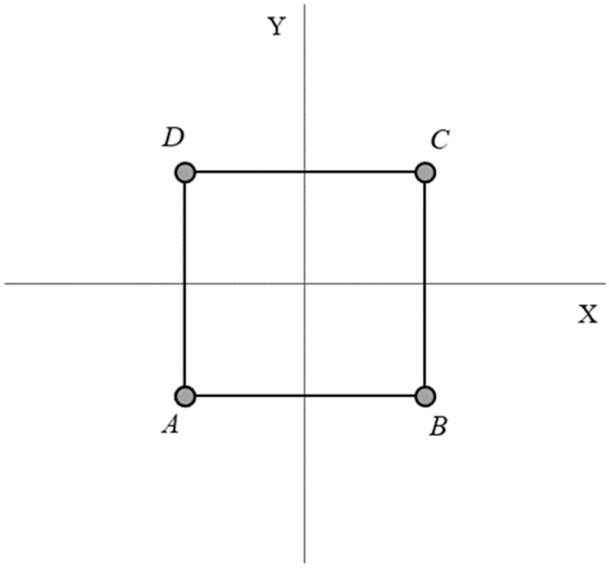

Figure 4.8 *– Representation of the coded square on a horizontal plane considering a barycentric reference system.*

Fixating the parameters "ABS" as the maximum absolute value of the x and y coordinates, the coordinates of the points would be determined by multiplying the ABS value to a here called "*matrix of signs*":

$$\text{ABS} \cdot \underbrace{\begin{bmatrix} -1 & -1 \\ +1 & -1 \\ +1 & +1 \\ -1 & +1 \\ -1 & -1 \end{bmatrix}}_{\textit{matrix of signs}} = \underbrace{\begin{bmatrix} -\text{ABS} & -\text{ABS} \\ +\text{ABS} & -\text{ABS} \\ +\text{ABS} & +\text{ABS} \\ -\text{ABS} & +\text{ABS} \\ -\text{ABS} & -\text{ABS} \end{bmatrix}}_{\textit{matrix of coordinates}}$$

The MS Excel file used to construct the square body structure is available at the following link:

https://drive.google.com/drive/folders/10qUUwVNcvvtEWXra8ip_UElZIYifOrSk?usp=sharing

Serpentine

With this term is here indicated a continuous filament covering the area of a square with a series of equidistant parallel lines, called *arms* connected to each other with orthogonal lines. The length of the arms and the distance amongst the barycentric line of two successive arms, called *inter-axis*, are constant (figure 4.9).

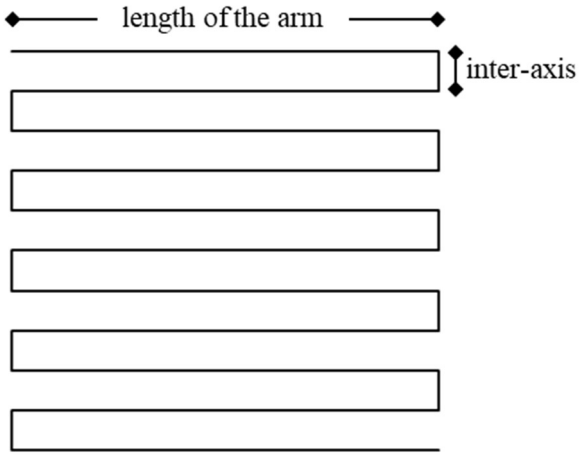

Figure 4.9 *– Schematization of the serpentine.*

The body structure of the serpentine is constituted by a number of blocks equal to twice the number of arms.

The first block stores the geometrical information of the first point of the serpentine and the E-axis is set on 0; the next ones store the geometrical information of the successive ordered vertices of the serpentine. The position of the E-axis would increment each time of the length of the path covered.

The scalability of this body structure allowed to automatize the coding of it. As it can be seen in figure 4.10, the serpentine can be seen as an iterative translation of the first main structure in which:

- the coordinates of the beginning point are the minimum x value and the maximum y value;
- the coordinates of the first point are the maximum x value and the maximum y value;
- the coordinates of the second point are the maximum x value again and the maximum y value decreased by the value of the inter-axis
- the coordinates of the third value are the minimum x value and the maximum y value decreased by the value of the inter-axis;
- the coordinates of the fourth value are the minimum x value and the previous value of the y decreased by the value of the inter-axis.

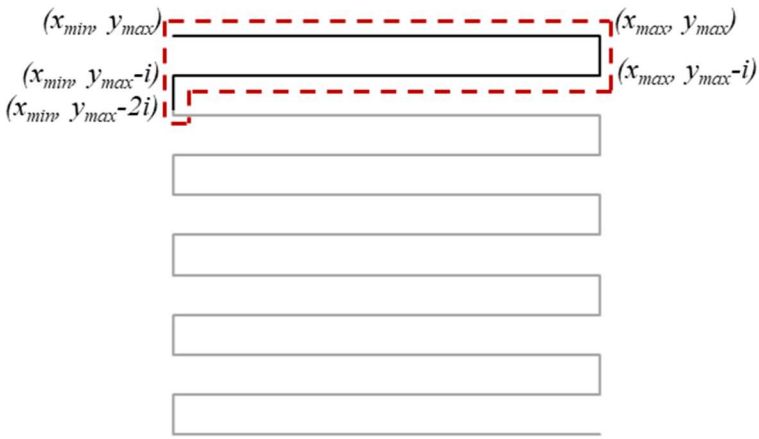

Figure 4.10 *– Scalability of the serpentine structure.*

Choosing a barycentric reference system, the problem can be simplified thanks to the double symmetry of the serpentine: it is indeed possible to consider an unique maximum absolute value "*ABS"* to assign to the x and y coordinates. As shown in figure 4.11, the coordinates of the points would be:

- *(-ABS, +ABS)* *beginning point*
- *(+ABS, +ABS)* *first point*
- *(+ABS, +ABS-i)* *second point*
- *(-ABS, +ABS-i)* *third point*
- *(-ABS, +ABS-2i)* *fourth point*

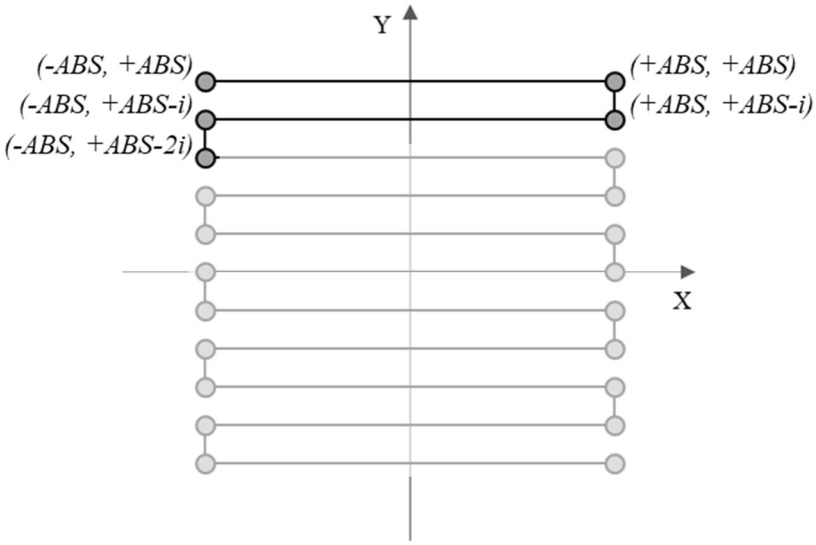

Figure 4.11 *– Scalability of the serpentine structure depending on only two parameters.*

Fixating the parameters *"ABS"* as the maximum absolute value of the x and y coordinates, and *"i"* as the inter-axis of the arms, the coordinates of the beginning point would be determined

multiplying the ABS value for a here called *"matrix of signs"*, in order to assign the negative and positive values to the coordinates:

$$ABS \cdot \begin{bmatrix} -1 & +1 \end{bmatrix} = \begin{bmatrix} -ABS & +ABS \end{bmatrix}$$

The coordinates of the successive points would be determined by multiplying the ABS value to a here called *"matrix of signs"*, adding the result to the here called *"matrix of displacements"* in which the inter-axis value appears:

$$ABS \cdot \underbrace{\begin{bmatrix} +1 & +1 \\ +1 & +1 \\ -1 & +1 \\ -1 & +1 \end{bmatrix}}_{\textit{matrix of signs}} + \underbrace{\begin{bmatrix} 0 & 0 \\ 0 & -i \\ 0 & -i \\ 0 & -2i \end{bmatrix}}_{\textit{matrix of displacements}} = \underbrace{\begin{bmatrix} +ABS & +ABS \\ +ABS & +ABS-i \\ -ABS & +ABS-i \\ -ABS & +ABS-2i \end{bmatrix}}_{\textit{matrix of coordinates}}$$

The matrix of coordinates is then iteratively added to the matrix of displacements until the ending point coordinates are reached, those one determined as follows:

$$ABS \cdot \begin{bmatrix} -1 & -1 \end{bmatrix} = \begin{bmatrix} -ABS & -ABS \end{bmatrix}$$

Once the X and Y coordinates are known, the E coordinates would be calculated as the cumulative distance amongst two successive points.

Concatenating the values with the relevant letter (X for x-coordinates, Y for y-coordinates and E for the cumulative distances), the G-code of the serpentine structure is ready.

The MS Excel file used to construct the serpentine body structure is available at the following link:
https://drive.google.com/drive/folders/10qUUwVNcvvtEWXra8ip_UElZIYifOrSk?usp=sharing

4.4 G-CODE GENERATION WITH PYTHON

During the testing campaign carried out at the Geotechnical Laboratory of the Engineering Department of the University of Palermo, it has been chosen to test specimens with a 3D orthogonal grid, i.e. constituted of layers of parallel adjacent filaments, each layer rotated of 90 degrees on the vertical axis with respect to the precedent one.

To obtain specimens with those characteristics, it has been chosen to 3D print squared samples having a serpentine structure with length of the arms higher than the maximum length of the specimen to be derived, so that the extremal portions of the serpentines in which the filament changes direction would have been excluded from the derivation of the specimens. Odd layers have been printed with the arms of the serpentines parallels to the x-direction; even layers have been printed with the arms of the serpentines parallels to the y-direction. It has been noted, however, that the change in direction of the 3D printer in the extremal part of the serpentines would drag sometimes the filament, causing some instabilities on the geometry. To remedy this inconvenience, it has been chosen to print firstly two squared rings, the internal one first, the external one then.

The structure of the G-code of these samples would be:

- 3D printer priming;
- layer number 1 (figure 4.12a):
    - internal square printing:
        - first position taking;
        - internal square printing;
        - end position taking;
    - external square printing:
        - first position taking;
        - external square printing;
        - end position taking;
    - x-serpentine:
        - first position taking;
        - x-serpentine printing;
        - end position taking;
- layer number 2 (figure 4.12b):
    - internal square:
        - first position taking;
        - internal square printing;
        - end position taking;
    - external square printing:
        - first position taking;
        - external square printing;
        - end position taking;
    - y-serpentine:
        - first position taking;
        - y-serpentine printing;
        - end position taking;

And so on, until the final height of the sample is reached. At the end:

- 3D printer powering down.

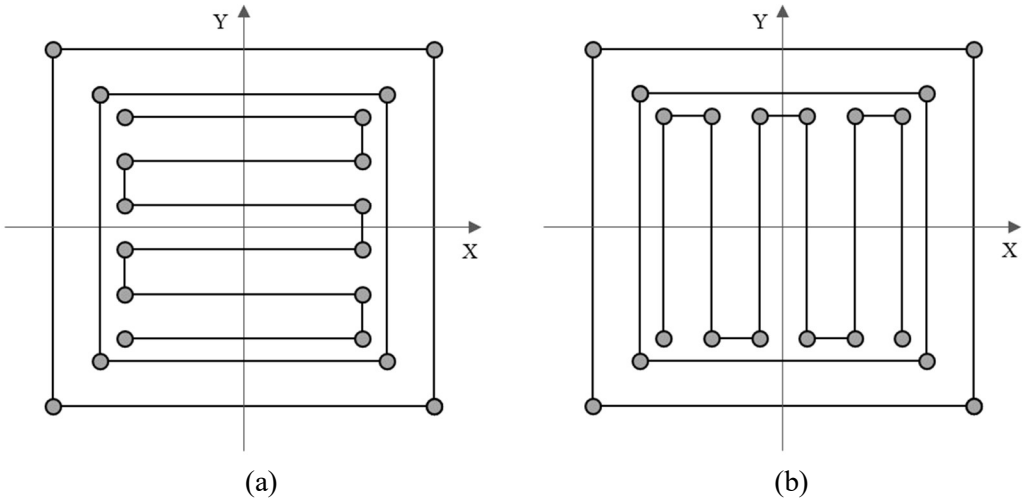

Figure 4.12 *– Visualization of the G-code. (a) odd layers, (b) even layers.*

The scheme of the grid obtained by superposition of two successive layers can be seen in figure 4.13.

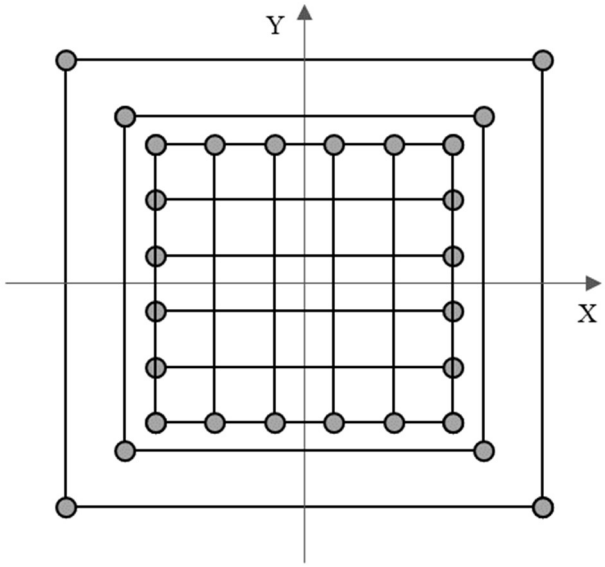

Figure 4.13 *– Visualization of two successive layers of the G-code.*

Three different nozzles have been used in the testing campaign and different sizes of the samples has been required, therefore, seen the scalability of the problem, it has been chosen to program the G-codes through Python.

The code, available in the Appendix A, has been written inside *JupiterLab* with *Python 3.7*; it could be needed to download the *math*, *mathplotlib.pyplot* and *numpy* libraries in order to run the code.

Once run, it is asked to give:

- the nozzle diameter in mm;
- the minimum square basis of the sample to be printed in mm;
- the inter-axis between the filaments in mm;
- the minimum height of the sample to be printed in mm;
- the inter layer distance expressed as ratio of the nozzle diameter, so from 0 to 1;
- the name to assign to the *.GCODE file that will be obtained as output of the procedure.

The code will first calculate the number of filaments that will be printed to cover the minimum square basis required, rounding up the ratio between the minimum square basis and the inter-axis between the filaments; the effective length is then calculated multiplying the number of filaments for the inter-axis of the side of the square. The number of layers is calculated rounding up the minimum height divided by the layer height (calculated multiplying the relative inter-layer distance by the nozzle diameter).

For each body structure to be printed (squares and serpentines), the X-, Y- and E-coordinates are derived, and each set of them would be written in GCODE language – that is with G1 command leading and with each value of the coordinate preceded by its letter. The Z-coordinate is the same for each layer, therefore it is expressed in the G-code only when it changes.

At the end of the calculations – that takes only a few seconds – the *.GCODE file is stored in the same folder in which the script has run.

5. A DOUBLE-POROSITY MODEL FOR 3D PRINTED FINE-GRAINED SOILS

The aim of this Chapter is to describe the building and the validation of a mathematical model in which the output characteristics of the printed samples (*n* or *e*) can be related to input parameters that can be controlled:

- before the 3D printing process – acting on the soil preparation;
- during the 3D printing process – acting on the G-code.

5.1 DOUBLE-POROSITY FRAMEWORK

As already explained, within the 3D printing process, the soil – prepared at an initial water content – undergoes an extrusion process and is then deposited in filaments adjacent one to another and then stacked in successive layers.

Therefore, before the 3D printing process, the soil can be studied as a porous media in which the pores can be filled with water or with air. In that case, according to the classical Geomechanical approach, the following definitions would apply:

- V_{TOT} – the total volume, divided into:
    - V_S – the volume of the soil skeleton;
    - V_V – the volume of the voids, in turn divided into:
        - V_L – the volume occupied by the liquid phase;
        - V_G – the volume occupied by the gas phase.

To summarize:

$$V_{TOT} = V_S + V_V \tag{1}$$

$$V_V = V_L + V_G \tag{2}$$

$$V_{TOT} = V_S + V_L + V_G \tag{3}$$

Considering an unit volume of the soil skeleton, the void index *e* can be defined as follow:

$$e = \frac{V_V}{V_S} \tag{4}$$

A representation of the porous medium is shown in figure 5.1.

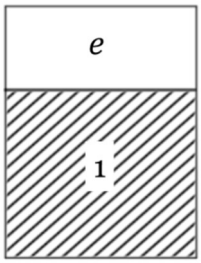

Figure 5.1 *– Schematization of a porous medium.*

A 3D printed soil, on the other hand, can be schematized as a double-porosity media, in which a porosity inherent to the filament, called *micro-porosity*, and a porosity dependent on the disposition of the filaments, called *macro-porosity*, can be defined (figure 5.2).

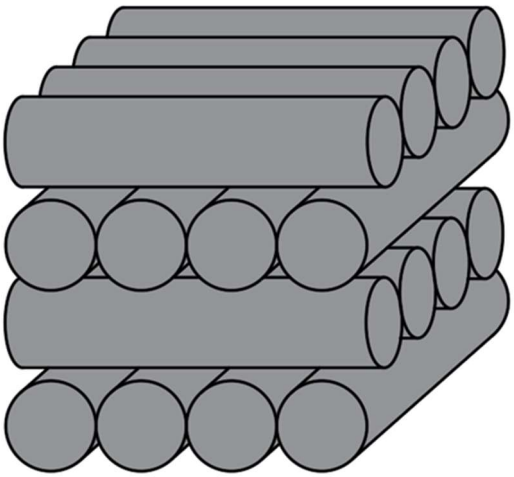

Figure 5.2 *– Axonometric schematization of a 3D printed soil.*

In this framework, the following definitions would apply:

- V_V^m – the volume of the voids relatives to the micro-porosity, divided into:
    - V_L^m – the volume of the voids relatives to the micro-porosity occupied by the liquid phase;
    - V_g^m – the volume of the voids relatives to the micro-porosity occupied by the gas phase.
- V_V^M – the volume of the voids relatives to the macro-porosity, divided into:
    - V_L^M – the volume of the voids relatives to the macro-porosity occupied by the liquid phase;
    - V_g^M – the volume of the voids relatives to the macro-porosity occupied by the gas phase.

The following relationships apply:

$$V_{TOT} = V_S + V_V^m + V_V^M \tag{5}$$

$$V_{TOT} = V_S + V_L^m + V_G^m + V_L^M + V_G^M \tag{6}$$

Considering an unit volume of the soil skeleton, two void indexes can be defined, one referred to the micro-porosity, so to the one inherent to the filament, the other referred to the macro-porosity, as follow:

$$e^m = e^f = \frac{V_V^m}{V_S} \tag{7}$$

$$e^M = \frac{V_V^M}{V_S} \tag{8}$$

The sum of these two void indexes would return the overall void index of the soil, as previously defined:

$$e^m + e^M = e \tag{9}$$

A representation of the double-porosity medium is shown in figure 5.3.

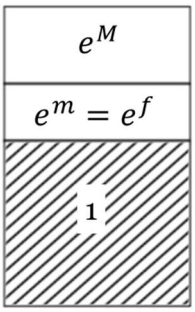

Figure 5.3 *– Schematization of a double-porosity medium.*

Considering an unit total volume, the following porosities can be defined:

- n^f – the porosity of the filament, thus referred to the volume of the filament
- n^m – the porosity of the micro-structure, thus referred to the total volume;
- n^M – the porosity of the macro-structure, referred too to the total volume.

To summarize:

$$n^f = \frac{V_V^m}{V^f} = \frac{V_V^m}{V_S + V_V^m} \tag{10}$$

$$n^m = \frac{V_V^m}{V_{TOT}} = \frac{V_V^m}{V_S + V_V^m + V_V^M} \tag{11}$$

$$n^M = \frac{V_V^M}{V_{TOT}} = \frac{V_V^M}{V_S + V_V^m + V_V^M} \tag{12}$$

The sum of the porosity of the micro-structure and of the porosity of the macro-structure would return the overall porosity of the soil:

$$n^m + n^M = n \tag{13}$$

With the hypothesis that:

- the degree of saturation of the filament is equal to 1;
- the macro-pores of the specimens at the moment of the 3D printing do not contain water;

some simplifications on the definitions above can be done:

$$V_V^m = V_L^m = V_L \tag{14}$$

$$V_V^M = V_G^M = V_G \tag{15}$$

$$V_{TOT} = V_S + V_L^m + V_G^M \tag{16}$$

$$V^f = V_S + V_L^m \tag{17}$$

The void index of the micro-structure (or of the filament) can therefore be expressed as:

$$e^m = e^f = \frac{V_L^m}{V_S} = wG_S \tag{18}$$

The porosity of the filament can therefore be calculated as:

$$n^f = \frac{e^m}{1 + e^m} \tag{19}$$

After some calculations, the porosity of the micro structure can be expressed as function of the porosity of the filament and of the porosity of the macro-structure (geometrical dependent):

$$n^m = n^f(1 - n^M) \tag{20}$$

The porosity and the void index of the sample can finally be calculated:

$$n = n^m + n^M = n^f(1 - n^M) + n^M \tag{21}$$

$$e = \frac{n}{1 - n} \tag{22}$$

To complete the model, it is necessary to derive the porosity of the macro structure.

Adjacent filaments

Circular filaments

To begin, a strong simplification would be carried out, considering cylindrical **filaments with circular cross section**.

With a single filament having diameter *d* and length *L*, as shown in figure 5.4a, the value of the macro-porosity corresponds to:

$$n^M = \frac{V_{parallelepiped} - V_f}{V_{parallelepiped}} = 1 - \frac{\pi}{4} \tag{23}$$

With the same approach, the value of the macro-porosity of multiple layers of adjacent filaments (figure 5.4b) is equal to:

$$n^M = \frac{V_{parallelepiped} - \sum V_f}{V_{parallelepiped}} = 1 - \frac{\pi}{4} \tag{24}$$

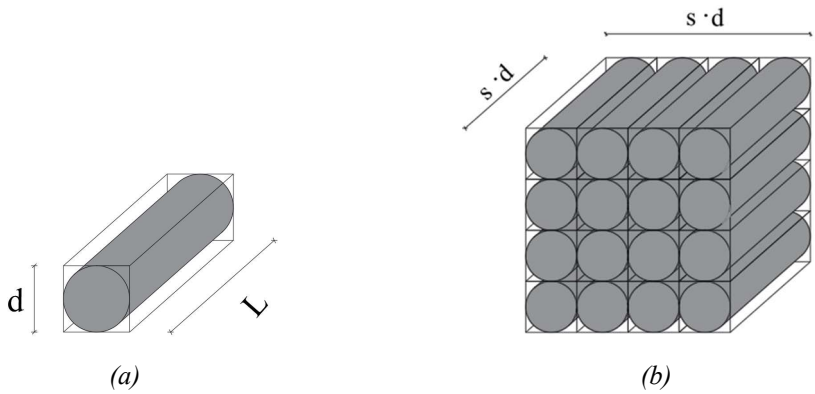

Figure 5.4 *– Macro-porosity of (a) a single circular filament and of (b) multiple layers of parallel circular filaments.*

In this latter case, however, the result is independent of the diameter of the cylindric base because the entire volume of each filament and of each parallelepiped are considered. When a specimen is derived from a printed sample, on the contrary, the integrity of the structure cannot be achieved. It is therefore interesting to evaluate the dimension of the Representative Elementary Volume (REV), that is the minimum observation volume to consider in order to have no variations on the observed property.

To do so, the schematization represented in figure 5.5 has been adopted to evaluate the expansion of the observed volume, having considered cylinder with unit height.

Beginning with the value of the macro-porosity of a single filament, widening the base of the square of observation, the area occupied by the filament can be computed and the macro-porosity corresponding to each step can be calculated.

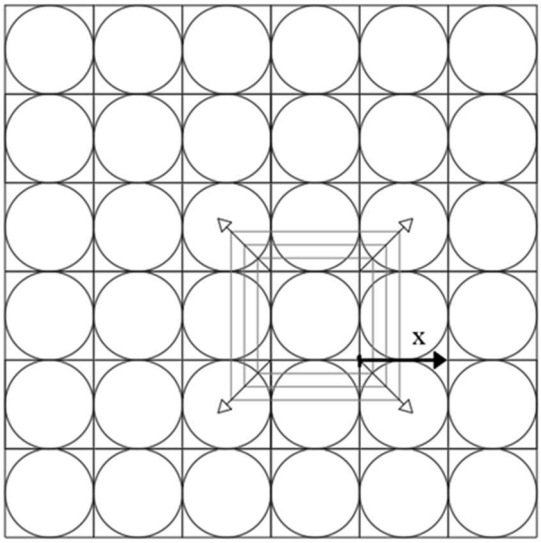

Figure 5.5 *– Schematization of the observed volume expansion.*

The obtained value of the macro-porosity depending on the ratio between the widening of the observation window and the diameter of the filament is represented in figure 5.6.

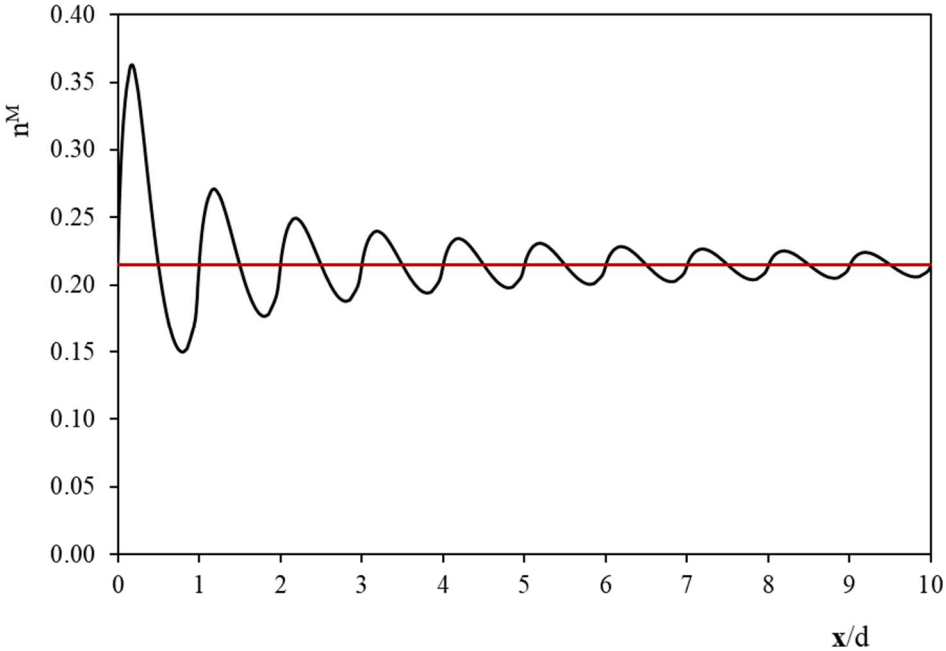

Figure 5.6 *– Macro-porosity depending on the widening of the observation window. Circular cross-section.*

It can be seen that after reaching an observation window x⁄d equal to 5, the value of macro-porosity varies in a range between 0.20 and 0.23, and, as x increases, it tends toward the value of ≈0.21 (=1-π/4) calculated earlier. The macro-porosity value of 0.21, as to be expected, is found whenever the observation window encompasses filaments in full, or when the observation window

dissects the outermost filaments in half. Macro-porosity increases when the observation window begins a new step and at the end of the latter; while it decreases in the middle part. This leads to the statement that if a parallelepiped with a square plan base is analysed, and the latter contains a number of filaments greater than ten, the error that is made on the macro-porosity if some filaments are sectioned is ±1.5%.

Elliptical filaments

In reality, an **ovalization of the cross section** of the filament occurs.

Considering an elliptical cross section for the filaments (figure 5.7), it occurs that in those cases too, considering a single filament or multiple layers of adjacent filaments, the value of the macro-porosity results equal to the same value:

$$n^M = 1 - \frac{\pi}{4} \tag{25}$$

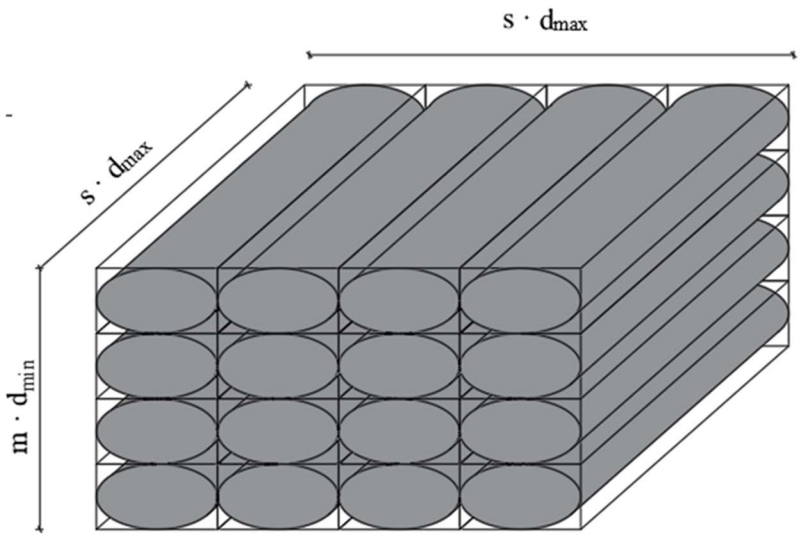

Figure 5.7 *– Multiple layers of parallel cylindrical filaments having elliptical cross section.*

The same considerations over the Representative Elementary Volume can be done in this configuration. To do so, the schematization represented in figure 5.8 has been adopted to evaluate the expansion of the observed volume, having considered cylinders with unit height.

Beginning with the value of the macro-porosity of a single filament, widening the window observation, the area occupied by the filament can be computed and the macro-porosity corresponding to each step can be calculated.

In this case it has been considered a window of observation whose sides have the same ratio of that of the ellipses' diameters.

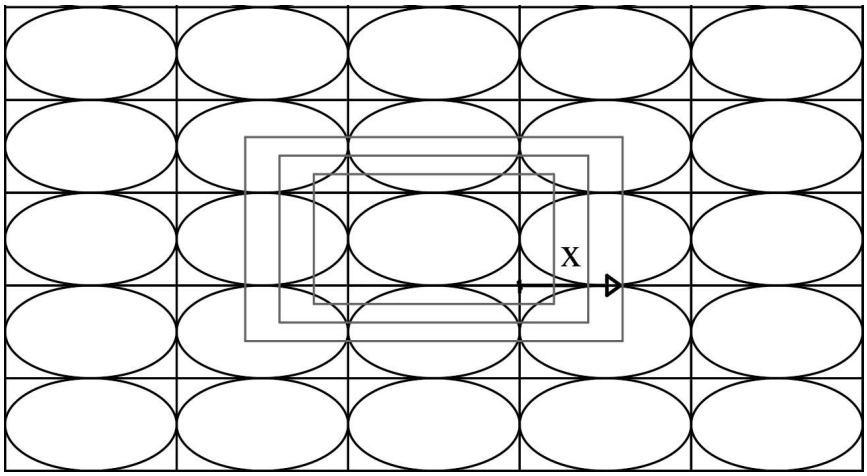

Figure 5.8 *– Schematization of the observed volume expansion.*

The computed values of macro-porosity depending on the ratio between the widening of the observation window and the maximum diameter of the filament with elliptical cross section are identical to the ones computed for the circular ones, as it is shown in figure 5.9.

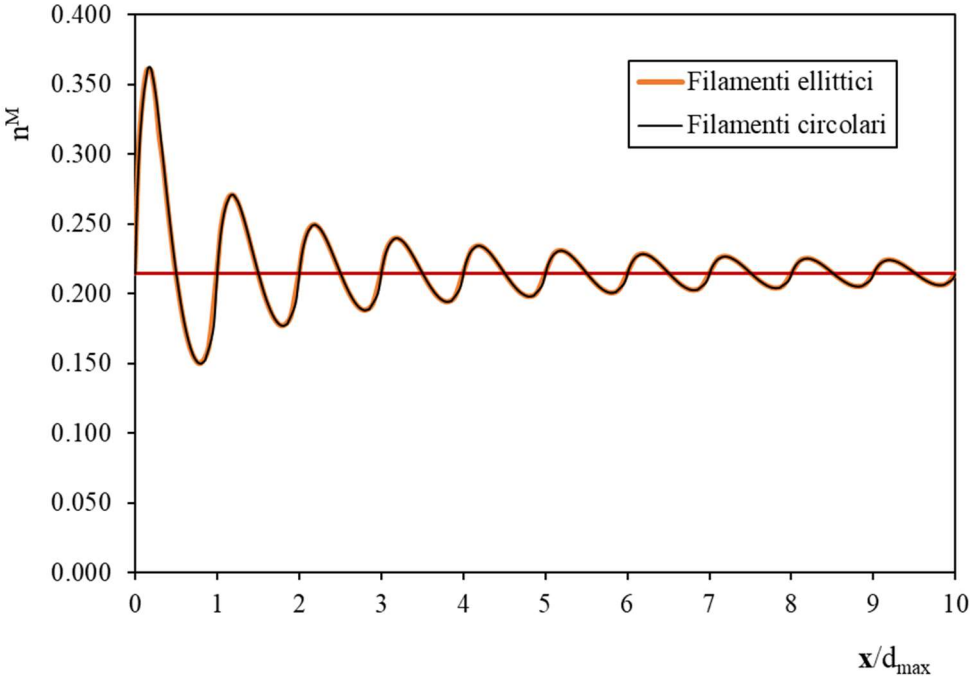

Figure 5.9 *– Macro-porosity depending on the widening of the observation window. Comparison between circular and elliptical cross section of the filament.*

Finally, it can be stated that the ovalization of the filaments from the point of view of macro-porosity, in the model presented so far, has no relevant effect.

Distanced filaments

It's only when a distance X from a filament to the adjacent one occurs (figure 5.10), that the value of the porosity of the macro-structure shows a dependence on the diameters of the ellipse and on the distance amongst parallel filaments.

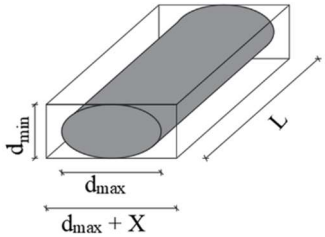

Figure 5.10 *– Macro-porosity of (a) a single elliptical filament and of (b) multiple layers of parallel elliptical filaments.*

While the 3D printing process happens in undrained conditions, the area of the cross section of the filament must remain the same even if ovalized; therefore it is possible to express the values of the maximum and minimum diameter of the ellipse as function of the diameter of the nozzle:

$$d_{max} = \alpha\, d \tag{26}$$

$$d_{min} = \frac{1}{\alpha}\, d \tag{27}$$

When considering the single-filament case, the porosity of the macro-structure is expressed as follow, depending on the ratio between the maximum diameter of the ellipse and on the spacing considered:

$$n^M = \frac{V_{parallelepiped} - V_f}{V_{parallelepiped}} = 1 - \frac{\frac{\pi}{4}}{1 + \frac{X}{d_{max}}} \tag{28}$$

The trend of the macro-porosity with increasing spacing X with respect to the maximum diameter, as is the adimensional spacing, is shown in figure 5.11.

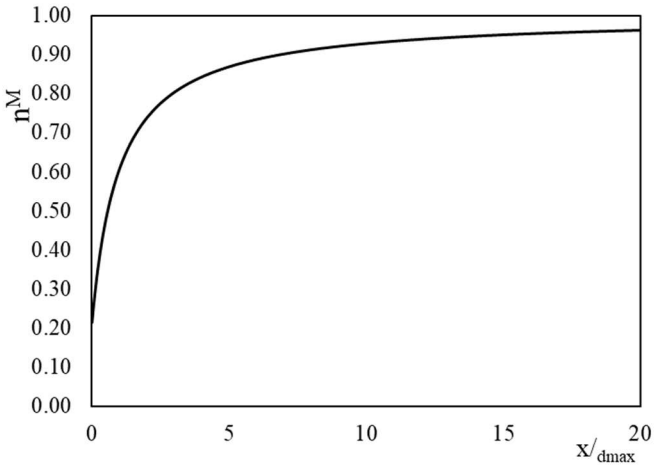

Figure 5.11 *– Macro-porosity depending on the adimensional spacing for a single filament.*

As it is possible to notice, the macro-porosity is equal to ≈0.21 when the spacing is equal to 0, while increasing the spacing the macro-porosity tends asymptotically to the unit value. The range within which it is reasonable to study the problem results between spacing values between 0 and d_{max} (figure 5.12), in which the macro-porosity assumes widely variable values, from 0.21 up to the value of 0.61.

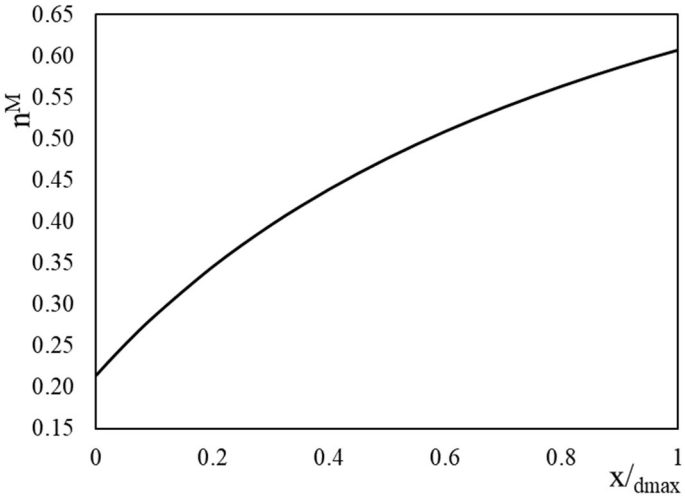

Figure 5.12 *– Macro-porosity depending on the adimensional spacing for a single filament. Adimensional spacing in the range 0-1.*

The study has been therefore extended to the case of the parallelepiped formed by *s* parallel filaments distanced by X (figure 5.13).

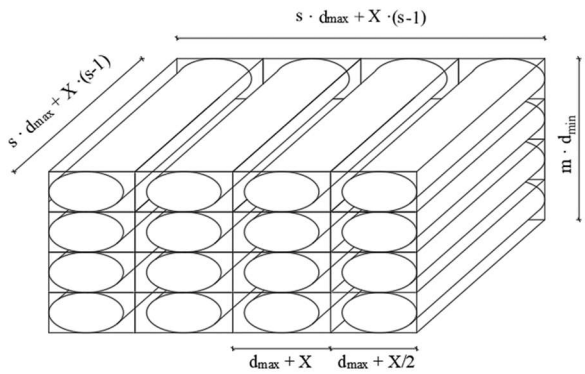

Figure 5.13 *– m layers of s parallel cylindrical filaments having elliptical cross-section distanced by X.*

When considering the double-structure having *m* layers of *s* adjacent filaments with spacing equal to X, the porosity expression becomes:

$$n^M = \frac{V_{parallelepiped} - \sum V_f}{V_{parallelepiped}} = 1 - \frac{\frac{\pi}{4}}{1 + \frac{X}{d_{max}} \frac{(s-1)}{s}} \tag{29}$$

In this case too, the dependence on the ratio between the distance and the maximum diameter of the ellipse appears; a dependence on the number of filaments considered *s* is added.

The results of this macro-porosity analysis are diagrammed in figure 5.14 as a function of spacing in dimensionless terms (X/d_{max}) and as the number of filaments considered *s* varies.

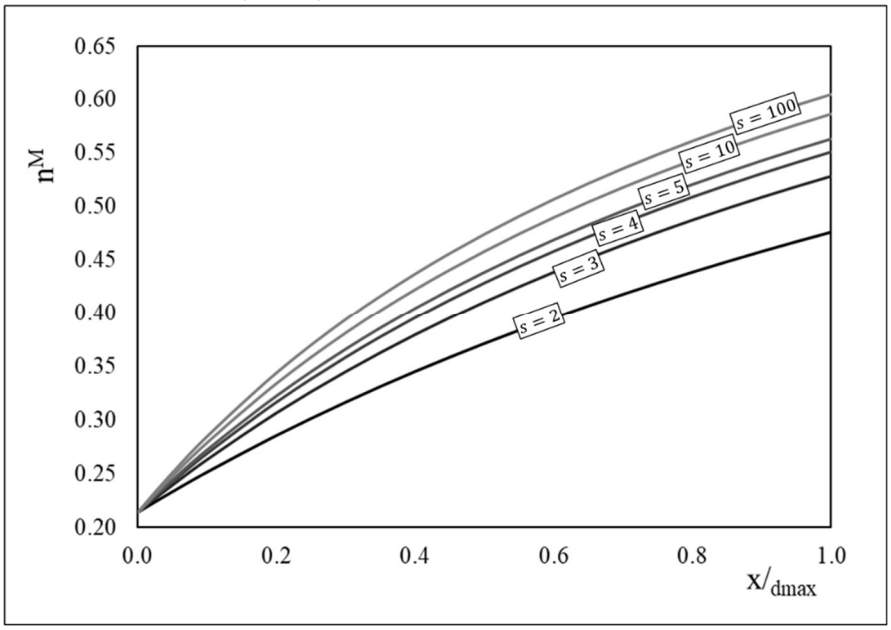

Figure 5.14 *– Macro-porosity depending on the adimensional spacing for a single filament. Adimensional spacing in the range 0-1. Variable number of filaments s.*

It is noticeable the same trend encountered when analyzing the circular cross section, with an increase on the macro-porosity with increasing spacing; moreover, the macro-porosity increases too with increasing number of filaments *s*. In addition, macro-porosity, given the same spacing between filaments, initially increases rapidly as the number of filaments considered increases (see from s=2 to s=3), slowing down once a certain number of filaments is exceeded (see from s=10 to s=100). It can therefore be said, that, with the same spacing, considering a number of filaments greater than ten does not lead to significant differences in terms of macro-porosity, confirming what was already seen during the REV study, where a parallelepiped with a squared base containing at least ten filaments was set as the minimum volume of observation.

It is also relevant to notice that the height of the parallelepiped does not appear to affect the evaluation of the macro-porosity in the considered model.

5.2 INDEX PROPERTIES PREDICTION

By means of the model just presented, it is possible to predict the index properties of the 3D printed samples through the following layout:

Input parameters:
Dependent on the soil:

- water content of the fine-grained soil to be printed w;
- degree of saturation of the soil to be printed S_r;
- specific gravity of the soil to be printed G_s;
- expected ovalization ratio of the filament diameter α

Dependent on the G-Code:

- diameter of the nozzle to be used for 3D printing d;
- barycentric inter-axis amongst parallel filaments i.

Predictable output parameters:

- porosity of the filament n^f;
- maximum diameter of the elliptical cross section of the filament d_{max};
- spacing amongst parallel filaments X;
- number of parallel filaments s:
- macro-porosity of the sample n^M;
- porosity and void index of the sample n and e.

5.3 VALIDATION OF THE MODEL

In order to validate the model presented above, five tests have been carried out. In particular, five samples with different spacing amongst parallel filaments have been 3D printed. To reduce the variables to be taken into account, all of the samples have been 3D printed using the same nozzle; the same soil with a fixed input water content has been used for all the tests, while the barycentric inter-axis amongst parallel filaments changed. The ovalization ratio of the filament has been evaluated through image-analysis of the microphotograph of the samples conducted with a Scanning Electron Microscope (SEM), as described on the next Chapter 6.

To prepare the specimens, first, the G-codes for each sample have been prepared using the python script described in the previous Chapter 4 and presented on Annex A. To obtain them it is necessary to set the diameter of the nozzle, the minimum length of the square basis L_s, the barycentric inter-axis between parallel filaments i, the minimum height of the parallelepipedal sample h, the interlayer distance ratio h and the printing speed v_{prt}.

Knowing the desired spacing amongst parallel filaments X, and the ovalization ratio α, the parameters collected in table 5.1 have been set.

Table 5.1 *– Input parameters.*

dependent on the soil				dependent on the geometry	
S_r	G_s	w	α	d_n	i
[-]	*[-]*	*[-]*	*[-]*	*[mm]*	*[mm]*
1	2.77	0.31	1.14	1.41	0-1

The printing velocity has been set always the same for all the 3D printing, equal to 800 mm/min.

A verification of the extrusion process has been conducted – according to the criterion (Wroth and Houlsby, 1984) described in the previous Chapter 3 – on the 3D printing having the longest duration, as is the one in which the spacing amongst parallel filaments is equal to zero.

In that case, being the extrusion process of the 3D printing conducted with a pressure applied on the ram of the tank equal to 700 kPa, it has been considered the consolidation coefficient c_v of the Commercial Clay correspondent to the loading step n. 6 of the oedometric test executed on that soil – whose results will be shown in the next Chapter 7 – corresponding to an applied effective pressure of 591 kPa, resulting equal to 1.98 mm^2/s. The characteristic time (Terzaghi, 196_) has been determined Considering a partial filling of the tank equal to 300 mm. It has been then confronted with the extrusion time expected to print a total length of the filament estimated equal to 16,000 mm with the fixed printing velocity of 800 mm/min.

The criterion is met as follows:

$$\frac{t_{3Dp}}{H^2/c_v} = 0.026 < 0.1$$

Once the samples have been printed, the specimens have been derived cutting them with a nylon thread, assuring that no filaments would be rescinded along the longitudinal section. Pictures of the specimen are reported in figure 5.15.

(a)

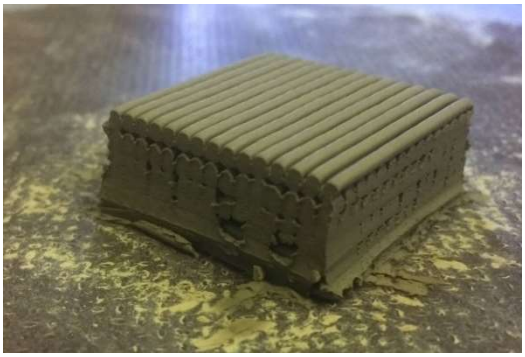

(b)

(c)

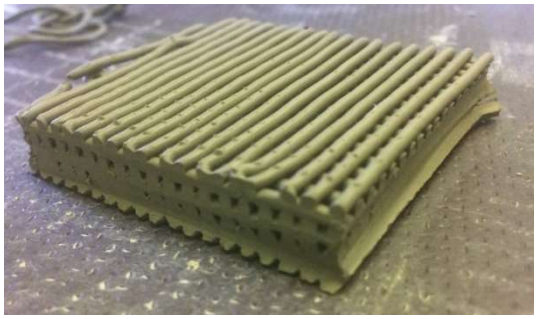

(d)

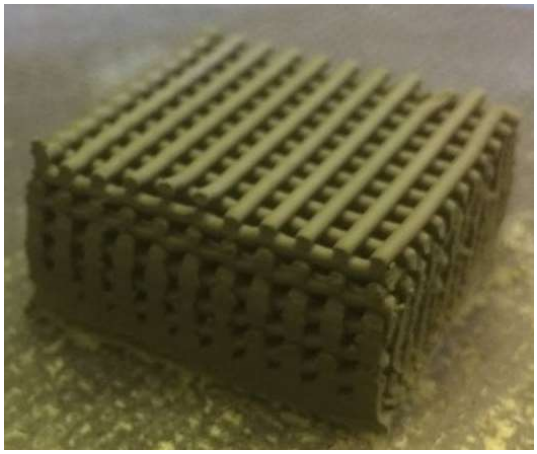

(e)

Figure 5.15 *– Specimens derived from 3D printed samples tested for the validation of the model. X/dmax = 0 (a); 0.25 (b); 0.5 (c); 0.63 (d); 1 (e).*

Index properties of the specimens

To validate the model, the values of the index properties of the 3D printed specimens predicted with it are compared with the experimental determined values.

Index properties of the filament

The void index and the porosity of the filament, respectively e^f or e^m and n^f can be evaluated with the following relations:

$$e^m = \frac{wG_S}{S_r}$$

$$n^f = \frac{1}{1 + e^m}$$

Under the hypothesis of saturated filament, the parameters can be determined.

To confirm the hypothesis of saturation of the filament, and to experimentally determine the values of the porosity and of the void index of the filaments, two set of tests have been conducted:

- suction of the 3D printed filament has been determined several times during the various printings conducted during the thesis work by means of a WP4 (Water Dewpoint Potentiometer). Immediately before 3D printing, the machine would almost always registered null values of that;
- total volume of 3D printed filament has been determined according to the method B of the "American Standard Test Methods for Density and Specific Gravity by Displacement" (ASTM D792-2020), using kerdane as apolar liquid for the measurements.

Table 5.2 reports the comparison between the predicted values of the index properties of the specimens and the experimentally determined ones.

Table 5.2 – *Comparison between predicted and determined index properties of the filament.*

predicted		determined	
$e^m=e^f$	n^f	$e^m=e^f$	n^f
[-]	*[-]*	*[-]*	*[-]*
0.86	0.46	0.77	0.44

Index properties of the macro-structure

Knowing the geometrical characteristics of the 3D printed specimens, the macro-porosity can be calculated accordingly to the relation (29).

Considering the previously predicted porosity of the filament, the porosity of the specimens and their void ratio would be calculated accordingly to the relations (21) and (22).

Measuring the volume of the specimens by means of a calibre with 0.01 mm of resolution and determining the volume of the soil skeleton, the values of the index properties of the specimens can be experimentally determined.

Table 5.3 and figure 5.16, compare the predicted values of the index properties of the specimens and the experimentally determined ones.

Table 5.3 *– Comparison between predicted and determined index properties of the specimens.*

	predicted			*determined*	
X/d_{max} [-]	n^M [-]	n [-]	e [-]	n [-]	e [-]
0.00	0.21	0.56	1.26	0.56	1.27
0.25	0.36	0.66	1.94	0.60	1.50
0.50	0.46	0.71	2.45	0.65	1.86
0.63	0.51	0.74	2.85	0.69	2.23
1.00	0.59	0.78	3.55	0.71	2.45

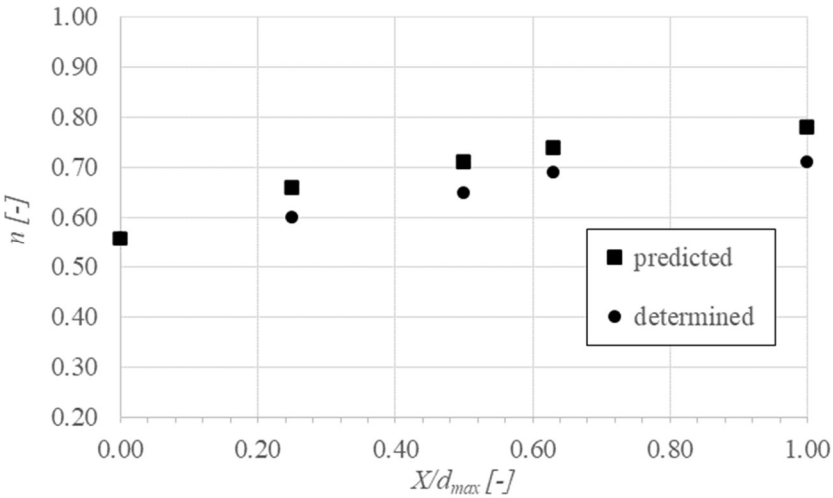

Figure 5.16 *– Predicted and determined values of the porosity of the tested specimens.*

The model appears to be able to predict well the index properties of the 3D printed specimens when the distance between parallel filaments tends to be equal to 0.

When dimensionless spacing increases, the model overestimates the porosity of about 7%. This difference can be explained with the absence in the model of the constitutive law of the soil, implicitly considering that as a perfectly rigid material. In the presence of increasingly high spacing, indeed, the filaments lying on the upper layer tend to sag within the spacing of the layer below as shown in figure 5.17. Moreover, the increasing spacing leads to a reduction of the confinement of each filament and consequently to a lateral expansion of the filaments located in the lower layers (figure 5.18).

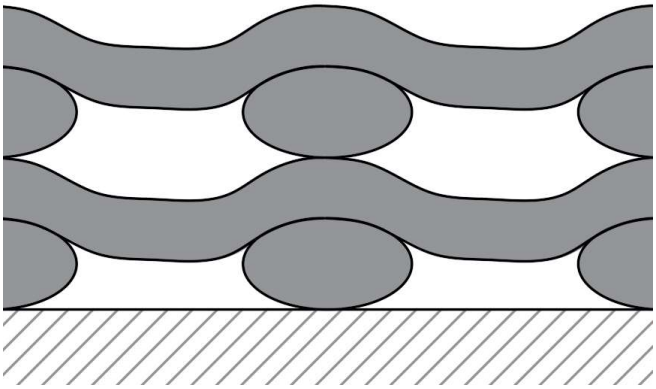

Figure 5.17 *– Sagging of the filaments within the spacing of the layers below.*

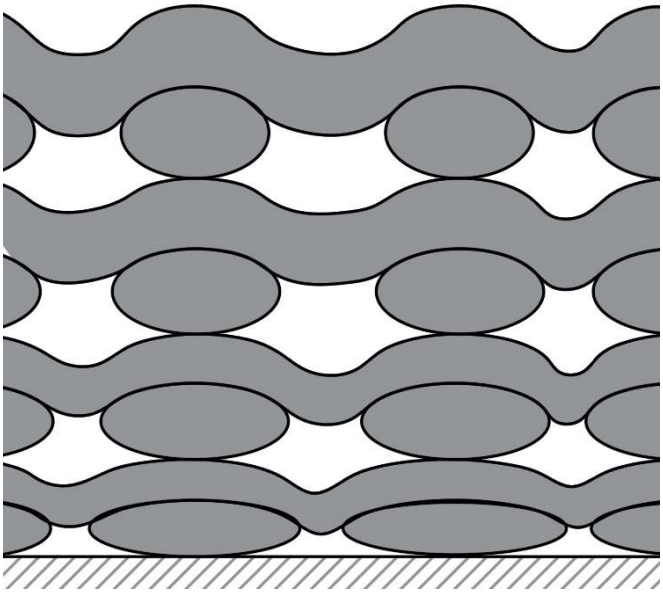

Figure 5.18 *– Lateral expansion of the filaments.*

5.4 SUMMARY

A double-porosity model has been proposed to predict the index properties of 3D printed specimens dependent on geotechnical characteristics of the fine grained soil used for the realization of the specimens and on their geometry, i.e. the spacing amongst parallel filaments.

In the latter part of the Chapter, the model was applied to 5 specimens characterized by different value of the adimensional spacing amongst parallel filaments. Results showed that the model tends to overestimate the porosity characteristics of the specimens. Adding the deformability characteristics of the soil in the model may help to improve the fitting capability of the model itself. Further studies are recommended to verify this assumption.

6. MICROSTRUCTURAL CHARACTERIZATION OF A 3D PRINTED SOIL

This Chapter has been published by the scientific journal "*Soils and Rocks*":

Ferrari, A., Rosone, M., La Rosa, S., & Sapienza, G. (2022). Microstructural characterization of a 3D-printed soil. Soils and Rocks, 45.
https://doi.org/10.28927/SR.2022.005422

Contribution of the doctoral candidate: Investigation, Data Analysis, Writing.

Additional images and data analysis not appearing in the paper are provided at the end of the Chapter.

Transversal applications of 3D printing (or Additive Manufacturing) have been recently implemented in the field of Geomechanics. In a 3D printing process, the printed volume is obtained from successive layering of adjacent soil filaments. In this work, the fabric of an as-printed soil has been carried out by combining Mercury Intrusion Porosimetry (MIP) tests and Scanning Electron Microscope (SEM) observations, with the aim to highlight how the particle arrangements and the orientation and shape of pores are linked to the printing operation. The microstructural analyses showed that macropores are the result of the relative position of the filaments and their initial distortion in quasi-undrained conditions. Particle arrangement within the soil filament is strongly anisotropic, due to the rotative movement of the soil in the extruder.

6.1 INTRODUCTION

The fields of application of 3D-printing (or Additive Manufacturing) are constantly growing, including uses in Geomechanics. 3D-printing of polymeric materials has been used to manufacture synthetic porous samples aiming at mimicking characteristics of soils and rocks (Ju et al., 2014; Dal Ferro & Morari, 2015; Bourke et al, 2016; Gomez at al., 2019). On the other hand, soils have been also used as printing materials, for artistic scopes, for the preparation of samples for laboratory testing (Hanaor et al., 2015; Matsumura & Mizutani, 2015; Mansoori et al., 2018; Pua et al., 2018; Pua et al., 2021), or even for the construction of structures and infrastructures (Khoshnevis, 2004; Perrot et al., 2018b).

In a printing process, the soil exits from the printer as filaments along prescribed paths; the result is a volume consisting of successive layers of adjacent soil filaments. The fabric of the printed soil is then the result of the initial microstructural characteristics of the filament, of the relative position of the adjacent filaments, and of all possible hydro-mechanical loads happening in the process (e.g increase of total stress as the layers overlap, or variations in water content due to exposure to hygroscopic conditions).

There is strong evidence on the fundamental role of the fabric of clayey soils on their hydro-mechanical response (e.g. Romero & Simms, 2008; Munoz-Castelblanco et al., 2012; Cordão Neto et al., 2018; Ferrari et al., 2022). This link seems highly relevant for a 3D-printed soil, in which the fabric can be seen as a controlled result of the printing process. In this regard, this note presents the results of a microstructural investigation carried out on 3D-printed soil samples prepared with a commercial 3D-printer, specifically adapted to be used with a fine soil. The different microstructural peculiarities of the as-printed samples are identified and discussed thanks to the combined use of Scanning Electron Microscope (*SEM*) and Mercury Intrusion Porosimetry (*MIP*).

6.2 MATERIAL AND METHODS

A commercial clayey soil used for artistic purposes was used as printing material; the geotechnical characteristics are listed in Table 6.1. Starting from the as-received condition, the soil was accurately mixed with distilled water to reach a consistency index *CI* close to 0.5 (corresponding target water content $w = 0.32$), which ensured adequate workability and limited the occlusion of air bubbles in the soil during the printing process.

Table 6.1 *– Main geotechnical properties of the soil called "CC" (specific gravity G_s, liquid limit LL, plastic limit PL, clay fraction f_{clay}, silt fraction f_{silt}, sand fraction f_{sand}).*

Soil ID	G_s	*LL*	*PL*	f_{clay}	f_{silt}	f_{sand}
(-)	(-)	(-)	(-)	(%)	(%)	(%)
CC	2.77	0.45	0.21	52	46	2

A Delta WASP 2040 Clay 3D printer has been used to prepare the samples. The printing system (figure 6.1) includes a 3-liter air-tight tank, in which an air-pressurized ram moves the soil toward the extruder; this latter holds an endless screw connected to a stepper motor. The rotation of the screw forces the extrusion of the soil filament through the nozzle. In this work a nozzle with a diameter of d_n = 1.4 mm was used. The air pressure in the tank was set to 600 kPa and maintained constant during the whole printing process. The printing velocity has been set equal to 180 mm/min.

The printer was programmed to print samples with a base of 75 mm x 75 mm and a height of 25 mm, obtained by the superposition of horizontal layers. As shown in figure 6.2, each layer was confined with two parallel filaments printed along the perimeter, while the internal part was filled with adjacent filaments extruded along the same direction; in each subsequent layer, the extruding direction was changed by 90 degrees.

Three samples were prepared to assess the repeatability of the printing procedure in terms of final sample characteristics (water content and void ratio). Cubical specimens of around 1 cm3 were cut from the central part of two printed samples and used for the microstructural investigation.

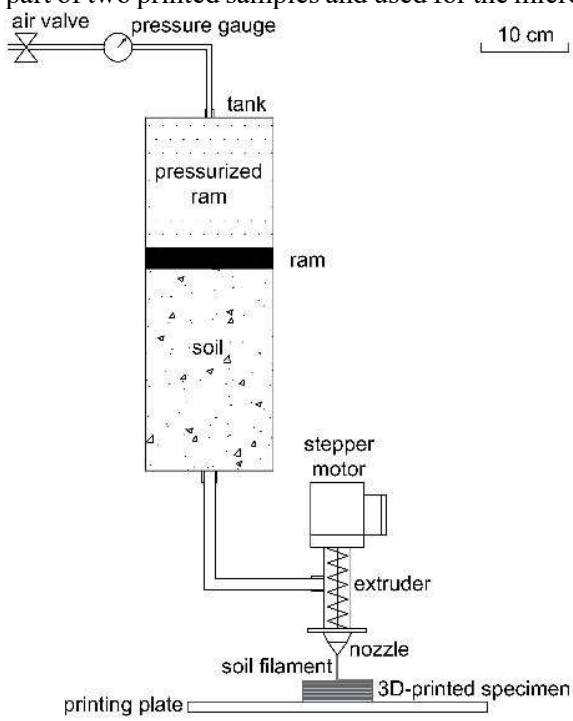

Figure 6.1 *– Schematic layout of the 3D soil printer.*

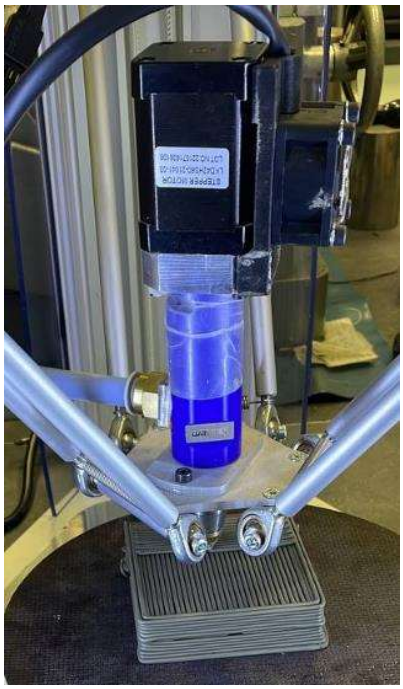

Figure 6.2 *– Picture of a sample being printed.*

Scanning Electron Microscope (*SEM*) observations and Mercury Intrusion Porosimetry (*MIP*) tests were carried out on the printed specimens after they were freeze-dried. This operation was done by submerging the specimens in liquid nitrogen (thus creating amorphous ice and avoiding the water volume to increase due to crystallization) and by subsequent sublimation in quasi-vacuum (P = 0.06 mbar) and under low temperature (T = -52°C).

A *Quanta-200-FEG SEM* was used for the observations in high-vacuum mode on golden-coated specimens. MIP tests were performed using a porosimeter (*Pascal 140–440 series, Thermo Scientific*) attaining a maximum intrusion pressure of 400 MPa, corresponding to an entrance pore diameter of about 4 nm. An extrusion stage was also performed after the mercury intrusion.

6.3 FABRIC OF THE PRINTED SAMPLES

Water contents of the printed samples were found in a narrow range with an average value of 0.30, slightly lower than the preparation water content, as a probable consequence of a partial consolidation induced by the stress applied through the row, and some drying due to the exposure to atmosphere (measured total suction of as-printed samples was about 0.3 MPa). In spite of some variability in as-printed void ratio ($e = 1.07 \pm 0.07$), the applied 3D-printing procedure was considered adequate to produce samples with similar characteristics. The average degree of saturation was 0.73.

To observe the fabric of the 3D-printed samples, the external surface (top and lateral) and the vertical cross-section of the extracted specimens were observed at *SEM* (figure 6.3).

The top surface of the specimen and its cross section are framed at 60X of magnification in Figure 6.3a and 6.3b, respectively. In particular, Figure 6.3a shows a zone of the top surface, where an inversion of the printing direction occurred. At this magnification, the soil filaments appear homogeneous. Figure 6.3b shows the result of the superposition of the filaments: a certain

ovalization in the cross-section of the filament can be detected, as a probable result of the weight of the above layers.

Interestingly, the area of the cross section of the filament coincides with the area of the circle having the diameter of the nozzle (d_n = 1.4 mm), suggesting that the deposition of the filament occurs in undrained conditions, without volume change. As a consequence of this ovalization, a good contact is observed when two filaments overlap, while an inflection is produced in the void space among adjacent filaments. Voids between the soil filaments have an average equivalent diameter of 150 mm and they represent the macropores (inter-filament pores) of the 3D-printed soil.

At 300X, the external surface of the filament (Figure 6.3c) shows a smooth and compact particle arrangement, with iso-oriented clay particles and few pores 0.3÷1.5 mm wide and 3÷30 mm long. On the microphotograph of the cross-section of the filament at 300X (Figure 6.3d), a spiral trend of the particles orientation can be observed, as a result of the rotative movement of the screw in the extruder. Pores having a maximum diameter of about 30 mm as well as pores 1-2 mm wide and 10÷70 mm long can be identified at the contacts between the clay aggregates (Figure 6.3d).

In the last microphotographs, taken with a 4000X magnification, different arrangements of the clayey particles are visible. Particles on the lateral surface (figure 6.3e) are iso-oriented and arranged with face-to-face packing; the arrangement of the particles in the inner part of the filament (figure 6.3f) is more complex showing aggregated structures with both face-to-face and edge-to-face contacts. At this magnification, inter-aggregate pores, having a dimension of few microns, and intra-aggregates pores of smaller dimensions (lower than 0.5 mm) are visible. It is worth to observe that where the clayey particles are packed with face-to-face contacts the intra-aggregates pores are smaller.

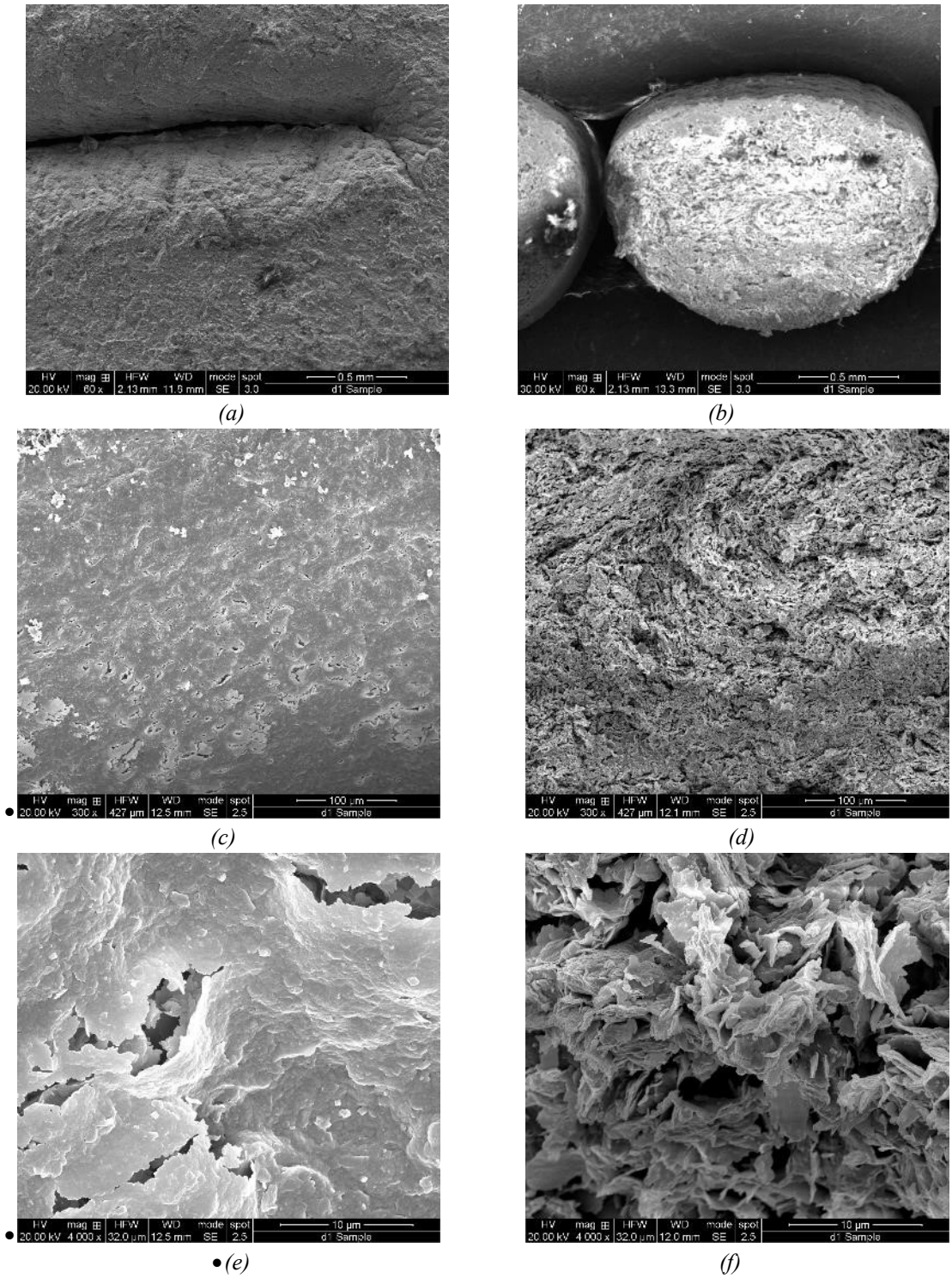

Figure 6.3 *– SEM photomicrographs of the 3D-printed soil: external surface (top in a, lateral in c and e) and vertical cross section (b, d and f). Magnifications are 60X (a,b), 300X (c,d) and 4000X (e,f).*

The results of MIP tests performed on two different specimens are reported in Figure 6.4a in terms of the intruded/extruded void ratio *(e_i,* the ratio of the void volume intruded by mercury

($V_{v,i}$) to the volume of soil particles (V_s)) and in Figure 3b in terms of the Pore Side Density *PSD* ($PSD = -De_i/D(logd)$) as a function of the computed pore diameter d. The total void ratios intruded during the MIP tests ($e_i = 0.838$ and 0.898) were lower than the mean void ratio measured on the 3D-printed samples ($e = 1.07$).

This difference is believed to be the result of the pores larger than 120 mm which are filled with mercury before the injection starts, and which are not detected with the technique. This maximum detectable pore diameter well corresponds to the average diameter of the inter-filament pores (150 mm). The intruded void ratio is then attributed to the pores within the filaments only. The corresponding microstructural void ratio e^m defined in the first part of this Chapter is then quantified in the range of $e^m = 0.838 \div 0.898$. The lower bound of macropores, which corresponds to the gaps left by the printing process between the filament, is set to 120 mm (figure 6.4).

On the other hand, the analytical evaluation for the macro-structural void ratio carried out in the first part of this Chapter allows to compute a value $e^M = 0.274$. The sum of the microstructural and macrostructural void ratios is in good agreement with the average void ratio of the 3D printed samples (Figure 6.4a, right axis).

The main modal diameter of pores ($d = 1$ μm, Figure 6.4b) corresponds both to the pores observed along the external surface of soil filament and to the pores between clayey aggregates observed in the cross-section. According to the procedure proposed by Delage & Lefebvre (1984) intra-assemblage porosity results in a reversible behaviour during the intrusion/extrusion phases, while mercury is trapped by capillary effects in the bigger pores once the applied pressure is removed (Figure 6.4a). This criterion applied to the two tests performed could provide the upper bound value of the intra-assemblage as $d = 0.127$ μm. These micropores include the porosity between clayey particles stacked in face-to-face disposition. However, the criterion based on intrusion and extrusion curves could underestimate the limit value (Yuan et al., 2020). In fact, a secondary peak of *PSD* can be identified in the same range of micropores ($d = 0.18$ μm). This class of micropores corresponds to the intra-assemblage pores located between particles stacked in face-to-edge disposition (Figure 6.3f). Then, on the base of *PSD* evolution (Figure 6.4b) a more consistent upper limit for the intra-assemblage pores domain can be identified at $d = 0.3$ μm.

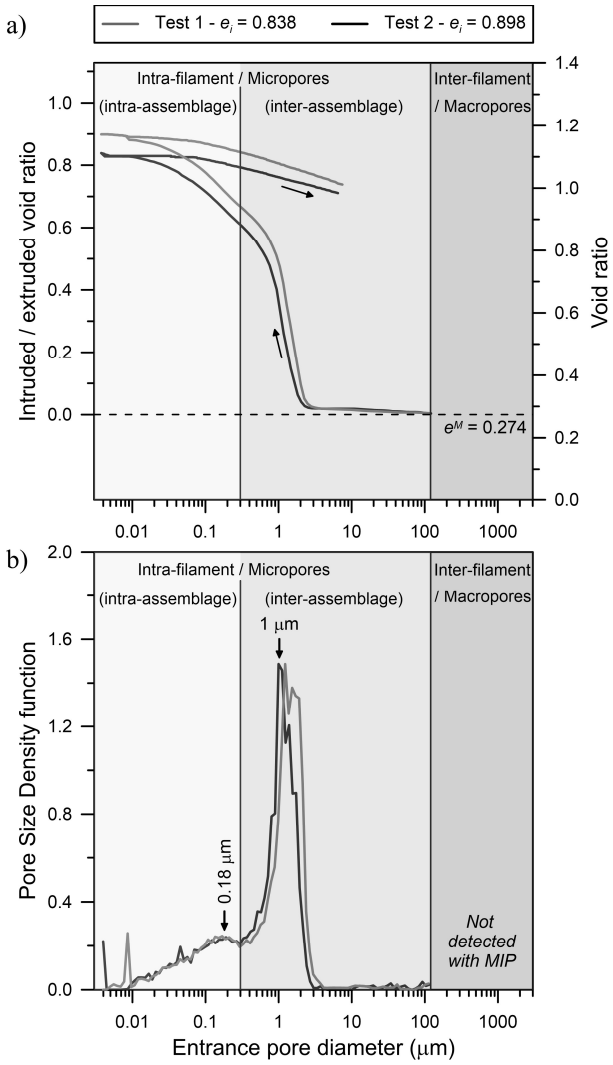

Figure 6.4 *– (a) Void ratio and (b) Pore Size Density as a function of the Entrance Pore Diameter from MIP tests.*

6.4 CONCLUSION

The fabric of a 3D printed clayey soil has been explored, highlighting how the particle arrangements and size, orientation and shape of pores are strongly linked to the printing operation. In particular, it was observed that the macropores are the result of the relative position of the filaments and their initial distortion in quasi-undrained conditions. Particle arrangement within the soil filament is strongly anisotropic due to the rotative movement of the soil in the extruder. Moreover, intra-assemblage pores, located in between the clayey assemblages, and intra-assemblage pores, as the results of different particle contacts (both face-to-face and edge-to-face contacts), characterize the microporosity in the intra-filament soil structure.

It is believed that these observations could pose the basis for engineering the creation of fabric-controlled samples; this capability could serve multiple purposes, such as the production of

samples with precise hydro-mechanical characteristics, e.g. permeability and water retention properties.

6.5 ADDITIONAL IMAGES AND DATA ANALYSIS

In this section additional images then those presented in the paper are reported.

Figure 6.5 shows the cross section of the specimen observed with the SEM after freeze-drying. Four layers have been printed each of them constituted of a serpentine having nine arms and of two squared rings confining the serpentine. The ovalization of the cross section of the filament is visible and more pronounced on the lowest layer.

Figure 6.5 *– SEM photomicrograph of the 3D-printed soil. Cross section of the filament. Magnification 100 x.*

Figure 6.6 shows the cross section of the specimen observed with the *SEM* with a magnification of 100x. In the superior part of the micrograph it is possible to notice the sagging of the upper filament upon the ones of the layer above, with the consequent reduction of the macro-porosity.

In Figure 6.7 is shown the top view of the specimen where the 3D printer direction changes at the end of an arm of a serpentine. Three insights can be gained from the analysis of this picture:

- in proximity of the change in direction of the filament, there is an accumulation of the soil due to the movement of the 3D printer that results in a reduction of the barycentric distance amongst the connected arms – this observation confirms the goodness of the choice to print samples bigger than the desired dimension of the specimen to avoid the extremal parts in which this accumulation occurs;
- the lateral surface of the filament presents concentric lines whose nature can be explained with an incorrect setting of the height of the layer, set too low on the G-code. In this case, a higher quantity of soil is deposited on each position; the "extra" soil would therefore push back the soil already deposited generating the observable lines;

the incorrect setting of the height of the layer is also confirmed by the observation of the horizontality of the top surface of the filament, due to the contact between the nozzle and the filament already printed.

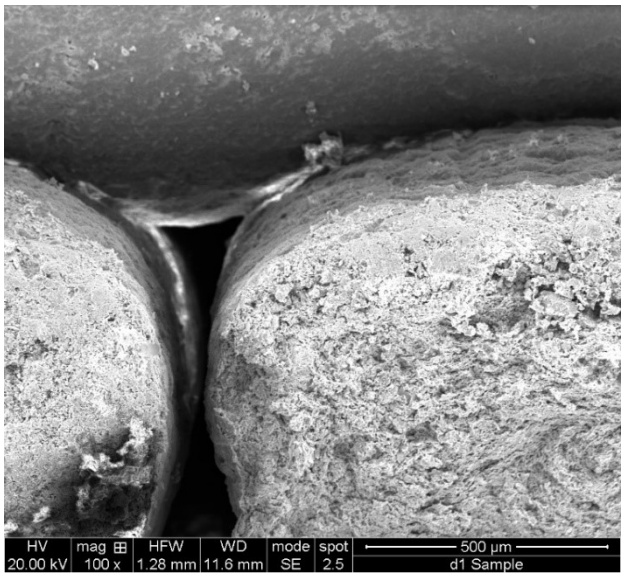

Figure 6.6 *– SEM photomicrograph of the 3D-printed soil. Cross section of the specimen. Magnification 100x.*

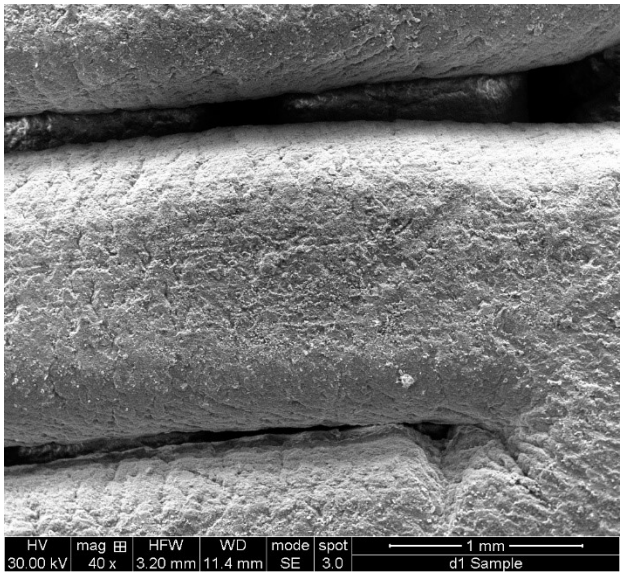

Figure 6.7 *– SEM photomicrographs of the 3D-printed soil. Top view of the filament. Magnification 40x.*

The last observation is confirmed by the SEM micrograph obtained with a magnification of 300x of figure 6.8. Comparing the fabric of the top surface of the filament with the one of the lateral one of figure 6.3c, the smoothness that characterizes the lateral surface, due to the iso-orientation of the clay particles is not observable here, due to the disturb caused by the contact of the moving nozzle with the 3D printed soil.

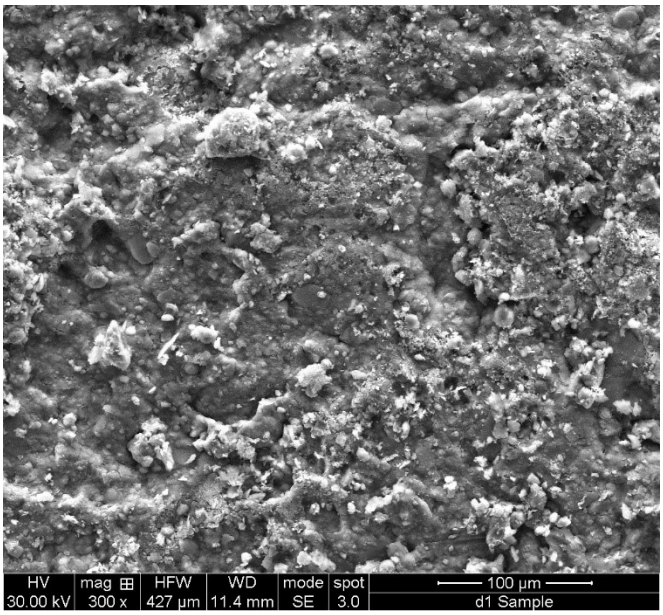

Figure 6.8 *– SEM photomicrograph of the 3D-printed soil. Top view of the filament. Magnification 300x.*

7. CHANGE IN THE TENSIONAL STATE OF A FINE-GRAINED SOIL DURING 3D PRINTING PROCESS

In this Chapter, the testing campaign carried out with the aim of study the change of the tensional state of a fine-grained soil during a 3D printing process will be described. To conduct this evaluation, oedometric tests have been performed on specimens obtained in the three different phases of the process:

- Before 3D printing:
  - soil in the as-received condition;
  - soil prepared to be inserted in the tank with the chosen water content of printing.
- During 3D printing:
  - soil inside the tank, undergoing the extrusion process.
- After printing:
  - 3D printed soil.

7.1 MATERIAL AND METHODS

Tested material

In this phase of the work, the soil called CC – Commercial Clay described on the chapter 2.1 has been tested. The main characteristics of the soil are reported in the following table 7.1.

Table 7.1 *– Main geotechnical properties of the soil called "CC" (specific gravity G_s, liquid limit LL, plastic limit PL, clay fraction f_{clay}, silt fraction f_{silt}, sand fraction f_{sand}).*

Soil ID	G_s	*LL*	*PL*	f_{clay}	f_{silt}	f_{sand}
[-]	[-]	[-]	[-]	[-]	[-]	[-]
CC	2.77	0.45	0.21	52	46	2

Specimens preparation

For all the phases of the process to be studied, oedometric specimens have been derived by driving the oedometric ring on the undisturbed sample relevant for each phase.

Packed soil

The fine-grained soil used for printing in this work is supplied by the manufacturer in a package made of a plastic material (figure 7.1). Once the packaging is removed, the oedometric specimen is obtained as shown in figure 7.2. In particular, after extracting the material needed using a nylon thread, the specimen is confined and driven by means of a lathe and a metal bar. Once extracted, the specimen is refined at the two ends by means of a nylon thread.

Figure 7.1 *– Packed soil as supplied by the manufacturer.*

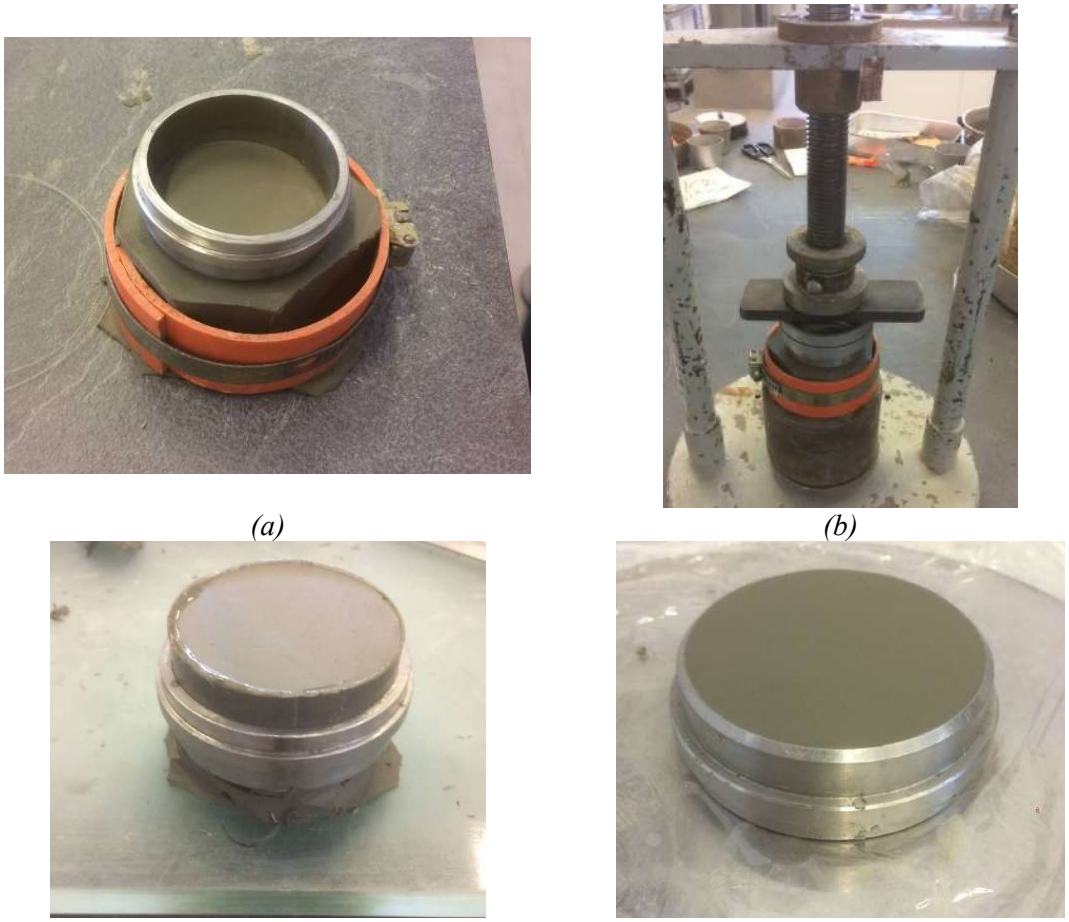

(a) *(b)*

(c) *(d)*

Figure 7.2 *– Specimen preparation. Confining of the soil (a), driving of the specimen by means of a lathe and a metal bar (b), specimen before refining (c) and refined specimen (d).*

Soil prepared for tank-filling

The specimen preparation is shown in figure 7.3.

Starting from the as-received condition, the soil is accurately mixed with distilled water to reach a consistency index CI close to 0.5 (corresponding target water content w = 0.30-0.32), to ensure adequate workability and limit the occlusion of air bubbles in the soil during the printing process.

Once processed, the geo-material is compacted manually and, to facilitate its insertion inside the tank, it is first inserted into a PVC pipe that would then pushed into the tank via a circular plate placed inside the tank – as explained in the previous Chapter 4.

Before the last step mentioned, the specimen is obtained by means of a lathe and a metal bar and the two ends are refined by means of a nylon thread.

(a)

(b)

(c)

(d)

(e)

(f)

(g)

(h)

Figure 7.3 *– Specimen preparation. Manual preparation of the soil adding distilled water (a); manual compaction of the soil (b); soil at the end of the manual compaction process (c); positioning of the PVC pipe (d); insertion of the PVC pipe in the soil (e); soil inside the PVC pipe (f); driving of the specimen (g); specimen refining by means of a nylon thread (h).*

Soil inside the tank

During the 3D printing process, the soil is extruded at a pressure of about 7 bar, or 700 kPa. To evaluate the hydro-mechanical characteristics of the soil in this phase of the process, the soil is extracted after having carried out some printing tests: the tank is dismantled, the geo-material is confined inside a PVC tube, the specimen is obtained (figure 7.4) by means of a lathe and a metal bar and the two ends are refined by means of a nylon thread.

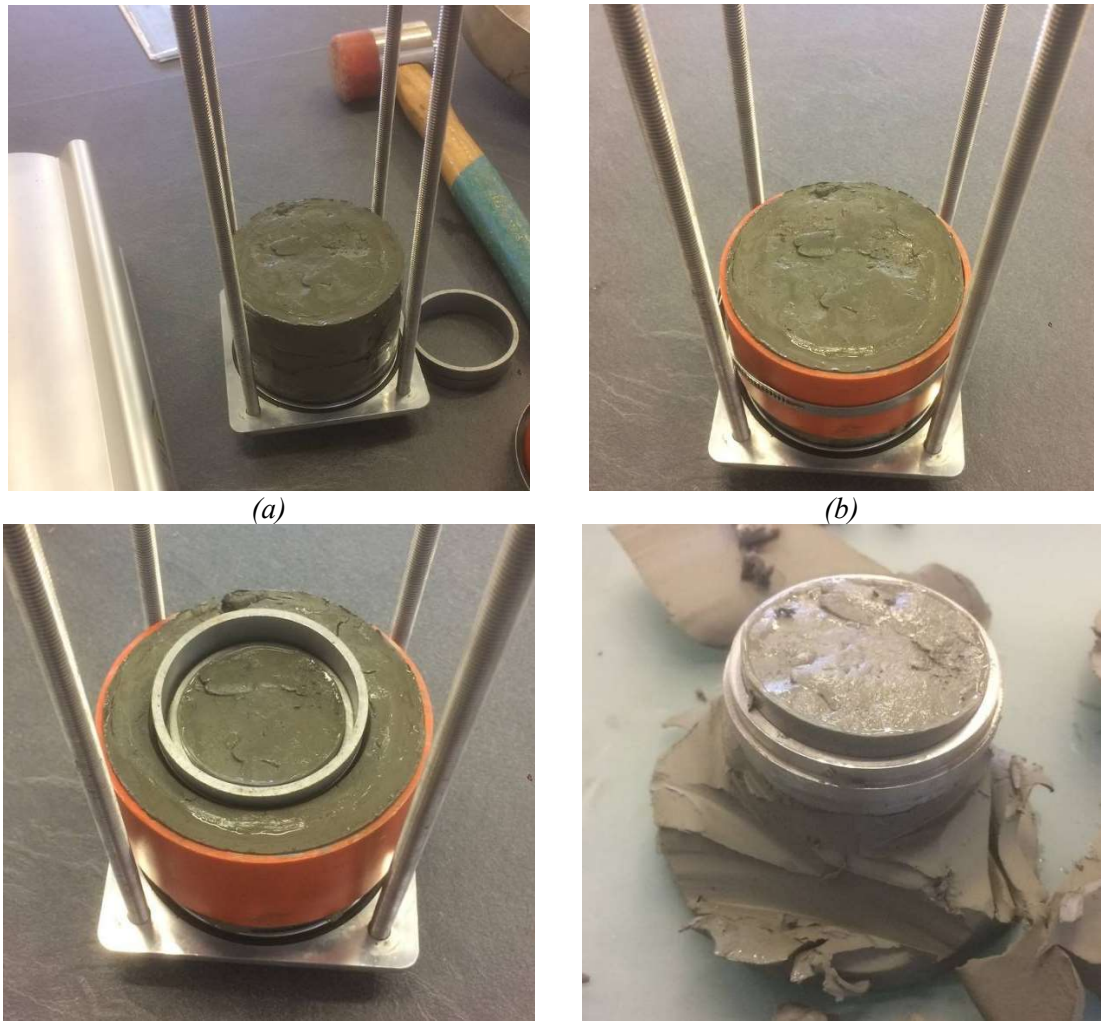

(a) *(b)*

(c) *(d)*

Figure 7.4 *– Specimen preparation. Extraction of the soil from the tank (a); confining with a PVC pipe (b); driving of the specimen (c); specimen refining (d).*

Soil after 3D printing

To explore a variety of macro-structural behaviors, for this phase of the 3D printing process, the specimens have been obtained printing three samples, with three different diameters of the nozzle – 1.41 mm, 1.96 mm, 3.1 mm – having no spacing amongst parallel filaments.

First, the G-code for each sample has been prepared, depending on the nozzle diameter. *Annex B* reports the first four layers of the G-code of the sample printed with the nozzle having a diameter size of 1.41 mm. The three complete G-codes can be found at the link:
https://drive.google.com/drive/folders/10qUUwVNcvvtEWXra8ip_UElZIYifOrSk?usp=sharing

The dimensions would change for each nozzle diameter, but the scheme was the same for each sample. Each squared layer consists of two external squared borders, while the core of the sample is a serpentine; odd layers had the serpentine oriented along the x-axis, even layers had the serpentine oriented along the y-axis. The barycentric distance of the serpentine arms has been defined following the criteria exposed on the previous Chapter 4, ensuring the contact without overlapping. The number of layers depends on the distance amongst each layer. Each sample had

a side of approximately 70 mm and a height of 25 mm, so to ensure the proper deriving of the oedometric specimens.

The extraction of the specimen (figure 7.5) has been conducted by infixing the oedometric ring – previously covered by Vaseline gel to avoid friction forces – in the 3D printed sample. The aim was to extract the core of the sample as to obtain a specimen in which only parallel filaments – avoiding then the border parts of the sample and the curving parts of the serpentines. Once the oedometric ring is infixed, the superior and the inferior parts of the sample is removed by means of a nylon thread.

(a)

(b)

Figure 7.5 *– Specimen preparation. 3D printing of a sample (a); driving of the specimen (b).*

In the table 7.2 the main geotechnical characteristics of the specimens extracted from the 3D printed samples are reported.

Table 7.2 *– Main geometrical and geotechnical characteristics of the tested specimens obtained from 3D printed samples.*

		before 3D printing		***during 3D printing***	***after 3D printing***					
		as received	*prepared*	*in the tank*	*1.41 mm*		*1.96 mm*		*3.1 mm*	
					A	B	0	B	0	B
w	*[-]*	0.27	0.32	0.28	0.30	0.30	0.32	0.30	0.36	0.32
e	*[-]*	0.762	0.99	0.87	1.00	0.96	1.00	1.13	1.22	1.06
S_r	*[-]*	0.99	0.9	0.89	0.84	0.86	0.88	0.73	0.95	0.84
n	*[-]*	0.43	0.5	0.47	0.50	0.49	0.50	0.53	0.55	0.51

Testing Set-Up

The testing set-up consists of a mechanical oedometric apparatus. In this type of machine the application of the effective vertical stress happens by putting a weight on a mechanical arm. The load is then transferred to the superior part of the cylindrical specimen, that is put in a box filled with water. The machine is equipped with LVDT transducer linked to a software; the electrical signal is transferred to the software and the displacements are registered.

The loading path followed during the tests is reported in table 7.3:

Table 7.3 *– Loading and unloading steps carried out in the oedometric tests.*

	Step n. [-]	*Effective stress applied* σ'_v *[kPa]*					
		before 3D printing		*during 3D printing*	*after 3D printing*		
		as received	*prepared*	*in the tank*	*1.41 mm*	*1.96 mm*	*3.1 mm*
Loading	1	1	1	1	1	1	1
	2	5	10	10	5	10	5
	3	10	20	20	10	20	15
	4	20	40	40	20	40	25
	5	40	80	80	40	79	46
	6	80	149	149	79	151	85
	7	149	259	259	151	296	155
	8	259	591	591	296	566	302
	9	591	1180	1180	566	1167	599
	10	1180	2410		1167	2369	1191
	11		3685		2334		2394
Unloading	1	591	1180	591	566	566	599
	2	259	259	259	151	151	155
	3	149	80	149	40	40	46
	4	80		80	10		
	5	40					
	6	20					

The first loading step is referred to the only application of the loading head. Each loading step had a duration of 24 hours, that was the time necessary to consolidation of the specimens to complete. In the loading phase, a geometric series for the increments has been followed, with ratio equal to two: doubling so the load applied for each step. The unloading phase followed a geometric series too, but with a ratio of four. The water level has aways been maintained constant to ensure the saturation of the specimen during the test.

7.2 RESULTS AND ANALYSIS

Data collection

For each step of the test, the software associated to the LVDT connected to the head of the specimen returns the value of the vertical displacements during time. As shown in the following table 6.4, starting from the initial time of the test, the next six values of the displacements were collected with an elapsing time of one second, then the elapsed time from a reading to another followed a geometric series with ratio equal to two, doubling then the elapsed time for each reading until reaching the 24 hours.

This data collection scheme has been followed in order to capture the shape of the displacement curve (table 7.4).

Table 7.4 *– Collected data.*

Reading n. [-]	*Time t [s]*
1	0
2	1
3	2
4	3
5	4
6	5
7	6
8	15
9	30
10	60
11	120
12	240
13	480
14	900
15	1800
16	3600
17	5400
18	7200
19	10800
20	14400
21	21600
22	28800
23	43200
24	57600
25	72000
26	86400

Data elaboration

The data elaboration has been executed with the following layout:

- data cleansing;
- construction of the displacement vs time curves in semi-logarithmic chart for each loading/unloading step;

- identification of the ρ_0 and ρ_{100} values by means of the log time method corresponding to the value of the displacement at the beginning of the consolidation process – when the average degree of consolidation is equal to 0 – and at the end of the consolidation process – when the average degree of consolidation is equal to 1;
- determination of the void index relating to the end of the consolidation process of each step – when the vertical displacement equal to ρ_{100} has been therefore reached;
- determination of the compression index of the loading phase and of the swelling index of the unloading phase;
- construction of the oedometric curves
- determination of the preconsolidation stress with the graphic Casagrande method.

Data analysis

The analysis of the **vertical displacement vs time curves** has been conducted on a semi-logarithmic chart. The displacement axis has been represented with positive values when a subsidence occurs.

It is interesting to highlight that a typical behavior has been observed on the 3D printed specimens: as it can be seen in figure 7.6, in the first 10 seconds of the loading the slope of the curve is steeper than expected. This behavior can be explained taking into account the double structured nature of the specimens: at the beginning of the loading step, the water retained on the macro-pores would be expelled easily and a prevalent reduction of the volume of the macro-pores occurs; after that, the consolidation process would affect mostly the micro-structure.

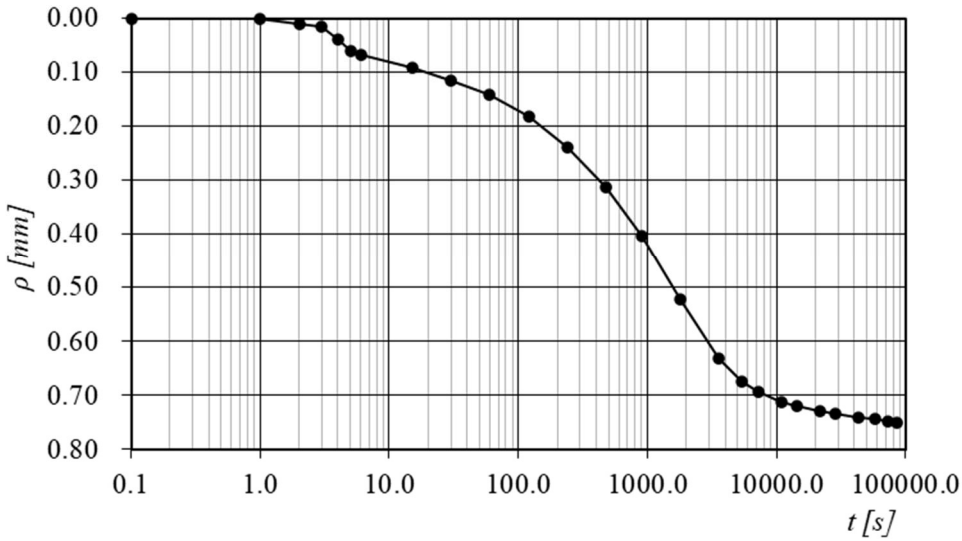

Figure 7.6 *– Typical displacement vs time curve obtained from the executed oedometric tests for the 3D printed specimens.*

The analysis and the comparison of the oedometric curves obtained for the specimens representative of the three different phases of a 3D printed process gives permit to describe the evolution of the stress state during the 3D printing process.

In the figure 7.7, the obtained oedometric curves are represented.

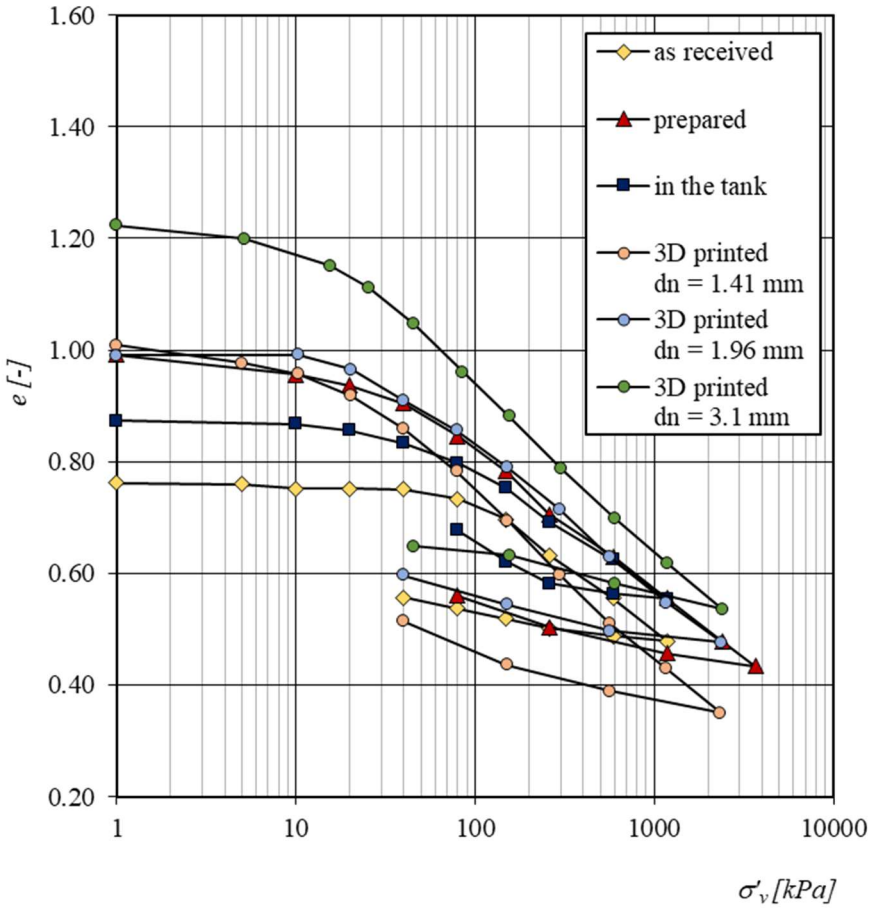

Figure 7.7 *– Oedometric curves obtained.*

Table 7.5 reports the index properties of the specimens at the beginning of the oedometric tests and the values of the preconsolidation stress determined for each tested specimen.

Table 7.5 *– Specimens initial index properties and preconsolidation stress.*

		before 3D printing		***during 3D printing***	***after 3D printing***					
		as received	*prepared*	*in the tank*	*1.41 mm*		*1.96 mm*		*3.1 mm*	
w	*[-]*	0.27	0.32	0.28	0.30	0.30	0.32	0.30	0.36	0.32
e	*[-]*	0.762	0.99	0.87	1.00	0.96	1.00	1.13	1.22	1.06
S_r	*[-]*	0.99	0.9	0.89	0.84	0.86	0.88	0.73	0.95	0.84
n	*[-]*	0.43	0.5	0.47	0.50	0.49	0.50	0.53	0.55	0.51
σ'_{vp}	*[kPa]*	150	30	100	10-30					

It is possible to notice that the soil is supplied by the producer with an evident preconsolidation stress estimated at 150 kPa.

Once prepared, before insertion into the extrusion tank, the soil loses this characteristic due to the manual processing of the operator; moreover, the addition of distilled water in order to obtain the pre-set water content for printing (w = 0.30-0.36) causes further effect by increasing the porosity index.

Once the material is inserted into the tank and subjected to the extrusion process, it is partially consolidated. However, this consolidation is only partial because there is no time for the excess pore water pressure to be dissipated, in compliance with the criterion exposed by Worth & Holsby (1984); if the criterion wouldn't had met, the printing process would have stopped. The preconsolidation stress of the soil in this phase is of the order of 100 kPa, slightly lower than that one relative to the packed soil.

Proceeding with the 3D printing process, the soil is extruded from the screw and deposited on the printing base. This operation, in conjunction with the macro-porosity induced by the print geometry, causes respectively a reduction in the preconsolidation stress and an increase in the void index.

There is some similarity on the behaviour of the soil once prepared and once 3D printed; this can be interpreted as that the printing process causes the same effect that the manual preparation carried out by the operator causes on the packed soil, that is, an increase in porosity index and a decrease in the preconsolidation stress.

Other considerations can be made analyzing the specimens obtained from the samples 3D printed with the three different nozzles shown together on figure 7.8. It can be noticed that:

- the increasing of the nozzle diameter is correlated with an increase on the initial void ratio;
- while the position of the curves is related to the macro-structure of the specimens, the shape of them is related to the micro-structure, presenting all of them similar values of the compression index and of the swelling index, as reported in table 7.7.

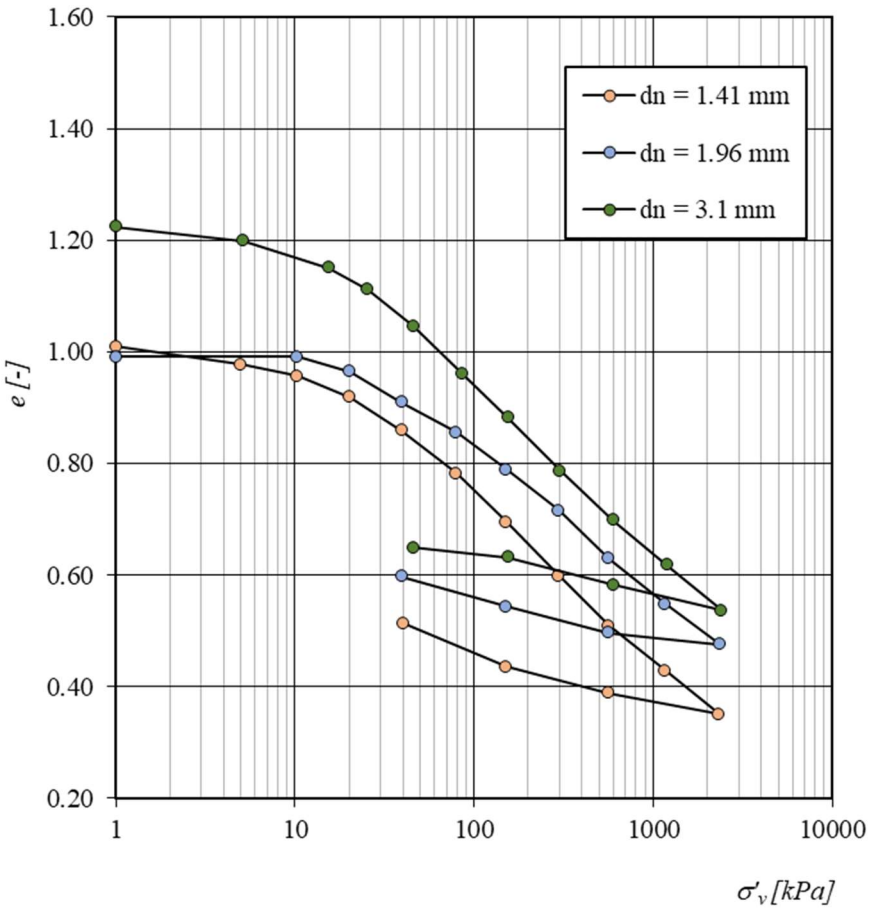

Figure 7.8 *– Oedometric curves obtained from the executed oedometric tests for the 3D printed specimens.*

Table 7.7 *– Values of the compressibility indexes and of the swelling indexes depending on the nozzle diameter.*

	Cc ***[-]***	***Cs*** ***[-]***
d_n = *1.41 mm*	0.27	0.07
d_n = *1.96 mm*	0.21	0.05
d_n = *3.1 mm*	0.29	0.07

7.3 SUMMARY

The experimental campaign described in this Chapter allowed to investigate how the tensional state of a soil changes when 3D printed. The analysis of the oedometric tests showed that, while the pressure applied on the soil inside the tank increases the preconsolidation stress and reduces the void ratio, the passage through the extrusion chamber – in which the internal screw

forces the movement of the soil – leads to a reduction on the preconsolidation stress, showing the same value held after by-hand preparation.

The comparison between the oedometric curves of the 3D printed specimens confirmed the dependence of the index properties on the diameter of the nozzle – and thus on the diameter of the filaments, while the compressibility behaviour is related to the characteristics of the soil itself.

8. MULTIMATERIAL 3D PRINTING OF FINE-GRAINED SOILS

In this Chapter, the experimental campaign carried out at the Geotechnical Laboratory of the University of Los Andes (Bogotá, Colombia) during the research project's period abroad is presented. The Geotechnical Laboratory in which the GeoSI Group led by Prof. Caicedo Hormaza operates is equipped with a multimaterial 3D printer – developed by Pua et al. (2018) and described in the previous Chapter 4. The purpose of the 3D printer is to create spatially variable physical models of soils accordingly to the random fields theory (Pua & Caicedo, 2021): with the currently available standard laboratory equipment is indeed difficult to reproduce 3D physical models faithful to the numerical ones.

The challenge was to find a scientific method to apply to determine the printing parameters to use when writing the G-codes depending on the nozzle diameter and on the consistency characteristics of the soils – that in this case would've been at the liquid state.

The experimental campaign here described has thus been developed with the aims of:

- characterize the custom multimaterial 3D printer with respect to:
    - the soils nature and consistency;
    - the diameter of the nozzles;
- obtain multimaterial samples faithful to the numerical models assuring 1 cm^3 of printing precision.

8.1 MATERIALS AND METHODS

Tested materials

In previous studies conducted by the investigation group of GeoSI, it has been chosen to use seven materials with different percentage of kaolin and bentonite to have soils with different values of consistency limits; the same soil mixtures colorants described on the previous Chapter 2.3 and called "Group B" were then used during this phase of the investigation. The main characteristics of them are reported in table 8.1:

Table 8.1 *– Main geotechnical properties of the soils of "Group B" (percentage of kaolin W_K/W_{tot}, percentage of bentonite W_Q/W_{tot}, percentage of colorant W_C/W_{tot}, specific gravity G_s, liquid limit LL, plastic limit PL).*

Soil ID	$W_{K,s}/W_{tot}$	$W_{B,s}/W_{tot}$	$W_{C,s}/W_{tot}$	G_s	*LL*	*PL*
[-]	*[%]*	*[%]*	*[%]*	*[-]*	*[-]*	*[-]*
S1	100	0	0	2.7	0.87	0.44
S2	68	23	9	2.73	1.20	0.32
S3	55	33	12	2.74	1.48	0.26
S4	44	44	12	2.75	1.96	0.24
S5	31	52	17	2.83	2.04	0.20
S6	21	63	16	2.82	2.34	0.23
S7	10	73	17	2.76	3.00	0.29
S8	0	100	0	2.84	3.48	0.30

To ensure the extrudability of the soils and to meet the requirements of the research work carried out by the GeoSI Group, all the soil mixtures have been tested at a water content equal to 1.5 times the liquid limit of each of them.

Testing Set-Up

The testing set-up consists of the custom multimaterial 3D printer developed and built by the GeoSI Group of the University of Los Andes described in the previous Chapter 4.1, whose main characteristics are here described: the printing system is composed of eight independent 2.3-liter air-tight tanks converging into a commercial hydraulic multiplexor valve having eight inputs and one output. The multiplexor valve, connected to an interchangeable nozzle, is fixed on a plate moving on the three dimensions, covering a printing volume of 30 cm x 30 cm x 30 cm. To the valve is connected an interchangeable nozzle.

In this 3D printer, the efflux of the soil from the tanks is guaranteed by stepper motors that control the ram displacement in each tank: the soil flows to the multiplexing valve and the filament is printed by means of an extrusion process.

In this configuration of the 3D printer, the movements on the three dimension of the multiplexor and the switch amongst the tanks is controlled by the G-code, while the rotational speed of the stepper motors is controlled by an external software.

G-Code generation

As for what has been chosen in the other phases of the work, it hasn't been used any commercial slicer software to generate the necessary G-codes.

As previously exposed in Chapter 4, in this 3D printing system the extrusion of the material is not controlled by the G-code, but from an external software; therefore the E-axis is not present in the G-codes used in this work. Moreover, seen the geometry of the printing to be performed, it wasn't necessary to program a G-code generator. Instead, all of the G-codes have been wrote from scratch.

Three structures of G-codes have been generated and are here described.

Points

- 3D printer booting;
- positioning;
- waiting time to allow extrusion;
- 3D printer powering down.

Lines:

- 3D printer booting;
- initial positioning;
- motion to the final position;
- 3D printer powering down.

Multimaterial lines:

- 3D printer booting;
- initial positioning;
- motion to the changing material position;
- switching tank;
- waiting time to allow switching;
- motion to the final position;
- 3D printer powering down.

In the Annexes C, D and E three examples of these G-codes are presented.

8.2 CHARACTERIZATION OF THE CUSTOM MULTIMATERIAL 3D PRINTER

In the current layout of the multimaterial 3D printer, the **printing velocity** – as the velocity with which the nozzle moves in the three dimensions – is controlled by the G-code, while the **extrusion velocity** – as the velocity with which the soil is extruded by the nozzle – is controlled by an external software by means of the imposition of a rotational speed to the stepper motors connected to each of the rams inside the relative air-tight tanks.

It was therefore necessary to study the functioning of the multimaterial 3D printing, developing a method with which associate printing velocity and extrusion velocity for the studied materials.

Identification of the problem

The printing velocity and the extrusion velocity are independent one to another, so the characterization problem can be expressed and solved by decoupling the two velocities, and thus the two movements of the extruder and of the printer: if the printer isn't moving, the volume of the extruded filament V_{ext} would be equal to the extrusion velocity v_{ext} multiplied by the extrusion time t_{ext} and for the area of the nozzle A_n:

$$V_{ext} = v_{ext} t_{ext} A_n$$

As confirmed by the testing campaign described in Chapter 3 and in Chapter 5, the process can be supposed to be undrained, so during the extrusion no changes in volume would occur, but only in shape; in particular, an ovalization of the cross section of the filament is expected maintaining the same area. Dividing the volume of the extruded filament for the area of the nozzle, the ideal length of the extruded filament L_{ext} is derived (figure 8.1):

$$L_{ext} = \frac{V_{ext}}{A_n}$$

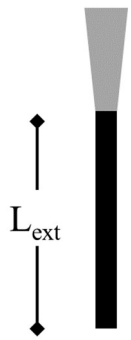

Figure 8.1 *– Extrusion schematization.*

When the printer is moving with a printing velocity v_{prt}, three scenarios could happen:

- the printing velocity is too low: the soil would be extruded in a length shorter than the extrusion length $L_{prt} < L_{ext}$ with accumulation of the soil around the nozzle – as the area of the filament would be bigger than the nozzle area (figure 8.2a);
- the printing velocity is too high: the soil would be extruded in a length wider than the extrusion length $L_{prt} > L_{ext}$ with dispersion of the soil around the nozzle – as the area of the filament would be smaller than the nozzle area (figure 8.2b);
- the printing velocity is adequate; the material would be extruded in a length equal to the extrusion length $L_{prt} = L_{ext}$ (figure 8.2c)

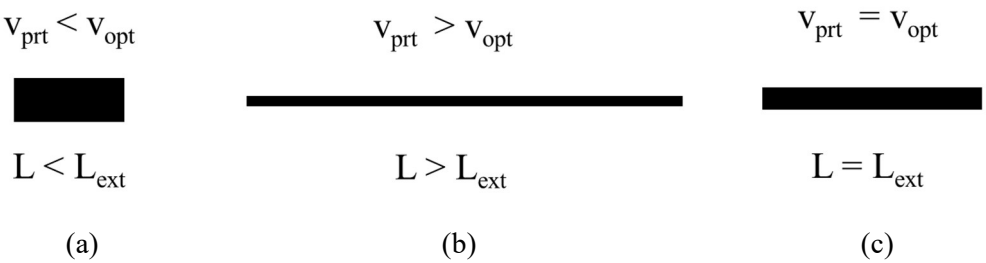

Figure 8.2 *– Schematization of the three possible scenarios: (a) slow printing, (b) fast printing, (c) optimum printing.*

Proposed method

The following method has been followed in order to associate the adequate printing velocity to each extrusion velocity:

- set an extrusion velocity v_{ext};
- extrude each material for a fixed time t_{ext} using a point-type G-code;
- measure the weight of the extruded material W;
- calculate the correspondent volume V under the hypothesis of saturated soil;
- calculate the correspondent extruded length L_{ext} considering the ideal cylinder with the same diameter of the nozzle;
- determine the optimum printing velocity v_{ext} dividing the extruded length L_{ext} for the extrusion time t_{ext};
- verify the obtained results printing a line with the derived extrusion velocity using a line-type G-code.

The testing campaign included the 8 types of soils at 5 different values of the extrusion velocity with 2 nozzles having different diameter, for a total of 80 tests. Each of them has been conducted three times to avoid measuring errors and the water content of the tested soils has been determined after each test, to confirm that the expected values would match the real ones.

Experimental results

In the following figure 8.3, the experimental results of the characterization are reported; the two velocities resulted linearly dependent, and the relationship between them would not relate with the type of soil tested, confirming the hypothesis of undrained condition during the extrusion process.

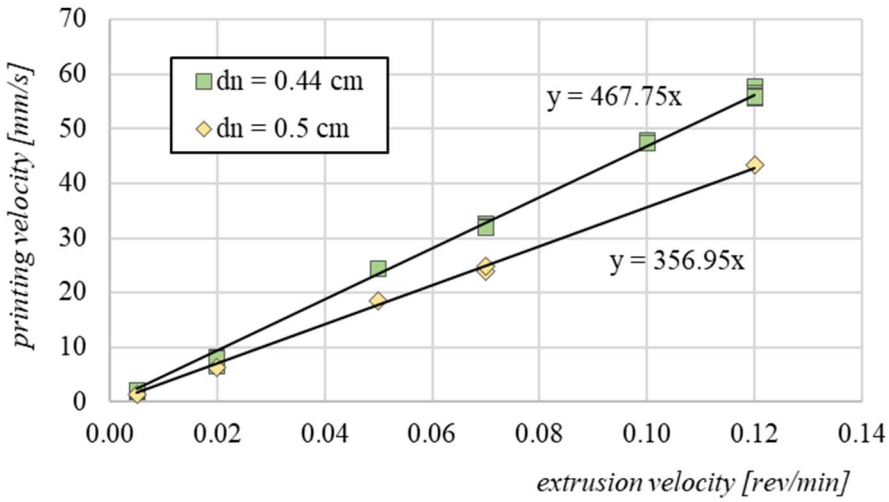

Figure 8.3 *– Extrusion velocity vs printing velocity experimental curves with two different nozzle diameters*

Moreover, due to the undrained conditions of the process, the slope of the line relating the two velocities can be expressed in terms of the area of the nozzle.

In particular:

$$v_{prt} = \frac{70}{A_n} v_{ext}$$

With:

- v_{prt} expressed in mm/s;
- A_n expressed in cm^2;
- v_{ext} expressed in rev/min.

The multimaterial 3D printer has been therefore characterized; if the process develops in undrained condition, known the nozzle diameter and choosing an extrusion velocity, the printing velocity is determined.

8.3 FAITHFUL MULTIMATERIAL 3D PRINTING

The last part of the work conducted with the multimaterial 3D printer has involved the investigation of a method to apply in order to guarantee a faithful reproduction of the 3D model.

With the performed work we have set the basis to perform a 3D printing able to faithfully reproduce the target 3D model. In particular, after preliminary testing it was possible to define a list to precautions that need to be considered:

- it is necessary to communicate to the machine to switch the tank through the G-code. To do so, it is only needed to create a block having as only word the letter T + the number of tank (from 0 to 7);

- in the current layout of the custom multimaterial 3D printer, a little time is necessary for the machine to complete the command, therefore, it has been chosen to stop the printing movements during the execution of the command. To do so, it is needed to create a block having instructions on how many seconds and milliseconds to pause.
- once the switching of the tank is effective, part of the multiplexor valve would still be filled with the soil of the previous tank. It is therefore necessary to calculate that volume, relating it to the correspondent extrusion length. Once known this value, it is necessary to anticipate the position in which applying the tank switching command, to guarantee that the material would change where requested.

Once the volume has been calculated and the time would have been measured, the G-codes have been wrote, switching multiple tanks. An example of a G-code successfully used is available in the Annex E.

Experimental campaign

The testing campaign included therefore the following steps:

- determination of the volume inside the valve;
- determination of the extrusion length to be considered depending on the nozzle used;
- determination of the time necessary to switch tank.

Depending on how many switches are necessary, the correct time to stop the printing is calculated.

Figure 8.4 shows one of the multimaterial printing carried out. It is a serpentine with 15 arms, the initial point being the one on the upper-right corner. The target was to obtain the change of the material in the midpoint of each even arm. As it can be seen, in some of the cases the target has not been reached: in the fourth arm (from soil S5 to soil S6), the switching time was underestimated, and the 3D printer started again the movement when the switching wasn't completed. In the eight and in the twelfth arm (from soil S4 to soil S2 and from soil S7 to soil S1), on the contrary, the switching time was overestimated: the duration of the stop was too high and the extrusion resumed when the 3D printer was still stopped. In cases like for the tenth and the fourteenth arms (from soil S2 t soil S7 and from soil S1 to soil S8), the switching time was a little overestimated, the soil accumulated in the stopping point and when the movement began again, the material extruding from the nozzle was held by the one on the accumulation point.

Other cases of underestimation of the switching time can be seen in figure 8.5; in those cases, the target of changing soil in the midpoint without problems occurred only in the tenth arm of the serpentine (switching from soil S6 to soil S7).

Figure 8.4 *–Multimaterial serpentine. Errors on estimation of the tank-switching time.*

Figure 8.5 *–Multimaterial serpentine. Underestimation of the tank-switching time.*

Finally, in figure 8.6 is showed a case of multimaterial 3D printing in which the target of changing soil in the midline of the even arms has been reached thanks to a correct estimation of the time necessary to the tank to be switched.

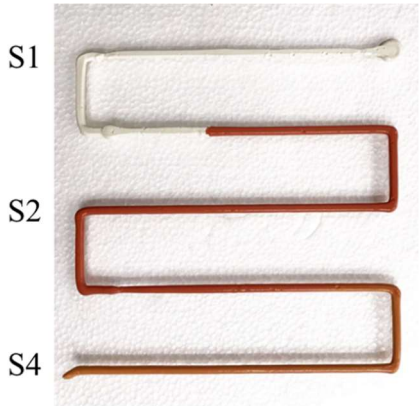

Figure 8.6 *–Multimaterial serpentine. Correct estimation of the tank-switching time.*

The measurements led to the definition of the values collected in table 8.2.

Table 8.2 *– Parameters to be used in the 3D printing of a multimaterial line.*

		dn = 0.44 cm	*dn = 0.5 cm*
extrusion length	*[mm]*	80	71.6
tank switching time	*[s]*	0.533	

8.4 SUMMARY AND FUTURE DEVELOPMENTS

The objective of the work conducted at the Geotechnical Laboratory of the University of Los Andes was to ensure the faithful reproduction of 3D models generated with the random field theory by means of the custom multimaterial 3D printer with which the laboratory is equipped.

The relationship between printing velocity and extrusion velocity that would guarantee an optimum 3D printing has been determined with an extensive experimental campaign, and it has been related with the area of the nozzle.

In the last part of the experimental campaign, 3D printing of multimaterial lines has been conducted, observing that the role played by the time necessary to the tank to switch is fundamental on the reaching of the target point of changing material and therefore on the ensuring a faithful 3D printed reproduction of the 3D model. The work conducted led to a good estimation of that, but more tests need to be conducted to validate the determined parameters.

Future developments of the research would also involve the extension of the double-porosity model described in Chapter 5 to the multi-material 3D printed specimens, allowing the prediction of the index properties of them.

CONCLUSIONS

The present thesis aimed at reading the process of 3D printing of fine-grained soils from a geomechanical point of view. After a discussion over how the 3D printing technologies get in touch with the geomechanical field, it has been highlighted that, until now, on one hand 3D printing has been used as a tool to conduct geomechanical characterization reproducing some characteristics of the soils or rocks by means of classical printing materials e.g. polymeric filaments; on the other hand, when fine-grained soils have been used as printing materials, they have been characterized without taking into account their multiphasic nature.

Three groups of fine-grained soils have been used for the investigation to analyze a vast range of behaviors of the fine-grained soils linked to mineralogic composition (kaolinite, quartz, and bentonite) and consistency (plastic and liquid state). The technology object of this work has been then presented, describing the characteristics of the 3D printers used during the investigation and outlining the programming language necessary to communicate with the equipment. Three methods have been used to write the G-codes used in this investigation – programming from scratch, mathematically automatizing the process via MS Excel and via a Python script.

First of all, the characterization of the extrusion process was analyzed, being the extrusion the main process to which a soil is subjected when 3D printed. To this aim, the extrusion process was considered as a combination of consolidation and efflux. The experimental campaign, constituted of extrusion tests and oedometric tests, aimed at evaluating the role played by the soils characteristics and geometry of the extrusion system on the outcome of the extrusion itself. Results showed that the parameters to consider are the coefficient of consolidation of the soil, the extrusion length and the time of extrusion.

Passing to the investigation of the 3D printing process, a double-porosity model was proposed to predict the index properties of 3D printed specimens starting from the geotechnical characteristics of the fine-grained soil and the specimens' geometry. After that, the model was validated through its application to further specimens characterized by different value of the adimensional spacing amongst parallel filaments. Results showed that the model tends to overestimate the porosity characteristics of the specimens. Further studies are recommended to improve the predicting ability of the model, e.g. through the addition the deformability characteristics of the soil as model parameters.

The research then focused on the fabric of a 3D printed clayey soil. It was observed that the particle arrangements and size, orientation and shape of pores are strongly linked to the 3D printing operation. In particular, the macropores are the result of the relative position of the filaments and their initial distortion in quasi-undrained conditions. In addition, particle arrangement within the soil filament is strongly anisotropic due to the rotative movement of the soil in the extruder. Moreover, intra-assemblage pores located in between the clayey assemblages, and those resulting from different particle contacts (both face-to-face and edge-to-face contacts), influence the microporosity.

Further on, the experimental campaign investigated the evolution of the tensional state of a soil before, during and after the 3D printing process through oedometric tests. It was seen that the pressure applied on the soil inside the tank increases the preconsolidation stress and reduces the void ratio. In contrast, the successive passage through the screw of the extrusion chamber reduces the preconsolidation stress, that goes back to the value determined after by-hand preparation. In addition, it was confirmed the relation between the index properties and the diameter of the nozzle i.e. the diameter of the filaments, whereas the compressibility behaviour is related to the characteristics of the soil itself.

The experimental campaign conducted at the Geotechnical Laboratory of the University of Los Andes aimed at ensuring the faithful reproduction of 3D models generated with the random field theory by means of their custom multimaterial 3D printer. The objective was achieved by determining the relationship between printing velocity, extrusion velocity as a function of the area of the nozzle. Finally, the 3D printing of multimaterial lines was optimized identifying the key parameters influencing the process, i.e. time necessary to switch tank and volume of the valve. Further studies are needed to validate the determined the parameters by considering a wider range of printing set-up.

In conclusion, the outcomes of the PhD project were found encouraging and suggest to deepen the research on 3D printing of fine-grained soils. Focusing on the laboratory scale, it was possible to determine which variables are relevant in the 3D printing process and how they are related with the characteristics of the 3D printed sample. The results obtained so far can help in the engineering of fabric-controlled samples with target geometric and hydro-mechanical characteristics. In this way, it would be possible to make a contribution in all of the fields in which fine-grained soils are used as printing material.

This PhD thesis can be considered a starting point for the research in this topic, and further studies are recommended to expand the knowledge on it:

- widening the range of the input parameters of the machines and of the fine-grained soils to print specimens with different index properties and hydro-mechanical properties;
- refining the double-porosity model taking into account the actual deformation of the filaments that would depend on the hydro-mechanical characteristics of the soil and on the number of layers above it;
- extending the validity of the double-porosity model to the multimaterial 3D printed specimens.

REFERENCES

Bourke, M., Viles, H., Nicoli, J., Lyew-Ayee, P., Ghent, R., & Holmlund, J. (2008). Innovative applications of laser scanning and rapid prototype printing to rock breakdown experiments. *Earth Surface Processes and Landforms: The Journal of the British Geomorphological Research Group*, *33*(10), 1614-1621.

Cordão Neto, M. P., Hernández, O., Reinaldo, R. L., Borges, C., & Caicedo, B. (2018). Study of the relationship between the hydromechanical soil behavior and microstructure of a structured soil. *Earth Sciences Research Journal*, *22*(2), 91-101.

Dal Ferro, N., & Morari, F. (2015). From real soils to 3D-printed soils: Reproduction of complex pore network at the real size in a Silty-loam soil. *Soil Science Society of America Journal*, *79*(4), 1008-1017.

Delage, P., & Lefebvre, G. (1984). Study of the structure of a sensitive Champlain clay and of its evolution during consolidation. *Canadian Geotechnical Journal*, *21*(1), 21-35.

Ferrari, A., Bosch, J. A., Baryla, P., & Rosone, M. (2022). Volume change response and fabric evolution of granular MX80 bentonite along different hydro-mechanical stress paths. *Acta Geotechnica*, 1-12.

Garzón, L. X., Caicedo, B., Sánchez-Silva, M., & Phoon, K. K. (2015). Physical modelling of soil uncertainty. *International Journal of Physical Modelling in Geotechnics*, *15*(1), 19-34.

Gomez, J. S., Chalaturnyk, R. J., & Zambrano-Narvaez, G. (2019). Experimental investigation of the mechanical behavior and permeability of 3D printed sandstone analogues under triaxial conditions. *Transport in Porous Media*, *129*(2), 541-557.

Grim, R. E., & Guven, N. (2011). Bentonites: geology, mineralogy, properties and uses. Elsevier.

Hanaor, D. A. H., Gan, Y., Revay, M., Airey, D. W., & Einav, I. (2016). 3D printable geomaterials. *Géotechnique*, *66*(4), 323-332.

Ju, Y., Xie, H., Zheng, Z., Lu, J., Mao, L., Gao, F., & Peng, R. (2014). Visualization of the complex structure and stress field inside rock by means of 3D printing technology. *Chinese science bulletin*, *59*(36), 5354-5365.

Kayabali, K., & Tufenkci, O. O. (2010). Determination of plastic and liquid limits using the reverse extrusion technique. *Geotechnical Testing Journal*, *33*(1), 14-22.

Kayabali, K., Üstün, A. B., & Özkeser, A. (2015). Refinement of the reverse extrusion test to determine the two consistency limits. *Bulletin of the Mineral Research and Exploration*, *150*(150), 131-144.

Khoshnevis, B. (2004). Automated construction by contour crafting—related robotics and information technologies. *Automation in construction*, *13*(1), 5-19.

Klein, C., Hurlbut, C. S., & Dana, J. D. (1993). *Manual of mineralogy*.

Mansoori, M., Kalantar, N., & Palmer, W. (2018, June). Handmade by Machine: A Study on Layered Paste Deposition Methods in 3D Printing Geometric Sculptures. In *Proceedings of the Conference Fabrication and Sculpting Event (FASE) 2018At: Instituto Superior Técnico, Lisbon, Portugal* (pp. 6-8).

Martin, P. J., Wilson, D. I., & Bonnett, P. E. (2006). Paste extrusion through non-axisymmetric geometries: Insights gained by application of a liquid phase drainage criterion. *Powder technology*, *168*(2), 64-73.

Matsumura, S., & Mizutani, T. (2015). 3D printing of soil structure for evaluation of mechanical behavior: Acta Stereologica: Proceedings of the 14th International Congress for Stereology and Image Analysis. *Liège, Belgium, July*, 6-10.

Muñoz-Castelblanco, J. A., Pereira, J. M., Delage, P., & Cui, Y. J. (2012). The water retention properties of a natural unsaturated loess from northern France. *Géotechnique*, *62*(2), 95-106.

Perrot, A., Rangeard, D., & Courteille, E. (2018a). 3D printing of earth-based materials: Processing aspects. *Construction and Building Materials*, *172*, 670-676.

Perrot, A., Rangeard, D., Nerella, V. N., & Mechtcherine, V. (2018b). Extrusion of cement-based materials-an overview. *RILEM Technical Letters*, *3*, 91-97.

Pua, L. M., & Caicedo, B. (2021). Reproducing the inherent variability of soils using a three-dimensional printer. *International Journal of Physical Modelling in Geotechnics*, *21*(6), 295-313.

Pua, L. M., Caicedo, B., Castillo, D., & Caro, S. (2018). Development of a 3D clay printer for the preparation of heterogeneous models. In *Physical Modelling in Geotechnics* (pp. 155-160). CRC Press.

Romero, E., & Simms, P. H. (2008). Microstructure investigation in unsaturated soils: a review with special attention to contribution of mercury intrusion porosimetry and environmental scanning electron microscopy. *Geotechnical and Geological engineering*, *26*(6), 705-727.

Terzaghi, K., Theoretical Soil Mechanics, and Jonh Wiley. "Sons." *New York*(1943).

Verástegui-Flores, R. D., & Di Emidio, G. (2014). Assessment of clay consistency through conventional methods and indirect extrusion tests. *Applied clay science*, *101*, 632-636.

Whyte, I. L. (1982). Soil plasticity and strength--a new approach using extrusion. *Ground Engineering*, *15*(1).

Wroth, C. P., & Houlsby, G. T. (1984). Applications of soil mechanics theory to the processing of ceramics. In *L.L. Hench, D.R. Ulrich (Eds.), Ultrastructure processing of ceramics, glasses and composites, Wiley, New York, USA, 1984*, pp. 448–463.

Yuan, S., Liu, X., Romero, E., Delage, P., & Buzzi, O. (2020). Discussion on the separation of macropores and micropores in a compacted expansive clay. *Géotechnique Letters*, *10*(3), 454-460.

ANNEXES

ANNEX A

G-code generator script programmed with Python language

```
#!/usr/bin/env python
# coding: utf-8

import math
import matplotlib.pyplot as plt
import numpy as np

# Parameters ####

d = float(input("Please insert nozzle diameter: [mm] "))
side = float(input("Please insert useful size: [mm] "))
i = float(input("Please insert filament barycentric spacing: [mm]
"))
height = float(input("Please insert specimen height: [mm] "))
k = float(input("Please insert interlayer relative distance: [0-1]
"))
filename = input("Please define output filename: [w/o extension]
")

filamentsNumber = math.ceil(side / i)
effectiveSide = i * filamentsNumber
numberOfLayers = math.ceil(height/(d*k))
# 1. Internal Border ####

def buildInternalBorder(effective_side, i, z):
    internalBorder                                                  =
[(i,i,z),(i,effective_side+2*i,z),(effective_side+2*i,
effective_side+2*i,z),(effective_side+2*i,i,z),(i,i,z)]
    internalBorder = np.array(internalBorder)
    rawDistances = np.diff(internalBorder, axis=0)
    extrusionDistances                                              =
np.concatenate(([0],np.hypot(rawDistances[:,0], rawDistances[:,1])))
    extrusionDistancesCumSum = np.cumsum(extrusionDistances)
    result                                                          =
np.concatenate((internalBorder,extrusionDistancesCumSum.reshape(-
1,1)),axis=1)
    return result

# 2. External border ####

def buildExternalBorder(effective_side, i, z):
    externalBorder                                                  =
[(0,0,z),(0,effectiveSide+3*i,z),(effectiveSide+3*i,
effectiveSide+3*i,z),(effectiveSide+3*i,0,z),(0,0,z)]
    externalBorder = np.array(externalBorder)
    rawDistances = np.diff(externalBorder, axis=0)
```

```
        extrusionDistances                                          =
np.concatenate(([0],np.hypot(rawDistances[:,0], rawDistances[:,1])))
        extrusionDistancesCumSum = np.cumsum(extrusionDistances)
        result                                                      =
np.concatenate((externalBorder,extrusionDistancesCumSum.reshape(-
1,1)),axis=1)
        return result

    # 3. Snake ####

    def buildSnakeX(effective_side, i, filaments_number, z):
        snake = []
        f_ = 0
        for j in range(0,filaments_number,2):
            if f_ == filaments_number: break
            snake.append((2*i,(2+j)*i,z))
            snake.append((effective_side+i,(2+j)*i,z))
            f_ += 1
            if f_ == filaments_number: break
            snake.append((effective_side+i,(3+j)*i,z))
            snake.append((2*i,(3+j)*i,z))
            f_ += 1
        snake = np.array(snake)
        rawDistances = np.diff(snake, axis=0)
        extrusionDistances                                          =
np.concatenate(([0],np.hypot(rawDistances[:,0], rawDistances[:,1])))
        extrusionDistancesCumSum = np.cumsum(extrusionDistances)
        result                                                      =
np.concatenate((snake,extrusionDistancesCumSum.reshape(-1,1)),axis=1)
        return result

    def buildSnakeY(effective_side, i, filaments_number, z):
        snake = []
        f_ = 0
        for j in range(0,filaments_number,2):
            if f_ == filaments_number: break
            snake.append(((2+j)*i,2*i,z))
            snake.append(((2+j)*i,effective_side+i,z))
            f_ += 1
            if f_ == filaments_number: break
            snake.append(((3+j)*i,effective_side+i,z))
            snake.append(((3+j)*i,2*i,z))
            f_ += 1
        snake = np.array(snake)
        rawDistances = np.diff(snake, axis=0)
        extrusionDistances                                          =
np.concatenate(([0],np.hypot(rawDistances[:,0], rawDistances[:,1])))
        extrusionDistancesCumSum = np.cumsum(extrusionDistances)
        result                                                      =
np.concatenate((snake,extrusionDistancesCumSum.reshape(-1,1)),axis=1)
        return result


    # Definition z for Z ####
```

```
    print("Initiating Zs...")
    Z = np.linspace(i*k, numberOfLayers*k*i, num=numberOfLayers)

    # All coordinates definition ####

    print("Building geometry...")
    outputs = []
    for z in Z:
        ib = buildInternalBorder(effectiveSide, i, z)
        ib[:,0] = ib[:,0] - (effectiveSide+3*i)/2
        ib[:,1] = ib[:,1] - (effectiveSide+3*i)/2
        eb = buildExternalBorder(effectiveSide, i, z)
        eb[:,0] = eb[:,0] - (effectiveSide+3*i)/2
        eb[:,1] = eb[:,1] - (effectiveSide+3*i)/2
        if np.where(Z == z)[0][0]%2 == 0:
            sn = buildSnakeX(effectiveSide, i, filamentsNumber, z)
            sn[:,0] = sn[:,0] - (effectiveSide+3*i)/2
            sn[:,1] = sn[:,1] - (effectiveSide+3*i)/2
        else:
            sn = buildSnakeY(effectiveSide, i, filamentsNumber, z)
            sn[:,0] = sn[:,0] - (effectiveSide+3*i)/2
            sn[:,1] = sn[:,1] - (effectiveSide+3*i)/2

outputs.append({"z":z,"components":{"internal_border":ib,"external_bord
er":eb,"snake":sn}})

    # Coordinates to G-Code ####

    GCODE = ""
    GCODE_GLOBAL_HEADER = """
    ;_______________
    ;PRIMING
    ;_______________

    G21; metric values
    G90; absolute positioning
    M82; set extruder to absolute mode
    G28; home all axes
    G92 E0
    M27 S30
    ;____________
    """
    GCODE_GLOBAL_FOOTER = "G28"

    # Component Layouts ----------------------------------

    componentHeader = """
    ;{c}
    G1 F3600
    G1 X{x1} Y{y1} Z{z1} E0
    G1 F800
    G1 E1
    G92 E0
```

```
G1 E0
;___________
"""
componentBody = "G1 X{x} Y{y} Z{z} E{e}\n"
componentFooter = """
;___________
;CLOSE STEP
G92 E0
G1 E1
G92 E0
G0 F3600 Z100
;_____________
"""

# G-Code Encoding ####

print("Building G-CODE...")

GCODE += GCODE_GLOBAL_HEADER
for zOutput in outputs:
    zGCode = ""
    for componentName in zOutput["components"].keys():
        print(f"> Encoding '{componentName}' at layer height
{round(zOutput['z'],2)}...")
        componentGCode = ""
        componentGCode                                          +=
componentHeader.format(x1=round(zOutput["components"][componentName][0,
0],2),

y1=round(zOutput["components"][componentName][0,1],2),

z1=round(zOutput["components"][componentName][0,2],2),

e=round(zOutput["components"][componentName][0,3],2),
                                                        c       =
componentName)
        for p in zOutput["components"][componentName]:
            componentGCode                                      +=
componentBody.format(x=round(p[0],2),y=round(p[1],2),z=round(p[2],2),e=
round(p[3],2))
        componentGCode += componentFooter
        zGCode += componentGCode
    GCODE += zGCode

GCODE += GCODE_GLOBAL_FOOTER

# Save ####

print(f"Saving '{filename}.gcode'...")
with open(f"{filename}.gcode","w") as f:
    f.write(GCODE)
print(f"Saved!")
```

ANNEX B

G-code of the parallelepiped with squared basis of 75.2 mm
Printed with nozzle having diameter d_n = 1.41 mm

In this Annex, the blocks relative to the first three layers of the G-code used to print the sample having squared basis of 75.2 mm printed with nozzle having diameter d_n = 1.41 mm are reported.

The blocks relative to the successive layers only differ on the value of the Z-coordinate, therefore it has been chosen to omit them in the printed version of this thesis. However, the complete G-code can be accessed at the following link:

```
;____________
;PRIMING
;____________

G21 ;metric values
G90 ;absolute positioning
M82 ;set extruder to absolute
mode
G28 ;home all axes
G92 E0
M27 S30
;________
;___LAYER:01 Z1.3
;________
;INTERNAL BORDER
G0 F3600
G0 X-36 Y36 Z1.3
G1 X-36 Y36 E0
G0 F800
G1 E1
G92 E0
G1 E0
G1 X36 Y36 E72
G1 X36 Y-36 E144
G1 X-36 Y-36 E216
G1 X-36 Y36 E288
;_______
;CLOSE STEP
G92 E0
G1 E1
G92 E0
G0 F3600 Z100
;_________
;EXTERNAL BORDER
G0 F3600
G0 X-37.6 Y37.6 Z1.3
G1 X-37.6 Y37.6 E0
G0 F800
G1 E1
G92 E0
G1 E0
G1 X37.6 Y37.6 E75.2
G1 X37.6 Y-37.6 E150.4
G1 X-37.6 Y-37.6 E225.6
G1 X-37.6 Y37.6 E300.8
;_______
;CLOSE STEP
G92 E0
G1 E1
G92 E0
G0 F3600 Z100
;_______________________
;INFILL (X)
G0 F3600
G1 X-35.2 Y35.2 Z1.3
G1 X-35.2 Y35.2 E0
G0 F800
G1 E1
G92 E0
G1 E0
G1 X35.2 Y35.2 E70.4
G1 X35.2 Y33.6 E72
G1 X-35.2 Y33.6 E142.4
G1 X-35.2 Y32 E144
G1 X35.2 Y32 E214.4
G1 X35.2 Y30.4 E216
G1 X-35.2 Y30.4 E286.4
G1 X-35.2 Y28.8 E288
G1 X35.2 Y28.8 E358.4
G1 X35.2 Y27.2 E360
```

```
G1 X-35.2 Y27.2 E430.4
G1 X-35.2 Y25.6 E432
G1 X35.2 Y25.6 E502.4
G1 X35.2 Y24 E504
G1 X-35.2 Y24 E574.4
G1 X-35.2 Y22.4 E576
G1 X35.2 Y22.4 E646.4
G1 X35.2 Y20.8 E648
G1 X-35.2 Y20.8 E718.4
G1 X-35.2 Y19.2 E720
G1 X35.2 Y19.2 E790.4
G1 X35.2 Y17.6 E792
G1 X-35.2 Y17.6 E862.4
G1 X-35.2 Y16 E864
G1 X35.2 Y16 E934.4
G1 X35.2 Y14.4 E936
G1 X-35.2 Y14.4 E1006.4
G1 X-35.2 Y12.8 E1008
G1 X35.2 Y12.8 E1078.4
G1 X35.2 Y11.2 E1080
G1 X-35.2 Y11.2 E1150.4
G1 X-35.2 Y9.6 E1152
G1 X35.2 Y9.6 E1222.4
G1 X35.2 Y8 E1224
G1 X-35.2 Y8 E1294.4
G1 X-35.2 Y6.4 E1296
G1 X35.2 Y6.4 E1366.4
G1 X35.2 Y4.8 E1368
G1 X-35.2 Y4.8 E1438.4
G1 X-35.2 Y3.2 E1440
G1 X35.2 Y3.2 E1510.4
G1 X35.2 Y1.6 E1512
G1 X-35.2 Y1.6 E1582.4
G1 X-35.2 Y0 E1584
G1 X35.2 Y0 E1654.4
G1 X35.2 Y-1.6 E1656
G1 X-35.2 Y-1.6 E1726.4
G1 X-35.2 Y-3.2 E1728
G1 X35.2 Y-3.2 E1798.4
G1 X35.2 Y-4.8 E1800
G1 X-35.2 Y-4.8 E1870.4
G1 X-35.2 Y-6.4 E1872
G1 X35.2 Y-6.4 E1942.4
G1 X35.2 Y-8 E1944
G1 X-35.2 Y-8 E2014.4
G1 X-35.2 Y-9.6 E2016
G1 X35.2 Y-9.6 E2086.4
G1 X35.2 Y-11.2 E2088
G1 X-35.2 Y-11.2 E2158.4
G1 X-35.2 Y-12.8 E2160
G1 X35.2 Y-12.8 E2230.4
G1 X35.2 Y-14.4 E2232
G1 X-35.2 Y-14.4 E2302.4
G1 X-35.2 Y-16 E2304
G1 X35.2 Y-16 E2374.4
G1 X35.2 Y-17.6 E2376
G1 X-35.2 Y-17.6 E2446.4
G1 X-35.2 Y-19.2 E2448
G1 X35.2 Y-19.2 E2518.4
G1 X35.2 Y-20.8 E2520
G1 X-35.2 Y-20.8 E2590.4
G1 X-35.2 Y-22.4 E2592
G1 X35.2 Y-22.4 E2662.4
G1 X35.2 Y-24 E2664
G1 X-35.2 Y-24 E2734.4
G1 X-35.2 Y-25.6 E2736
G1 X35.2 Y-25.6 E2806.4
G1 X35.2 Y-27.2 E2808
G1 X-35.2 Y-27.2 E2878.4
G1 X-35.2 Y-28.8 E2880
G1 X35.2 Y-28.8 E2950.4
G1 X35.2 Y-30.4 E2952
G1 X-35.2 Y-30.4 E3022.4
G1 X-35.2 Y-32 E3024
G1 X35.2 Y-32 E3094.4
G1 X35.2 Y-33.6 E3096
G1 X-35.2 Y-33.6 E3166.4
G1 X-35.2 Y-35.2 E3168
G1 X35.2 Y-35.2 E3238.4
;_______
;CLOSE STEP
G92 E0
G1 E1
G92 E0
G0 F3600 Z100
;________
;___LAYER:02 Z2.6
;________
;INTERNAL BORDER
G0 F3600
G0 X-36 Y36 Z2.6
G1 X-36 Y36 E0
G0 F800
G1 E1
G92 E0
G1 E0
G1 X36 Y36 E72
G1 X36 Y-36 E144
```

```
G1 X-36 Y-36 E216
G1 X-36 Y36 E288
;_______
;CLOSE STEP
G92 E0
G1 E1
G92 E0
G0 F3600 Z100
;_________
;EXTERNAL BORDER
G0 F3600
G0 X-37.6 Y37.6 Z2.6
G1 X-37.6 Y37.6 E0
G0 F800
G1 E1
G92 E0
G1 E0
G1 X37.6 Y37.6 E75.2
G1 X37.6 Y-37.6 E150.4
G1 X-37.6 Y-37.6 E225.6
G1 X-37.6 Y37.6 E300.8
;_______
;CLOSE STEP
G92 E0
G1 E1
G92 E0
G0 F3600 Z100
;_____________________
;INFILL (Y)
G0 F3600
G1 X35.2 Y-35.2 Z2.6
G1 X35.2 Y-35.2 E0
G0 F800
G1 E1
G92 E0
G1 E0
G1 X35.2 Y35.2 E70.4
G1 X33.6 Y35.2 E72
G1 X33.6 Y-35.2 E142.4
G1 X32 Y-35.2 E144
G1 X32 Y35.2 E214.4
G1 X30.4 Y35.2 E216
G1 X30.4 Y-35.2 E286.4
G1 X28.8 Y-35.2 E288
G1 X28.8 Y35.2 E358.4
G1 X27.2 Y35.2 E360
G1 X27.2 Y-35.2 E430.4
G1 X25.6 Y-35.2 E432
G1 X25.6 Y35.2 E502.4
G1 X24 Y35.2 E504
G1 X24 Y-35.2 E574.4
G1 X22.4 Y-35.2 E576
G1 X22.4 Y35.2 E646.4
G1 X20.8 Y35.2 E648
G1 X20.8 Y-35.2 E718.4
G1 X19.2 Y-35.2 E720
G1 X19.2 Y35.2 E790.4
G1 X17.6 Y35.2 E792
G1 X17.6 Y-35.2 E862.4
G1 X16 Y-35.2 E864
G1 X16 Y35.2 E934.4
G1 X14.4 Y35.2 E936
G1 X14.4 Y-35.2 E1006.4
G1 X12.8 Y-35.2 E1008
G1 X12.8 Y35.2 E1078.4
G1 X11.2 Y35.2 E1080
G1 X11.2 Y-35.2 E1150.4
G1 X9.6 Y-35.2 E1152
G1 X9.6 Y35.2 E1222.4
G1 X8 Y35.2 E1224
G1 X8 Y-35.2 E1294.4
G1 X6.4 Y-35.2 E1296
G1 X6.4 Y35.2 E1366.4
G1 X4.8 Y35.2 E1368
G1 X4.8 Y-35.2 E1438.4
G1 X3.2 Y-35.2 E1440
G1 X3.2 Y35.2 E1510.4
G1 X1.6 Y35.2 E1512
G1 X1.6 Y-35.2 E1582.4
G1 X0 Y-35.2 E1584
G1 X0 Y35.2 E1654.4
G1 X-1.6 Y35.2 E1656
G1 X-1.6 Y-35.2 E1726.4
G1 X-3.2 Y-35.2 E1728
G1 X-3.2 Y35.2 E1798.4
G1 X-4.8 Y35.2 E1800
G1 X-4.8 Y-35.2 E1870.4
G1 X-6.4 Y-35.2 E1872
G1 X-6.4 Y35.2 E1942.4
G1 X-8 Y35.2 E1944
G1 X-8 Y-35.2 E2014.4
G1 X-9.6 Y-35.2 E2016
G1 X-9.6 Y35.2 E2086.4
G1 X-11.2 Y35.2 E2088
G1 X-11.2 Y-35.2 E2158.4
G1 X-12.8 Y-35.2 E2160
G1 X-12.8 Y35.2 E2230.4
G1 X-14.4 Y35.2 E2232
```

```
G1 X-14.4 Y-35.2 E2302.4
G1 X-16 Y-35.2 E2304
G1 X-16 Y35.2 E2374.4
G1 X-17.6 Y35.2 E2376
G1 X-17.6 Y-35.2 E2446.4
G1 X-19.2 Y-35.2 E2448
G1 X-19.2 Y35.2 E2518.4
G1 X-20.8 Y35.2 E2520
G1 X-20.8 Y-35.2 E2590.4
G1 X-22.4 Y-35.2 E2592
G1 X-22.4 Y35.2 E2662.4
G1 X-24 Y35.2 E2664
G1 X-24 Y-35.2 E2734.4
G1 X-25.6 Y-35.2 E2736
G1 X-25.6 Y35.2 E2806.4
G1 X-27.2 Y35.2 E2808
G1 X-27.2 Y-35.2 E2878.4
G1 X-28.8 Y-35.2 E2880
G1 X-28.8 Y35.2 E2950.4
G1 X-30.4 Y35.2 E2952
G1 X-30.4 Y-35.2 E3022.4
G1 X-32 Y-35.2 E3024
G1 X-32 Y35.2 E3094.4
G1 X-33.6 Y35.2 E3096
G1 X-33.6 Y-35.2 E3166.4
G1 X-35.2 Y-35.2 E3168
G1 X-35.2 Y35.2 E3238.4
;_______
;CLOSE STEP
G92 E0
G1 E1
G92 E0
G0 F3600 Z100
;________
;___LAYER:03 Z3.9
;________
;INTERNAL BORDER
G0 F3600
G0 X-36 Y36 Z3.9
G1 X-36 Y36 E0
G0 F800
G1 E1
G92 E0
G1 E0
G1 X36 Y36 E72
G1 X36 Y-36 E144
G1 X-36 Y-36 E216
G1 X-36 Y36 E288
;_______
;CLOSE STEP
G92 E0
G1 E1
G92 E0
G0 F3600 Z100
;_________
;EXTERNAL BORDER
G0 F3600
G0 X-37.6 Y37.6 Z3.9
G1 X-37.6 Y37.6 E0
G0 F800
G1 E1
G92 E0
G1 E0
G1 X37.6 Y37.6 E75.2
G1 X37.6 Y-37.6 E150.4
G1 X-37.6 Y-37.6 E225.6
G1 X-37.6 Y37.6 E300.8
;_______
;CLOSE STEP
G92 E0
G1 E1
G92 E0
G0 F3600 Z100
;_______________________
;INFILL (X)
G0 F3600
G1 X-35.2 Y35.2 Z3.9
G1 X-35.2 Y35.2 E0
G0 F800
G1 E1
G92 E0
G1 E0
G1 X35.2 Y35.2 E70.4
G1 X35.2 Y33.6 E72
G1 X-35.2 Y33.6 E142.4
G1 X-35.2 Y32 E144
G1 X35.2 Y32 E214.4
G1 X35.2 Y30.4 E216
G1 X-35.2 Y30.4 E286.4
G1 X-35.2 Y28.8 E288
G1 X35.2 Y28.8 E358.4
G1 X35.2 Y27.2 E360
G1 X-35.2 Y27.2 E430.4
G1 X-35.2 Y25.6 E432
G1 X35.2 Y25.6 E502.4
G1 X35.2 Y24 E504
G1 X-35.2 Y24 E574.4
G1 X-35.2 Y22.4 E576
```

```
G1 X35.2 Y22.4 E646.4
G1 X35.2 Y20.8 E648
G1 X-35.2 Y20.8 E718.4
G1 X-35.2 Y19.2 E720
G1 X35.2 Y19.2 E790.4
G1 X35.2 Y17.6 E792
G1 X-35.2 Y17.6 E862.4
G1 X-35.2 Y16 E864
G1 X35.2 Y16 E934.4
G1 X35.2 Y14.4 E936
G1 X-35.2 Y14.4 E1006.4
G1 X-35.2 Y12.8 E1008
G1 X35.2 Y12.8 E1078.4
G1 X35.2 Y11.2 E1080
G1 X-35.2 Y11.2 E1150.4
G1 X-35.2 Y9.6 E1152
G1 X35.2 Y9.6 E1222.4
G1 X35.2 Y8 E1224
G1 X-35.2 Y8 E1294.4
G1 X-35.2 Y6.4 E1296
G1 X35.2 Y6.4 E1366.4
G1 X35.2 Y4.8 E1368
G1 X-35.2 Y4.8 E1438.4
G1 X-35.2 Y3.2 E1440
G1 X35.2 Y3.2 E1510.4
G1 X35.2 Y1.6 E1512
G1 X-35.2 Y1.6 E1582.4
G1 X-35.2 Y0 E1584
G1 X35.2 Y0 E1654.4
G1 X35.2 Y-1.6 E1656
G1 X-35.2 Y-1.6 E1726.4
G1 X-35.2 Y-3.2 E1728
G1 X35.2 Y-3.2 E1798.4
G1 X35.2 Y-4.8 E1800
G1 X-35.2 Y-4.8 E1870.4
G1 X-35.2 Y-6.4 E1872
G1 X35.2 Y-6.4 E1942.4
G1 X35.2 Y-8 E1944
G1 X-35.2 Y-8 E2014.4
G1 X-35.2 Y-9.6 E2016
G1 X35.2 Y-9.6 E2086.4
G1 X35.2 Y-11.2 E2088
G1 X-35.2 Y-11.2 E2158.4
G1 X-35.2 Y-12.8 E2160
G1 X35.2 Y-12.8 E2230.4
G1 X35.2 Y-14.4 E2232
G1 X-35.2 Y-14.4 E2302.4
G1 X-35.2 Y-16 E2304
G1 X35.2 Y-16 E2374.4
G1 X35.2 Y-17.6 E2376
G1 X-35.2 Y-17.6 E2446.4
G1 X-35.2 Y-19.2 E2448
G1 X35.2 Y-19.2 E2518.4
G1 X35.2 Y-20.8 E2520
G1 X-35.2 Y-20.8 E2590.4
G1 X-35.2 Y-22.4 E2592
G1 X35.2 Y-22.4 E2662.4
G1 X35.2 Y-24 E2664
G1 X-35.2 Y-24 E2734.4
G1 X-35.2 Y-25.6 E2736
G1 X35.2 Y-25.6 E2806.4
G1 X35.2 Y-27.2 E2808
G1 X-35.2 Y-27.2 E2878.4
G1 X-35.2 Y-28.8 E2880
G1 X35.2 Y-28.8 E2950.4
G1 X35.2 Y-30.4 E2952
G1 X-35.2 Y-30.4 E3022.4
G1 X-35.2 Y-32 E3024
G1 X35.2 Y-32 E3094.4
G1 X35.2 Y-33.6 E3096
G1 X-35.2 Y-33.6 E3166.4
G1 X-35.2 Y-35.2 E3168
G1 X35.2 Y-35.2 E3238.4
;_______
;CLOSE STEP
G92 E0
G1 E1
G92 E0
G0 F3600 Z100
[…]
;_______
;POWERING DOWN
;_______
G28
```

ANNEX C

Point type G-Code

```
G28 ;home all axes
G1 Z5 F5000 ;lift nozzle

G21 ;set units to millimeters
G90 ;use absolute coordinates
M82 ;use absolute distances for extrusion
G92 E0

G1 X10 Y100 F7800 ;go to first position
G1 Z5 F100       ;set z-level
G4 S30           ;stay 30 seconds
G1 Z5 F5000      ;lift nozzle

G28
```

ANNEX D

Line type G-Code

```
G28 ;home all axes
G1 Z5 F5000 ;lift nozzle

G21 ;set units to millimeters
G90 ;use absolute coordinates
M82 ;use absolute distances for extrusion
G92 E0

G1 X10 Y100 F7800.000 ;go to first position
G1 Z5 F100            ;set z-level
G0 F900               ;set printing velocity
G1 X50 Y100
G92 E0

G28
```

ANNEX E

Multimaterial line type G-Code

```
G28 ;home all axes                G28
G1 Z10 F5000 ;lift nozzle

G21 ;set units to millimeters
G90 ;use absolute coordinates
M82 ;use absolute distances
for extrusion
G92 E0

T0 ;first extruder to be used
G1 X10 Y100 F7800 ;go to
first position
G1 Z0 F100 ;set z-level

G0 F900 ;set printing
velocity to 900 mm/min = 15
mm/s

G1 X50 Y100
G4 P1
T1 ;extruder S2 to be used
G4 P533
G1 X290 Y100
G1 X290 Y105

G1 X250 Y105
G4 P1
T0 ;extruder S1 to be used
G4 P533

G1 X10 Y105
G1 X10 Y110

G1 X50 Y110
G4 P1
T1 ;extruder S2 to be used
G4 P533
G1 X290 Y110

G1 Z30
G1 X290 Y290
```